AN ABSTRACT OF THE THESIS OF

Heinz D. Fuchs for the degree of Master of Science in Physics presented on February 16, 1990 .

Title : Perturbed Angular Correlation Investigation of Cubic Zirconia

Redacted for privacy

Abstract approved : _____

John A. Gardner

Perturbed angular correlation (PAC) spectra of fully yttria-stabilized (cubic) zirconia with Y_2O_3 contents of 35.4 wt. %, 27.8 wt. %, and 16.9 wt. %, respectively, were measured using the isotope ^{181}Ta as probe nucleus.

PAC spectra in cubic zirconia are characterized by a wide frequency distribution due to contributions of dopant cations (Y) and oxygen vacancies. The jump rate for oxygen vacancies in the lattice is several orders of magnitude higher than for the cations. In the entire temperature range (24°C to 1300°C) the cations can be considered static, whereas the mobility of the anion vacancies is strongly temperature-dependent. The spectra show that the electric field gradient (EFG) is static at highest ($T > 1200$°C) and lowest ($T < 500$°C) temperatures. The contributions to the EFG due to oxygen vacancies average to zero for the highest temperatures because of the fast vacancy jump rate. At the lowest temperatures, the vacancy jump time is greater than the lifetime of the intermediate state (10.8 ns), resulting in a static EFG. A relaxation phenomena arising from diffusion of oxygen vacancies was observed for intermediate temperatures.

The relaxation parameter, λ, has a maximum at about 850°C. In the high-temperature region (T > 850°C), λ has an activated form. The activation energy for the oxygen vacancy motion, E_a, is 1.06 eV (± 0.07 eV) and is independent of the Y_2O_3 concentration which contradicts results obtained from ionic conductivity measurements found in the literature.

The EFG increases by a factor of three with decreasing temperature from 1200°C to 500°C. It is proposed that this is caused by dynamical screening: at elevated temperatures oxygen vacancies jump into higher-energy positions closer to the PAC probe, reducing the cationic contribution to the EFG. The activation energy for this process is 0.2 eV (± 0.02 eV).

PAC measurements on samples heated up to different temperatures show that the material must be annealed for about 24 hours at 1300°C. Even though the Y_2O_3 concentrations were 16.9 wt. % and higher, the samples were inhomogeneous without annealing.

A computer simulation of the angular perturbation function, $G_2(t)$, was developed, and the results for a static EFG, the XYZ model, and rapidly jumping vacancies in a simple cubic lattice are presented. The simulation assumes that (i) the atoms of Zr and Y are randomly distributed, (ii) the oxygen vacancies can be described as point ions, (iii) there are no interactions between the oxygen vacancies and no interactions between the vacancies and Zr or Y, (iv) the vacancies can only jump to next-nearest-neighbor sites, and (v) the vacancies never occupy nearest-neighbor sites to the PAC probe.

The results from the static EFG and the XYZ model are in agreement with theoretical calculations. The transition probability, W, between two particular EFG states per unit time is proportional to the inverse of the average correlation time, τ_c, and the number of possible EFG states, N.

Perturbed Angular Correlation Investigation of Cubic Zirconia

by

Heinz D. Fuchs

A Thesis

submitted to

Oregon State University

in partial fulfillment of
the requirements for the
degree of

Master of Science

Completed February 16, 1990

Commencement June 1990

Approved:

Redacted for privacy

Professor of Physics in charge of major

Redacted for privacy

Chairman of the Department of Physics

Redacted for privacy

Dean of Graduate School

Date thesis is presented February 16, 1990

Typed by Heinz D. Fuchs for Heinz D. Fuchs

Table of Contents

List of Figures

List of Tables

Perturbed Angular Correlation Investigation of Cubic Zirconia

1. Introduction

Ceramics are encountered quite frequently in every-day life. Toilet bowls, bath tubs, cookware and many other things made out of ceramics have been used for decades. But it took a Nobel prize to emphasize the scientific value of ceramics. In fact, it was not until the discovery of high T_c superconductivity in La-Ba-Cu systems[1] that many scientists focused their attention on ceramics. Nevertheless, ceramics such as ZrO_2, SiC, Si_3N_4 have always been a field of scientific study.

Ceramics possess useful properties such as low wear, good dielectric properties, high resistance against heat and aggressive chemicals, and extreme mechanical stiffness and hardness which is in general retained at higher temperatures than metals. A lot of work has been done particularly on zirconia (ZrO_2), since it has been found to be a structural toughener in improving the crack resistance of ceramics. Not only has zirconia been used as an additive to improve mechanical properties of other ceramics, but it has also been used as the major constituent for ceramics. A wide range of technological applications for zirconia-based ceramics include cutting tools, machinery wear parts, thermal barrier coatings, piezoelectric devices, and magnetohydrodynamic generators. Zirconia alloys also are very good oxygen conductors at high temperatures and have therefore often been used, for example, as oxygen sensors and fuel cells.[2,3,4]

1.1. Zirconia

Research activity on zirconia ceramics has been very intense in the past several decades due to its potential applications. A conference, held every three years, is devoted to the exchange of research information on these materials.[2,3,4] A very helpful yet concise booklet on the general properties of zirconia has been compiled by Stevens.[5]

1.1.1. Occurrence and Processing

The element zirconium (Zr) is present at a level of 0.02 to 0.03 % in the earth's crust and is more abundant than copper, nickel, lead, or zinc. The two main mineral sources of zirconium are baddeleyite and zircon.

- Baddeleyite is the mineral form in which zirconium was discovered in 1892 in Brazil. Today it is extracted as uranium, copper, and phosphate minerals are processed.
- Zircon ($ZrO_2 \cdot SiO_2$) is the most abundant zirconium mineral. It is found as secundary deposits with other minerals in river and beach sands and it contains small amounts of titanium oxide, ferric oxides, and aluminum.

Crude grades of zirconia can be produced by thermal treatment of zircon. But higher purity zirconia, which is of interest for scientific use, must be chemically processed. In this process zircon must first be decomposed and then treated. Pure zirconia is then isolated and finally calcined. The resulting zirconia is the basis for further research.

1.1.2. Structure

In different temperature regions pure zirconia exhibits three well-defined polymorphs. These phases are stable at the following temperatures:

monoclinic below ~1170°C.

tetragonal between ~1170 and 2370°C.

cubic between 2370°C and ~2680°C (melting point)

The unit cells of various phases of zirconia are generally considered to be derivations of the cubic fluorite structure. It has also been shown that at room temperature with pressure above 40 kbar zirconia can transform into an orthorhombic form.[6]

Monoclinic ZrO_2 has four formula units in the unit cell and has the space group $P2_1/c$.[7] The atomic arrangement in the unit cell is[8]

$$\pm(xyz;\ \bar{x}, y+1/2, 1/2-z)$$

with the cell dimensions[9]

$$a = 5.145\ \text{Å};\ b = 5.028\ \text{Å};\ c = 5.311\ \text{Å};\ b = 99.2^\circ .$$

The Zr^{4+} ion is seven–fold coordinated by two types of oxygen atoms with the O_{II} coordination nearly tetrahedral. The Zr atoms are positioned at (0.2758, 0.0411, 0.2082), O_I are located at (0.070, 0.342, 0.341), and O_{II} are located at (0.442, 0.775, 0.479). At room temperature, the average Zr–O_I range from 2.05 to 2.16Å and for Zr–O_{II} from 2.15 to 2.29Å. The thermal expansion of monoclinic ZrO_2 is very anisotropic,

with the expansion coefficient for the a and c axes an order of magnitude higher than that of the b axis.[10]

In the tetragonal phase the space group is $P4_2/nmc$. Instead of describing the tetragonal cell in terms of a face centered lattice, for tetragonal pure zirconia a primitive tetragonal unit cell is often found in the literature.[11,12] The atomic arrangement in the unit cell is

2 Zr : (0, 0, 0); (1/2, 1/2, 1/2)

4 O : (1, 1/2, z); (1/2, 0, –z); (0, 1/2, 1/2+z); (1/2, 0, 1/2–z) .

The unit cell dimensions are

a = 3.64 Å; c = 5.27 Å ,

with z = 0.185 at 1250°C. Each oxygen atom is coordinated by four zirconium atoms and each Zr atom is eight–fold coordinated with four O atoms at a distance 2.455Å and four at 2.065Å. The latter four oxygen atoms form a flattened tetrahedron with the zirconium, while the former four O atoms and Zr form a more elongated tetrahedron rotated by 90° with respect to the first one.

The phase transformation between the monoclinic and the tetragonal phases is of both scientific and technological importance. Pure zirconia undergoes a volume contraction on heating and a corresponding expansion on cooling, typically 3–5%, through the monoclinic⇔tetragonal transformation. This large volume change is often accomplished by cracking, causing the zirconia to crumble. Thus pure zirconia is not suitable for structural applications. However it was realized that this disruptive transformation can be used to increase the strength and toughness of other ceramics.[13]

The monoclinic⇔tetragonal transformation of pure ZrO_2 was first suggested by Wolten[14] to be martensitic in nature. Some of the experimental observations that led to that conclusion are:[15]

- The tetragonal phase cannot be quenched to room temperature.
- The transformation exhibits a large temperature hysteresis loop.
- The transformation is athermal, i.e., it does not take place at a fixed temperature but over a range. The amount of transformed phase changes with temperature but not as a function of time at a fixed temperature.

Above 2370°C up to the melting point at ~2680°C, the zirconia takes on the cubic form. This phase is a fluorite structure, with the spacegroup symmetry F_{m3m}. The atomic arrangement in the unit cell is

$$Zr: (0, 0, 0)$$
$$0: (\pm 1/4, \pm 1/4, \pm 1/4)$$

with a unit cell dimension of

$$a = 5.198 \text{ Å}.$$

Each Zr atom is eight-fold coordinated by equidistant oxygen atoms, and the O atoms are tetrahedrally coordinated by four zirconium atoms with a Zr-O distance of 2.251 Å (Fig. 1.1.).

There is evidence from neutron-diffraction studies that the oxygen positions are shifted similar to the tetragonal cell but to a smaller extent.[16]

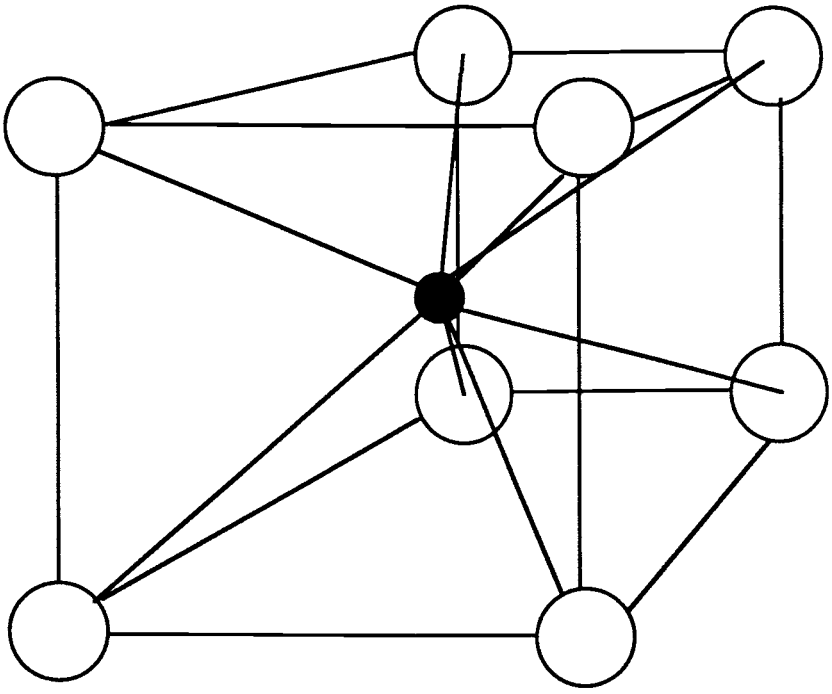

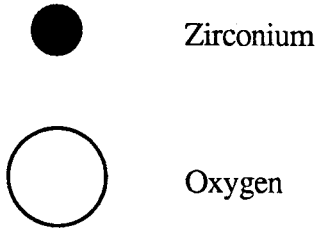

Fig. 1.1 The first oxygen coordination shell for Zr in cubic zirconia

1.1.3. Zirconia Alloys

For practical applications, ZrO_2 has often been alloyed with other oxides to modify its properties. Binary oxide alloys of ZrO_2 with CaO, MgO, Y_2O_3, In_2O_3, and rare earth oxides lower the temperatures where the monoclinic⇔tetragonal and tetragonal⇔cubic phase transformation occur.[17,18] The phase diagrams of the systems ZrO_2–MgO, ZrO_2–CaO, and ZrO_2–Y_2O_3 have been reviewed by Stubican.[19] The ZrO_2–Y_2O_3 binary system,[20] which is the matter of investigation in this research, is shown in Fig. 1.2.

When alloyed with more than ~17 mol.% of Y_2O_3, the cubic phase is stable from room temperature to the melting point. This composition region, which is the subject of investigation in the following chapters, is commonly known as fully stabilized zirconia (FSZ), or with reference to the stabilizing agent, yttria stabilized zirconia (YSZ), calcia stabilized zirconia (CSZ), etc.

Partially stabilized zirconia (PSZ) , which is a mixture of cubic and tetragonal (or monoclinic) zirconia, occurs when the dopant concentration is less than is needed for complete stabilization.

The incorporation of alloying metal oxides also decreases the linear thermal expansion coefficient of the two–phase zirconia and the volume change associated with the monoclinic⇔tetragonal transformation. The PSZ, thus, has better thermal shock resistance than fully stabilized and pure monoclinic zirconia.[15]

Besides the modification of mechanical properties when doped with metal oxides, oxygen vacancies are also introduced as charge compensators for lower valence cation dopants. One oxygen vacancy is created for every divalent cation dopant (e.g. Ca^{2+}, Mg^{2+}) or for every two trivalent cation dopants (e.g. Y^{3+}, Sc^{3+}). Every two pentavalent cation dopants (e.g. Ta^{5+}, Nb^{5+}), however, introduce one oxygen

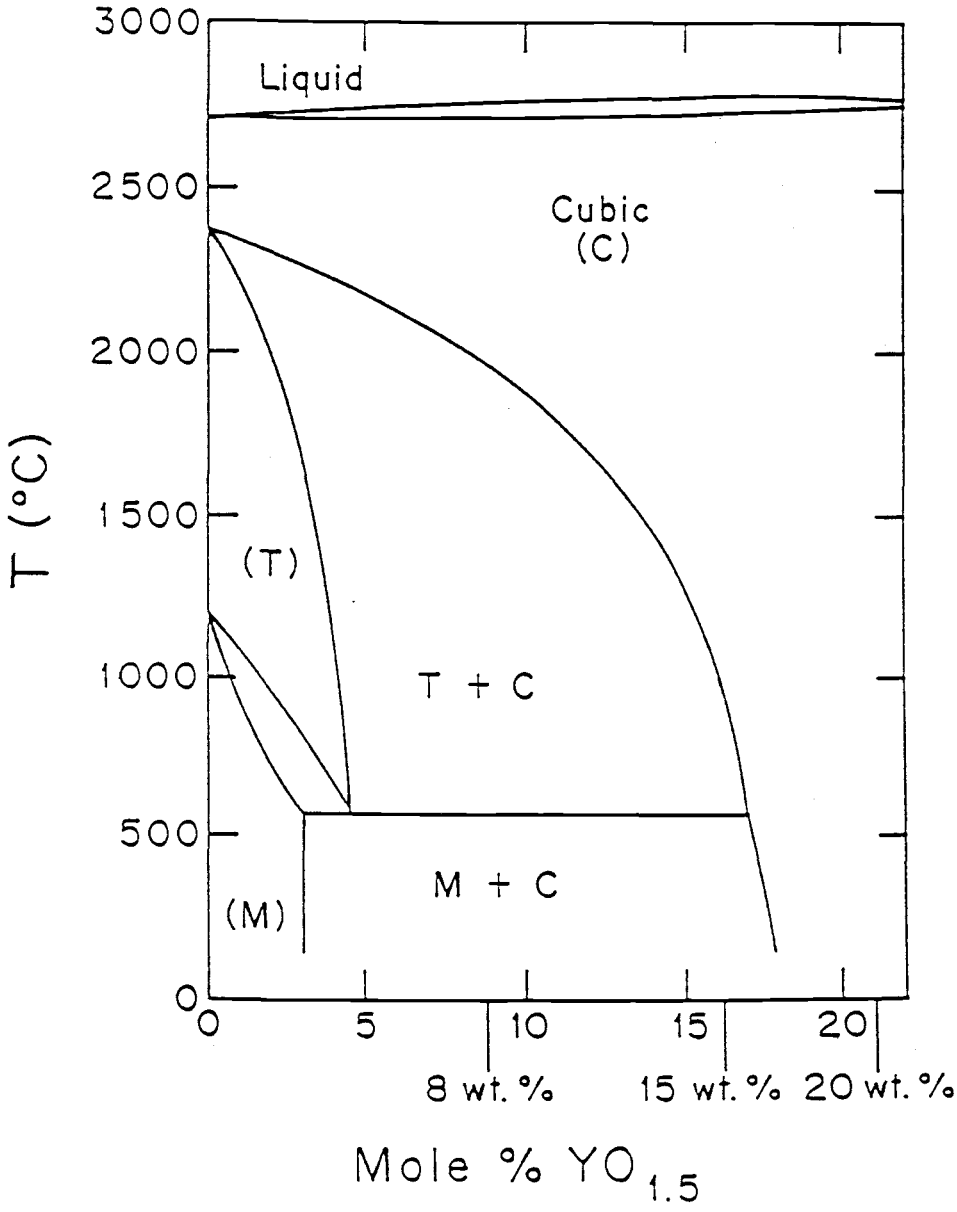

Fig. 1.2. Phase diagram for the ZrO_2–Y_2O_3 system.

interstitial. Therefore the concentration of oxygen vacancies or interstitials can be manipulated by doping with appropriate species of dopant cations. Similar to other fluorite oxides, oxygen vacancies are the dominant carriers for ionic conductivity in ZrO_2. The oxygen diffusion motion in the zirconia is an activated process and exhibits an Arrhenius behavior with an activation energy of about 1 eV. More details of this process will be discussed later in this work.

1.1.4. Applications of Zirconia Ceramics

As already mentioned, there are numerous technological applications of zirconia ceramics. Among these are the following:

- **Wear components in combustion engines.** Fine tetragonal zirconia particles incorporated in other ceramics such as alumina or silicon carbide increase their strength and fracture toughness.
- **Thermal barrier coating in gas turbine engines.** Thin layers of YSZ on metal parts allow an increase of the operating temperatures and result in an increased efficiency of the engines.
- **Heating elements in furnaces which operate above 2000°C.** After preheating the zirconia element to about 1000 °C, the ionic conductivity is sufficient for self-heating.
- **Oxygen sensors.** Because of the excellent heat resistance of zirconia, oxygen sensors can even be used at high temperatures. If the opposite sides of a zirconia electolyte are exposed to different partial oxygen pressures p_1 and p_2 respectively, a voltage across the electolyte is created, which is proportional to $\ln (p_1 / p_2)$.

- **Imitation diamonds.** A high refractive index of cubic zirconia is responsible for its use as imitation diamonds. It is even possible to produce large-sized optical-quality single crystals with diameters up to 10 cm.[21] Colored gemstones can be manufactured by adding rare earth or transition metal oxides.

1.2. Perturbed Angular Correlation Spectroscopy (PAC)

The angular distribution of radiations from an atomic or nuclear system, decaying in a cascade of successive γ–rays, have their characteristic patterns with respect to a chosen axis.[22] Usually the first γ–ray is used to establish the quantization axis against which the direction of the second γ–ray is correlated. Studies of the angular correlation of such successive radiations have been a very useful tool in nuclear physics. This tool provides a method for the determination of properties of the nuclear levels, of the radiation emitted, and of the interactions governing the emission.[23] PAC measurements have also been used in solid state physics, since they yield interesting information about materials and defects. The peculiarity of PAC is that it is a local probe which does not average over macroscopic dimensions, as x-ray diffraction or bulk-conductivity measurements do. Among the various types of angular correlations, the γ–γ correlation is the one most often employed due to the penetrating power of the gamma–ray in condensed matter. The γ–γ perturbed angular correlation spectroscopy has been used to study phenomena such as the defect–impurity association in metals,[24,25,26,27] internal oxidation in metals,[28,29] impurity effects in semiconductors[30,31] and phase identification in compounds.[32,33] An extended compilation of TDPAC measurements on compounds has been performed by Lerf and Butz,[34] and a similar compilation for metals was done by Vianden.[35]

The electric and magnetic fields originating from the surrounding matter are present at the nuclei. These perturbing fields interact with the electric and magnetic moments of the nuclei and often alter the angular correlation pattern of the successive radiations. Through analyzing the perturbed angular correlation, patterns physical quantities like the following can be obtained :

- **Strength of local electromagnetic moments.** The characteristic PAC-frequency ω_1 is propotional to V_{zz}, the component of the field gradient.
- **Symmetry of electric field gradient** (η). η depends on the ratio of the PAC-frequencies ω_1, ω_2, and ω_2. The ratio $\omega_1:\omega_2:\omega_3$ equals 1:2:3 for axial symmetry, whereas $\omega_2 < 2\omega_1$ for nonaxial symmetry .
- **Quality of crystals or microcrystals.** Comparing the linewidth of the PAC-frequency distribution yields information about the quality of different samples.
- **Jump frequency of defects.** The relaxation rate λ in the perturbation function $G_2(t)$, which describes the relaxation rate of the probe, is proportional to τ_c or $1/\tau_c$, for high or low temperatures respectively.
- **Energy barriers for motion of defects or trapping energies (E).** The temperature dependence of the relaxation rate, $\lambda \sim e^{\pm E/kT}$, is used to find the energy barrier.

1.2.1. $^{181}Hf/^{181}Ta$ PAC Measurements in Zirconia

One of the major difficulties in PAC experiments is incorporating the desired radioactive tracer into the materials to be investigated. In the $^{181}Hf/^{181}Ta$ PAC experiments involving zirconia ceramics, this problem has been solved nicely by nature.

Most of the ores containing zirconium also contain about 1 at % or more of hafnium. Owing to the remarkable chemical similarity between zirconium and hafnium, this Hf content is still found in the zirconia ceramics, unless special procedures were taken to remove the hafnium impurity. The similarity between Zr and Hf is due in part to the electronic configurations in the outer shells ($4d^2 5s^2$ and $5d^2 6s^2$ for both zirconium and hafnium) and to the near identity of the atomic radii: 1.452 Å and 1.442 Å, respectively.

The natural ^{180}Hf is transformed into radioactive ^{181}Hf by irradiation with thermal neutrons (see 3.1.6). The unstable isotope ^{181}Hf decays by β emission with a half-life of 43 days to an excited state of ^{181}Ta (Fig. 1.3.). After a half life of 18 μs, this state decays to the ground state by emitting several gamma rays. In this work the cascade emitting γ_1 with 133 keV and γ_2 with 483 keV and a spin sequence of 1/2→ 5/2→ 7/2 is used. The intermediate state, which is the actual PAC probe, has a large quadrupole moment (Q=2.5 b) which interacts with the extra-nuclear field during the state's 10.8 ns half-life (see Table 1.1.). Just as the Hf parent nuclei, the Ta nuclei occupy zirconium sites. The only interaction which has to be taken into account in zirconia ceramics is the electric quadrupole interaction. So PAC with $^{181}Hf/^{181}Ta$ probes samples the electric field gradients (EFG) at a zirconium site.

$^{181}Hf/^{181}Ta$ PAC measurements have been made on various zirconia samples in order to understand, microscopically, the local structures and vacancy dynamics in this system.[36,37,38] $^{181}Hf/^{181}Ta$ PAC measurements have also been used to determine the phase diagram of zirconia-yttria-alloys and the relative number of sites in mixed phase materials.[38,39]

It should be mentioned that instead of ^{181}Ta, ^{111}Cd and other tracers have also been used. [38,41] It is interesting to compare the results gained by various probe nuclei. The interaction between the chosen probe and oxygen vacancies, which have an

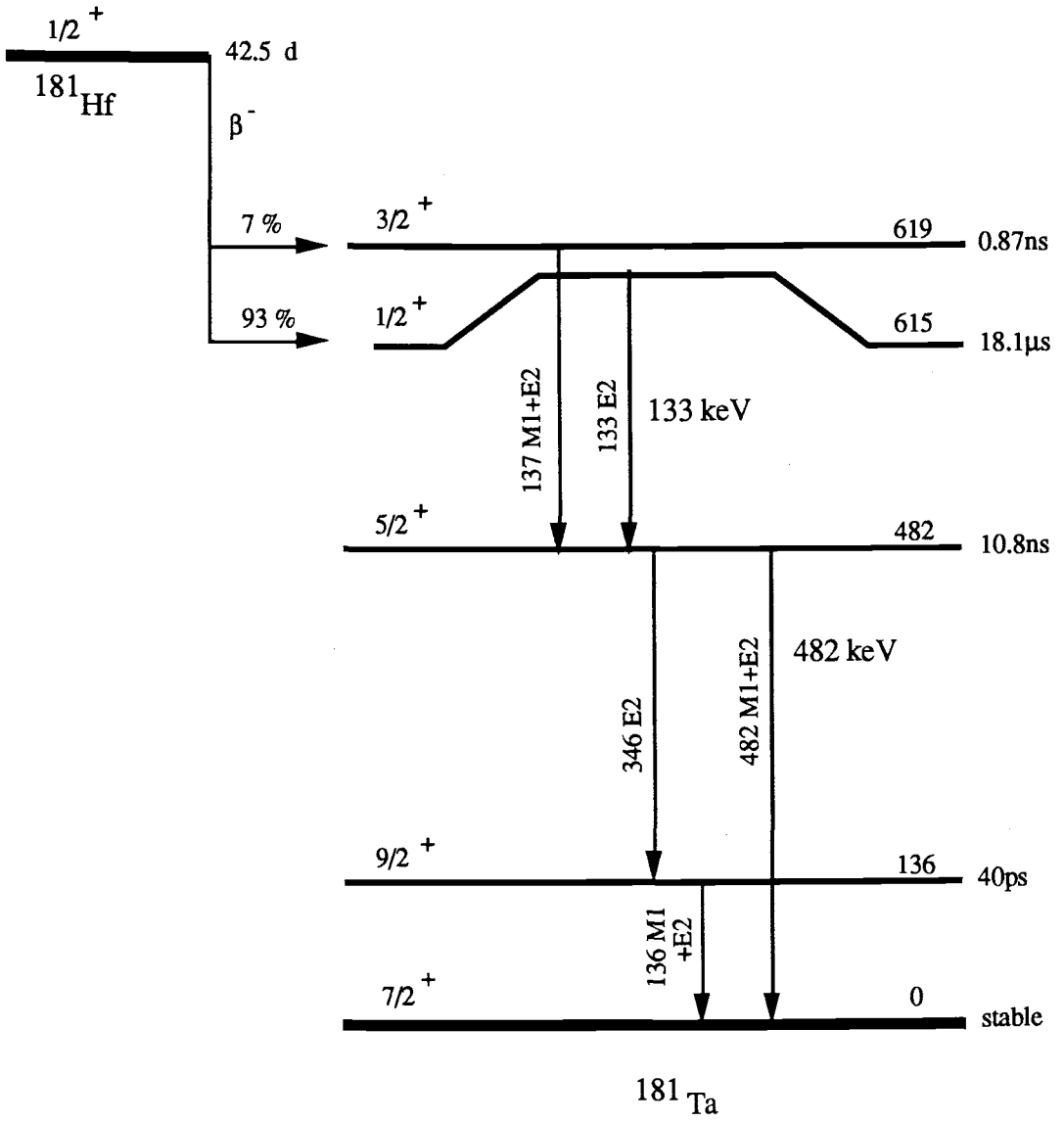

Fig. 1.3. The ^{181}Hf to ^{181}Ta decay schematic diagram.[43]

Unit of Energies is keV. Of interest in this work is the 133 keV-482 keV γ-ray cascade.

Table 1.1. Summary[42] of relevant nuclear characteristics of ^{181}Ta.

Parent half–life (^{181}Hf)	42.5 d
Energies of cascade γ rays:	
γ_1	133 keV
γ_2	482 keV
Nuclear–spin sequence	$1/2^+ \rightarrow 5/2^+ \rightarrow 7/2^+$
Angular–correlation coefficients:	
A_2	-0.295(5)
A_4	-0.069
Intermediate nuclear state:	
Half–life	10.8 ns
Electric quadrupole moment	+ 2.5 b

effective charge of +2 in the anionic sublattice, depends on the effective charges of the probe nuclei in the zirconia cationic lattice. Whereas ^{181}Ta has a 5+ ion core, and thus an effective charge of +1, ^{111}Cd has a formal charge of 2+, meaning an effective charge of -2. By simply considering the Coulomb interaction, one expects that the ^{181}Ta probe repels oxygen vacancies, and divalent dopants like ^{111}Cd attract them. Experiments support this hypothesis.[37,38,39]

In cubic zirconia (stabilized with Y_2O_3 in this experiment), the observed ^{181}Ta PAC spectra exhibit a nonoscillatory pattern.[37,39,40] The EFG experienced by a probe nucleus results from a static contribution due to the surrounding dopant cations and a fluctuating contribution due to the diffusive motion of the oxygen vacancies due to the diffusive motion of the oxygen vacancies.

The fluctuating part of the EFG is negligible near room temperature and above 1200°C. At room temperature, the oxygen diffusion motion is very slow, and therefore the environment is approximately static during the lifetime of the probe. Above 1200°C, the oxygen diffusion is very fast and the fluctuating EFG averages to zero. Thus the EFG is primarily contributed by the static background due to the lattice in these two regimes.

At intermediate temperatures, the relaxation of the probe becomes significant because the oxygen vacancy jump times become comparable to $<\omega_Q^2>^{-1/2}$, the average characteristic interaction time of the probe with the EFG.

As a result of the temperature dependance of the relaxation, the relaxation constant λ shows slow and fast relaxation regimes when plotted as a function of inverse temperature between room temperature and 1300°C. The maximum relaxation occurs near 800°C to 850 °C. The slope of the relaxation constant above 850°C is approximately three times that at low temperatures. Such asymmetry has often been attributed to the existence of two relaxation mechanisms that cross over near the maximum of λ.[37] A more physical explanation suggests that at the long jump time region, the contributions of the vacancies in the more distant shells are not negligible.[39,40] Properly summing the contributions of the different shells does not modify the short jump time region, but changes the slope in the long jump time region. Based on this model, only a single activation energy is needed. The physics of this process is still a matter of interest.

2. Theory of γ-γ Perturbed Angular Correlations

If an atomic or nuclear system decays in a cascade of successive γ-rays, the angular distribution of the radiation has a characteristic pattern.[22] This pattern is influenced by interactions of the intermediate states with their environment. PAC makes use of this feature to yield information about local environments inside the material. In this experiment ZrO_2 (zirconia) in its cubic form was investigated using a $^{181}Hf/^{181}Ta$ PAC probe. The only important interaction between the PAC probe and the extra-nuclear field in this experiment is the interaction between the quadrupole moment of the probe and the electric field gradient (EFG) in the lattice. The reason for that is (i) higher order electric interactions are negligible, (ii) ZrO_2 is a nonmagnetic material and therefore no magnetic interactions have to be taken into account, and (iii) the ^{181}Ta PAC probe has a closed electronic shell (spherical symmetry) and therefore no magnetic or electric dipole moments.

The formalism for static EFG–quadrupole interaction that will be presented in this chapter follows very closely that given by Frauenfelder and Steffen,[44] as summarized by Jaeger[38] and Su[39]. A more modern treatment is given by Steffen and Adler[45] in a form that is more suitable for low temperature work. For the fluctuating EFG's the time-dependent electric quadrupole interaction in liquids[46] and a stochastic model[47] are described.

2.1. The Generalized Angular Correlation Function $W(k_1, k_2, t)$

The probe nuclei of γ-γ PAC measurements decay through a cascade $I_i \rightarrow I \rightarrow I_f$, emitting two gamma rays γ_1 and γ_2. The first γ-ray is used to establish the

quantization axis against which the direction of the second γ-ray is correlated. The three nuclear states with spins I_i, I, and I_f have sublevels m_I which are populated with unequal probabilities during the decay. The angular correlation function $W(\mathbf{k}_1, \mathbf{k}_2, t)$ is defined so that $W(\mathbf{k}_1, \mathbf{k}_2, t)d\Omega_1 d\Omega_2$ is the probability that γ_1 and γ_2 are emitted in directions $\mathbf{k}_1$ and $\mathbf{k}_2$ within the solid angles $d\Omega_1$ and $d\Omega_2$. The time "t" in the perturbed angular correlation function $W(\mathbf{k}_1, \mathbf{k}_2, t)$ is the time separation between these two successive radiations, meaning t=0 is the time at which γ_1 is emitted.

Using the density matrix formalism, ρ_{in} refers to the system in its initial state. At t = 0, γ_1 with polarization σ_1 is emitted. Using the creation and annihilation operators $A^+(\mathbf{k}_1, \sigma_1)$ and $A(\mathbf{k}_1, \sigma_1)$, respectively, the system immediately after emission of γ_1 is described by $\rho(\mathbf{k}_1, 0) = A^+(\mathbf{k}_1, \sigma_1)\, \rho_{in}\, A(\mathbf{k}_1, \sigma_1)$. In the presence of extra-nuclear perturbations, the density matrix of the system after emission of γ_1 will evolve with time, meaning $\rho(\mathbf{k}_1,t) = \Lambda(t)\rho(\mathbf{k}_1,0)\Lambda^+(t)$, where $\Lambda(t)$ is the time evolution operator of the system. After time t, γ_2 with polarization σ_2 is emitted, described by $A^+(\mathbf{k}_2, \sigma_2)$ and $A(\mathbf{k}_2, \sigma_2)$, respectively. $W(\mathbf{k}_1, \mathbf{k}_2, t)$ in its most general form can then be written as

$$W(\mathbf{k}_1,\mathbf{k}_2,t) = \sum_{\sigma_1,\sigma_2} \mathrm{Tr}\left[A^+(\mathbf{k}_2, \sigma_2)\Lambda(t)A^+(\mathbf{k}_1, \sigma_1)\, \rho_{in} A(\mathbf{k}_1, \sigma_1)\Lambda^+(t)A(\mathbf{k}_2, \sigma_2)\right]$$

$$= \sum_{\sigma_1,\sigma_2} \mathrm{Tr}\left[\rho(\mathbf{k}_2,t)\rho(\mathbf{k}_1,t)\right], \qquad (2\text{–}1)$$

where $$\rho(\mathbf{k}_2,t) = A(\mathbf{k}_2,\sigma_2)\rho_{final}A^+(\mathbf{k}_2,\sigma_2) = A(\mathbf{k}_2,\sigma_2)\underline{1}A^+(\mathbf{k}_2,\sigma_2) \qquad (2\text{–}2)$$

is the density function of the system immediately before emission of γ_2. These equations look quite simple, but this entire chapter will be devoted to finding $W(\mathbf{k}_1,\mathbf{k}_2,t)$. In fact, for slowly fluctuating EFGs in solids, the problem of finding an analytical expression for $W(\mathbf{k}_1, \mathbf{k}_2, t)$ still remains unsolved.

To calculate the trace of the product of the two density matrices in equation (2-1) we consider the sublevels m_I, m'_I. These sublevels form a complete set of eigenstates of I^2 and I_z. The angular correlation function is therefore

$$W(\mathbf{k}_1, \mathbf{k}_2, t) = \sum_{\sigma_1,\sigma_2} \sum_{m_1 m_1'} \langle m_1|\rho(\mathbf{k}_1, t)|m_1'\rangle\langle m_1'|\rho(\mathbf{k}_2, t)|m_1\rangle . \qquad (2\text{–}3)$$

If the interaction Hamiltonian which describes the extra-nuclear perturbations is K(t), the time evolution operator of the system, $\Lambda(t)$, obeys the equation

$$\frac{d}{dt}\Lambda(t) = -\frac{i}{\hbar}K(t)\Lambda(t) \quad , \text{with} \quad \Lambda(0)=\underline{1} . \qquad (2\text{–}4)$$

Using this time evolution operator, $\Lambda(t)$, and the closure relation for m_2 and m_2', the matrix element $\langle m_1|\rho(\mathbf{k}_1,t)|m_1'\rangle$ becomes

$$\langle m_1|\rho(\mathbf{k}_1,t)|m_1'\rangle = \sum_{m_2 m_2'}^{n} \langle m_1|\Lambda(t)|m_2\rangle\langle m_2|\rho(\mathbf{k}_1,0)|m_2'\rangle\langle m_1'|\Lambda(t)|m_2'\rangle^* . \qquad (2\text{–}5)$$

In PAC measurements the polarization of the radiation is not observed (expressed by the sum over σ_1 and σ_2). In that case, using the Wigner-Eckart theorem, the matrix elements of $\rho(\mathbf{k}_1, 0)$ and $\rho(\mathbf{k}_2, t)$ can be calculated to be

$$<m_2|\rho(\mathbf{k}_1,0)|m_2'>= \sum_{q_1 N_1} (-1)^{2I-I_i+m_2} A_{q_1}(1) \begin{pmatrix} I & I & k_1 \\ m_2' & -m_2 & N_1 \end{pmatrix} \times\sqrt{4\pi}\, Y^*_{q_1 N_1}(\theta_1,\phi_1) \ , \qquad (2\text{–}6)$$

and

$$<m_1'|\rho(\mathbf{k}_2,t)|m_1>= \sum_{q_2 N_2} (-1)^{k_2-I_f-m_1} A_{q_2}(2) \begin{pmatrix} I & I & k_2 \\ m_1' & -m_1 & N_2 \end{pmatrix} \times\sqrt{4\pi}\, Y_{q_2 N_2}(\theta_2,\phi_2) \ , \qquad (2\text{–}7)$$

where the Wigner 3-j symbols[48] enter each of these expressions. The $Y^*_{q_1 N_1}(\theta_1,\phi_1)$ and $Y_{q_2 N_2}(\theta_2,\phi_2)$ are the spherical harmonics. The numbers $A_{q_1}(1) \equiv A_{q_1}(L_1 L_1' I_i I)$ and $A_{q_2}(2) \equiv A_{q_2}(L_2 L_2' I_f I)$ depend only on the spins of the nuclear states involved in the transition and the multipolarities of the emitted radiations. The overall normalization is $A_0 = 1$. We assumed that no polarizations of the radiation are observed. In that case the angular correlation function $W(\mathbf{k}_1, \mathbf{k}_2, t)$ is also called the directional correlation function. Using the expressions (2-6,7) for the matrix elements of the density matrices, $W(\mathbf{k}_1, \mathbf{k}_2, t)$ becomes

$$W(\mathbf{k}_1, \mathbf{k}_2, t) = 4\pi \sum_{k_1 k_2} \sum_{N_1 N_2} [(2k_1+1)(2k_2+1)]^{-\frac{1}{2}} A_{k_1}(1)\, A_{k_2}(2)\, G^{N_1 N_2}_{k_1 k_2}(t) \times Y^*_{k_1 N_1}(\theta_1,\phi_1)\, Y_{k_2 N_2}(\theta_2,\phi_2) \ . \qquad (2\text{–}8)$$

Equation (2-8) defines the so-called perturbation function $G_{k_1k_2}^{N_1N_2}(t)$, which contains all the information about the interaction between the PAC probe and the extra-nuclear field:

$$G_{k_1k_2}^{N_1N_2}(t) = \sum_{m_1 m_1' m_2 m_2'} (-1)^{2I+m_1+m_2}[(2k_1+1)(2k_2+1)]^{\frac{1}{2}} \begin{pmatrix} I & I & k_1 \\ m_2' & -m_2 & N_1 \end{pmatrix} \times \begin{pmatrix} I & I & k_2 \\ m_1' & -m_1 & N_2 \end{pmatrix} < m_1|\Lambda(t)|m_2 >< m_1'|\Lambda(t)|m_2' > \ . \quad (2\text{–}9)$$

The name "perturbation" indicates that this interaction perturbs the angular correlation of a free nucleus.

2.2. Angular Correlation for Free Nuclei

If there are no interactions between the intermediate state of the PAC probe and the environment during the transition $I_i \rightarrow I \rightarrow I_f$, the time evolution operator $\Lambda(t)$, as defined in (2–2), becomes unity. Therefore

$$<m_1|\Lambda(t)|m_2><m_1'|\Lambda(t)|m_2'> = \delta_{m_1 m_2}\delta_{m_1' m_2'} \ . \quad (2\text{–}10)$$

So $m_1 = m_2$, and we can use the orthogonality of the 3j-symbols:[36]

$$\sum_{m_1 m_1'} \begin{pmatrix} I & I & k_1 \\ m_1' & -m_1 & N_1 \end{pmatrix} \begin{pmatrix} I & I & k_2 \\ m_1' & -m_1 & N_2 \end{pmatrix} = (2k_1+1)^{-1}\delta_{k_1k_2}\delta_{N_1N_2} \ . \quad (2\text{–}11)$$

Now equations (2-9, 10, 11) give a simple expression for $G_{k_1 k_2}^{N_1 N_2}(t)$:

$$G_{k_1 k_2}^{N_1 N_2}(t) = \delta_{k_1 k_2} \delta_{N_1 N_2} \ . \tag{2–12}$$

The physical averaging over the directions of $\mathbf{k}_1$, keeping only the information about the angle θ between $\mathbf{k}_1$ and $\mathbf{k}_2$, reduces the summation over N_1 and N_2 in (2-8) to (2k+1). Furthermore, equation (2-12) for free nuclei reduces the general formula for $W(\mathbf{k}_1, \mathbf{k}_2, t)$ considerably, because it allows us to use the Addition theorem for spherical harmonics to obtain

$$W(\theta) = \sum_{k=0,\text{even}}^{k_{max}} A_k(1)\, A_k(2)\, P_k(\cos\theta) = \sum_{k=0,\text{even}}^{k_{max}} A_{k\,k} P_k(\cos\theta) \ . \tag{2–13}$$

The $P_k(\cos\theta)$, the usual Legendre polynomials, contain all the angular dependence of the unperturbed (free nuclei) angular correlation function. The selection rule of the 3-j symbols restricts the value of the summation index k:

$$0 \le k \le 2I \ . \tag{2–14}$$

For spin I=5/2 states, as used in this experiment, k_{max} is equal to 4, and the angular-correlation coefficient A_4 is much smaller than A_2. The reason that the summation contains only even values of k up to k_{max} is that the circular polarization of the emitted radiation is not observed.

2.3. Static Perturbations

2.3.1. Static Perturbations of Single Nuclei

If there is an interaction (perturbation) between the probe nucleus and its environment, but the interaction does not change during the lifetime of the intermediate state I, the time evolution operator (2-2) becomes

$$\Lambda(t) = \exp(-\frac{i}{\hbar} K t) \ . \qquad (2\text{–}15)$$

The time–independent interaction Hamiltonian K can be diagonalized by a unitary operator U. The diagonal elements are the energy eigenvalues E_n. The time evolution operator $\Lambda(t)$ can then be written as

$$\Lambda(t) = U^{-1} e^{-\frac{i}{\hbar} E t} U \ , \qquad (2\text{–}16)$$

and the matrix elements of $\Lambda(t)$ become

$$< m_1 | \Lambda(t) | m_2 > = \sum_n < n | m_1 > * < n | m_2 > \exp(-\frac{i}{\hbar} E_n t) \ , \qquad (2\text{–}17)$$

where the vectors |n> are the eigenstates of the diagonalized Hamiltonian, describing the n^{th} sublevels of the intermediate state. So the result of the angular perturbation function (2-9) for a single nucleus in the case of a static perturbation is:

$$G_{k_1k_2}^{N_1N_2}(t) = \sum_{m_1m_1'm_2m_2'} \sum_{nn'} (-1)^{2I+m_1+m_2}[(2k_1+1)(2k_2+1)]^{\frac{1}{2}} \begin{pmatrix} I & I & k_1 \\ m_1' & -m_1 & N_1 \end{pmatrix}$$

$$\times \begin{pmatrix} I & I & k_2 \\ m_2' & -m_2 & N_2 \end{pmatrix} \exp[-\tfrac{i}{\hbar}(E_n - E_{n'})t] < n|m_1 > * < n|m_2 >< n'|m_1' >< n'|m_2' > * . \quad (2\text{–}18)$$

2.3.2. Static Perturbations in Polycrystalline Materials

A powder can be considered as a large number of randomly oriented microcrystals. So the principal axes in the various microcrystals have different directions. Let $D(\Omega)$ be the rotation matrix that transforms from the lab coordinate frame $\mathbf{z}$ through a set of prescribed Euler angles $\Omega = (\phi, \theta, \gamma)$ to the principal axes system $\mathbf{z}'$ of a microcrystal:

$$K(z') = D(\Omega)\, K(z)\, D^{-1}(\Omega) \ . \quad (2\text{–}19)$$

If U is the unitary operator which diagonalizes $K(\mathbf{z}')$, then the matrix elements of $\Lambda(t)$ become

$$\Lambda(t) = D^{-1}(\Omega)\, U^{-1} \exp(-\tfrac{i}{\hbar} Et)\, U\, D(\Omega) \ , \quad (2\text{–}20)$$

and the matrix elements of $\Lambda(t)$ can be rewritten as

$$< m_1|\Lambda(t)|m_2 > = \sum_{m_1'm_2'n} < n|m_1' >^* < n|m_2' > \exp(-\tfrac{i}{\hbar} E_n t) D^I_{m_1'm_1}{}^* (\Omega) D^I_{m_2'm_2}(\Omega) \ . \quad (2\text{–}21)$$

The terms of type $D^{I}_{m_i' m_i} = \langle m_i' | D(\Omega) | m_i \rangle$ are the matrix elements for the rotation operator. For these matrix elements we can apply a very useful contraction relation:[48]

$$\begin{pmatrix} j_1 & j_2 & j \\ m_1' & m_2' & m' \end{pmatrix} D^{j}_{mm'}{}^{*} = \sum_{m_1 m_2} \begin{pmatrix} j_1 & j_2 & j \\ m_1 & m_2 & m \end{pmatrix} D^{j_1}_{m_1 m_1'} D^{j_2}_{m_2 m_2'} \,. \tag{2–22}$$

Using (2-23) and summing over all sublevels m_1, m_1', m_2 and m_2', we find the perturbation function of each of the microcrystals:

$$\begin{aligned} G^{N_1 N_2}_{k_1 k_2}(t) = \sum_{\substack{m_1 m_2 \\ m_1' m_2'}} \sum_{nn'} (-1)^{2I+m_1+m_2} [(2k_1+1)(2k_2+1)]^{\frac{1}{2}} \exp[-\tfrac{i}{\hbar}(E_n - E_{n'})t] \\ \times \begin{pmatrix} I & I & k_1 \\ m_1' & -m_1 & p_1 \end{pmatrix} \begin{pmatrix} I & I & k_2 \\ m_2' & -m_2 & p_2 \end{pmatrix} D^{k_1}_{p_1 N_1}{}^{*}(\Omega) D^{k_2}_{p_2 N_2}(\Omega) \\ \times \langle n | m_1 \rangle^{*} \langle n' | m_1' \rangle \langle n | m_2 \rangle \langle n' | m_2' \rangle^{*} \,. \end{aligned} \tag{2–23}$$

Each one of the microcrystals has a different rotation matrix. To obtain the perturbation function of the whole powder, we have to average over all contributions, corresponding to the different orientations of the principal axis. If we use the orthogonality relation for the rotation matrices,

$$\int d\Omega \, D^{j_1}_{m_1 m_1}{}^{*}(\Omega) \, D^{j_2}_{m_2 m_2}(\Omega) = \frac{1}{2j_1+1} \delta_{j_1 j_2} \delta_{m_1 m_2} \delta_{m_1' m_2'} \,, \tag{2–24}$$

the resulting angular perturbation function is

$$G_{kk}(t)=\sum_{\substack{m_1m_2\\ m_1'm_2'}}\sum_{nn'}(-1)^{2I+m_1+m_2}\begin{pmatrix}I & I & k\\ m_1' & -m_1 & N\end{pmatrix}\begin{pmatrix}I & I & k\\ m_2' & -m_2 & N\end{pmatrix}$$

$$\times\exp[-\tfrac{i}{\hbar}(E_n-E_{n'})t]<n|m_1>^*<n'|m_1'><n|m_2><n'|m_2'>^* . \qquad (2\text{–}25)$$

This can be written as

$$G_{kk}(t)=\delta_{k_1k_2}\delta_{N_1N_2}\delta_{p_1p_2}\sum_{nn'}S_{nn'}^{kk}\exp[-\tfrac{i}{\hbar}(E_n-E_{n'})t] , \qquad (2\text{–}26)$$

using the coefficients $S_{nn'}^{kk}$ which are defined as

$$S_{nn'}^{k_1k_2}=\sum_{\substack{m_1m_2\\ m_1'm_2'}}(-1)^{2I+m_1+m_2}\begin{pmatrix}I & I & k_1\\ m_1' & -m_1 & N\end{pmatrix}\begin{pmatrix}I & I & k_2\\ m_2' & -m_2 & N\end{pmatrix}$$

$$\times<n|m_1>^*<n'|m_1'><n|m_2><n'|m_2'>^* . \qquad (2\text{–}27)$$

Comparing (2-25) with the single-crystal result in (2–17), the perturbation function for the polycrystalline sample can be regarded as the average of the perturbation function of the single-crystal in the following way:

$$G_{kk}(t)=\frac{1}{2k+1}\sum_{N}G_{kk}^{NN}(t) . \qquad (2\text{–}28)$$

The sum in (2-26) over all sublevels n and n' can be separated and the equation rewritten as

$$G_{kk}(t) = \sum_{n} S_{nn}^{kk} + \sum_{n \neq n'} S_{nn'}^{kk} \cos\left[\frac{(E_n - E_{n'})t}{\hbar}\right] . \qquad (2\text{–}29)$$

Inserting (2–29) in the expression for the angular correlation function (2–8), the summation over N_1, N_2 can be performed since the perturbation function is independent of N_1 and N_2. The addition theorem for the spherical harmonics can also be applied to (2–8), and the angular correlation displayed by a polycrystalline sample has the form

$$W(\theta,t) = \sum_{k=0,\text{even}}^{k_{max}} A_{kk} G_{kk}(t) P_k(\cos\theta) . \qquad (2\text{–}30)$$

An important feature of the perturbation function (2–29) for the polycrystalline sample is the time independent term $\sum_{n} S_{nn}^{kk}$. Because of this term, the angular correlation of a polycrystalline sample is never completely destroyed under the influence of static perturbing fields. For this reason, this term has historically been called the "hard–core".

2.4. The Static Electric Quadrupole Interaction

To find the energies E_n and $E_{n'}$ which are needed to calculate the angular perturbation function for a static perturbation in a powder source (2-29), the Hamiltonian for the static electric interactions between the nucleus of the PAC probe and its environment has to be considered. Since ZrO_2 is a nonmagnetic material, no magnetic interactions have to be taken into account. Assuming the nucleus is surrounded by point charges, the Hamiltonian for the static interaction can be written as

$$H_{EI} = \sum_{ij} \frac{e_i e_j}{|r_i - r_j|} , \qquad (2\text{–}31)$$

where the quantities with index "i" are the charges and coordinates of the nucleus and the quantities with index j are those of its environment. Using the usual multipole expansion for the case $r_j > r_i$, the Hamiltonian becomes

$$H_{EI} = \sum_{ij} \sum_{k=0}^{\infty} \frac{e_i e_j r_i^k}{r_j^{k+1}} P_k(\cos\theta_{ij}) . \qquad (2\text{–}32)$$

Here θ_{ij} is the angle between a pair of $\mathbf{r}_i$ and $\mathbf{r}_j$. Applying the addition theorem of spherical harmonics to (2–33) yields

$$H_{EI} = 4\pi \sum_{k=0}^{\infty} \frac{1}{2k+1} \sum_{\mu} (-1)^{\mu} \sum_{i} e_i r_i^k Y_{k\mu}(\theta_i,\phi_i) \sum_{j} e_j \frac{1}{r_j^{k+1}} Y_{k-\mu}(\theta_j,\phi_j) . \qquad (2\text{–}33)$$

To achieve a more compact form, the tensor operators of the nuclear moments, $q^{(k)}$, and of the electric fields, $V^{(k)}$,.are introduced.[49] The definitions for these tensor operators are

$$q_{\mu}^{(k)} = \sum_{i} e_i r_i^k Y_{k\mu}(\theta_i,\phi_i) \quad \text{and} \quad V_{\mu}^{(k)} = \sum_{j} e_j \frac{1}{r_j^{k+1}} Y_{k-\mu}(\theta_j,\phi_j) . \qquad (2\text{–}34)$$

Using the definition of the scalar product of two tensor operators,

$$q^{(k)} \bullet V^{(k)} = \sum_{\mu=-k}^{k} (-1)^{\mu} q_{\mu}^{(k)} V_{-\mu}^{(k)} , \qquad (2\text{–}35)$$

the Hamiltonian can now be expressed as a product of two factors: a nuclear factor and an external field factor

$$H_{EI} = \sum_{k=0}^{\infty} \frac{4\pi}{2k+1} q^{(k)} \bullet V^{(k)} . \qquad (2\text{–}36)$$

The only term that needs to be retained in this infinite sum is the the electric quadrupole term and its corresponding interaction. The reason for that is that (i) the odd-order electric moments vanish due to the requirement of parity conservation under reflection, and (ii) the effects of nuclear electric hexadecapole moment or higher order terms are too small to be considered. The remaining Hamiltonian H_{QI} is

$$H_{QI} = \frac{4}{5}\pi V^{(2)} \bullet q^{(2)} = \frac{4}{5}\pi \sum_{\mu=-2}^{2} (-1)^{\mu} q_{\mu}^{(2)} V_{-\mu}^{(2)} . \qquad (2\text{–}37)$$

In (2-37), $q^{(2)}$ is the second–rank tensor operator of the nuclear quadrupole moment. The quadrupole term in the multipole expansion of the electric field, $V^{(2)}$, is often called the classical electric field gradient operator (EFG). The matrix elements of the quadrupole Hamiltonian (2–37) are

$$<Im|H_{QI}|Im'>=\frac{4\pi}{5}\sum_{\mu=-2}^{2}(-1)^{\mu}<Im|q_{\mu}^{(2)}|Im'>V_{-\mu}^{(2)}\ . \qquad (2\text{–}38)$$

The matrix elements of the quadrupole moment tensor $q_{\mu}^{(2)}$ can be evaluated using the Wigner–Eckart theorem:[48]

$$<Im|q_{\mu}^{(2)}|Im'>=(-1)^{I-m}\begin{pmatrix} I & I & 2 \\ m' & -m & \mu \end{pmatrix}<I||q^{(2)}||I>\ . \qquad (2\text{–}39)$$

The conventional definition of the nuclear quadrupole moment,[50]

$$eQ=\sqrt{\frac{16\pi}{5}}<II|q_{0}^{(2)}|II>\ , \qquad (2\text{–}40)$$

allows us to calculate the reduced matrix element $<I||q^{(2)}||I>$:

$$<I||q^{(2)}||I>=\sqrt{\frac{16\pi}{5}}\begin{pmatrix} I & I & 2 \\ I & -I & 0 \end{pmatrix}^{-1}eQ\ . \qquad (2\text{–}41)$$

Equations (2-39) and (2-41) then yield the matrix elements of the the quadrupole moment tensor:

$$<Im|q_{\mu}^{(2)}|Im'>=(-1)^{I-m}\sqrt{\frac{5}{16\pi}}eQ\begin{pmatrix} I & I & 2 \\ m' & -m & \mu \end{pmatrix}\begin{pmatrix} I & I & 2 \\ I & I & 0 \end{pmatrix}^{-1}\ . \qquad (2\text{–}42)$$

With this result, only the terms of the form $V_\mu^{(2)}$ remain to be calculated in equation (2-38). Using the definition of the tensor operator $V^{(k)}$ from (2-34), we can write the contribution of an external charge e_j to $V^{(2)}$ as

$$V_\mu^{(2)} = \frac{e_j}{r_j^3} Y_{2\ -\mu}(\theta,\phi) \ . \tag{2–43}$$

These spherical components $V_\mu^{(2)}$ can be written in terms of the Cartesian derivatives V_{xx}, V_{xy}, and V_{zz}, where the notation, $V_{xy} = \frac{\partial^2 V}{\partial x \partial y}$, etc., is used. In a principal-axis system, the cross derivatives equal zero, and conventionally the coordinate system is chosen such that $|V_{xx}| \le |V_{yy}| \le |V_{zz}|$. If we define the asymmetry parameter η as

$$\eta = \frac{V_{xx} - V_{yy}}{V_{zz}} \ , \tag{2–44}$$

then EFG components (Cartesian components of $V_\mu^{(2)}$) can be characterized by two parameters, the magnitude V_{zz} and the asymmetry parameter η:

$$V_0^{(2)} = \sqrt{\frac{5}{16\pi}}\, V_{zz} \ , \tag{2–45a}$$

$$V_{\pm 1}^{(2)} = 0 \ , \tag{2–45b}$$

$$V_{\pm 2}^{(2)} = \sqrt{\frac{5}{96\pi}}\,(V_{xx} - V_{yy}) = \sqrt{\frac{5}{96\pi}}\,\eta\, V_{zz} \ . \tag{2–45c}$$

Expressing the EFG components in Cartesian derivatives and using the conventional definition of the quadrupole frequency ω_Q,

$$\omega_Q = \frac{e\,Q\,V_{zz}}{4I(2I-1)\hbar}\ , \tag{2–46}$$

the non–vanishing matrix elements of the quadrupole Hamiltonian (2-38) are

$$< Im \pm 2 | H_{QI} | Im >= \hbar\omega_Q \frac{\eta}{2} [(I \pm m + 1)(I \pm m + 2)(I \mp m + 1)(I \mp m)]^{\frac{1}{2}} \tag{2–47}$$

and

$$< Im | H_{QI} | Im >= \hbar\omega_Q [3m^2 - I(I+1)]\ . \tag{2–48}$$

2.4.1. Static Electric Quadrupole Interaction for Axially Symmetric EFG

For the axially symmetric case, $\eta = 0$, the non-diagonal matrix elements of the quadrupole Hamiltonian (2-47) are equal to zero. The Hamiltonian is diagonal with eigenvalues (2-48):

$$E_m = \hbar\omega_Q [3m^2 - I(I+1)]\ . \tag{2–49}$$

There are (2 I + 1)/2 (for half–integer I) or I +1 (for integer I) distinct energy values since the $\pm$ m levels are doubly degenerate. The perturbation function (2–30) for a polycrystalline sample with axially symmetric electric quadrupole interaction is therefore

$$G_{k\,k}(t) = \sum_m S^{k\,k}_{m\,m} + \sum_{m \neq > m'} S^{k\,k}_{m\,m'} \cos[3\omega_Q (m^2 - m'^2)t]\ . \tag{2–50}$$

Introducing a new index $n = |\, m^2 - m'^2 \,|/2$ (for half–integer I) or $n = |\, m^2 - m'^2 \,|$ (for integer I) and defining

$$S_{k\,n} = \sum_{m\,m'} S^{k\,k}_{m\,m'} = \sum_{m\,m'} \begin{pmatrix} I & I & k \\ m' & -m & p \end{pmatrix}^2 , \qquad (2\text{–}51)$$

the angular perturbation function (2–50) becomes

$$G_{k\,k}(t) = S_{k0} + \sum_{n>0} S_{k\,n} \cos(n\omega_0 t) \ . \qquad (2\text{–}52)$$

The angular frequency ω_0, equivalent to the smallest non–vanishing energy difference, is equal to $6\omega_Q$ (for half–integer I) or $3\omega_Q$ (for integer I). Because of the definition of $G_{kk}(t)$, we have $\sum_n S_{k\,n} = 1$.

2.4.2. Static Electric Quadrupole Interaction for Non-Axially Symmetric EFG for the Case of an Intermediate State with I = 5/2

If the interaction Hamiltonian is not axially symmetric, it has to be diagonalized to find the energy eigenvalues. In general it is difficult to diagonalize the Hamiltonian matrix. To simplify the task, we will concentrate only on the case I = 5/2, which is the nuclear spin of the intermediate state in ^{181}Ta, used in this experiment. The Hamiltonian (2-47) and (2-48) in matrix form for I = 5/2 is

$$H_{QI} = \hbar\omega_Q \begin{pmatrix} 10 & 0 & \eta\sqrt{10} & 0 & 0 & 0 \\ 0 & -2 & 0 & 3\eta\sqrt{2} & 0 & 0 \\ \eta\sqrt{10} & 0 & -8 & 0 & 3\eta\sqrt{2} & 0 \\ 0 & 3\eta\sqrt{2} & 0 & -8 & 0 & \eta\sqrt{10} \\ 0 & 0 & 3\eta\sqrt{2} & 0 & -2 & 0 \\ 0 & 0 & 0 & \eta\sqrt{10} & 0 & 10 \end{pmatrix} . \qquad (2\text{–}53)$$

The secular equation of this Hamiltonian is

$$E^3 - 28E\left\{\eta^2 + 3\right\}(\hbar\omega)^2 - 160\left\{1 - \eta^2\right\}(\hbar\omega)^3 = 0 \ . \qquad (2\text{–}54)$$

The eigenvalues of the quadrupole Hamiltonian in the case of non-axial symmetry are therefore found by solving this cubic equation and can be expressed in the form

$$E_{\pm\frac{5}{2}} = 2\alpha\hbar\omega_Q \cos[\tfrac{1}{3}\cos^{-1}\beta] \ , \qquad (2\text{–}55a)$$

$$E_{\pm\frac{3}{2}} = -2\alpha\hbar\omega_Q \cos[\tfrac{1}{3}(\pi + \cos^{-1}\beta)] \ , \qquad (2\text{–}55b)$$

$$E_{\pm\frac{1}{2}} = -2\alpha\hbar\omega_Q \cos[\tfrac{1}{3}(\pi - \cos^{-1}\beta)] \ , \qquad (2\text{–}55c)$$

$$\text{with} \qquad \alpha = \sqrt{\tfrac{28}{3}(\eta^2 + 3)} \quad \text{and} \quad \beta = \frac{80(1 - \eta^2)}{\alpha^3} \ . \qquad (2\text{–}56)$$

As before, we introduce the index $n = |\, m^2 - m'^2 \,|/2$, and the expression of the perturbation factor for polycrystalline samples (2-30) becomes

$$G_{k\,k}(t) = S_{k\,0}(\eta) + \sum_{n=1}^{3} S_{k\,n}(\eta) \cos[\, \omega_n(\eta) t \,] \ . \qquad (2\text{–}57)$$

The PAC frequencies ω_n are the differences of the energy eigenvalues in (2–57)

$$\omega_1 = \frac{|E_{3/2} - E_{1/2}|}{\hbar} = 2\sqrt{3}\,\alpha\omega_Q \sin[\tfrac{1}{3}\cos^{-1}\beta\,]\,, \tag{2–58a}$$

$$\omega_2 = \frac{|E_{5/2} - E_{3/2}|}{\hbar} = 2\sqrt{3}\,\alpha\omega_Q \sin[\tfrac{1}{3}(\pi - \cos^{-1}\beta)]\,, \tag{2–58b}$$

$$\omega_3 = \frac{|E_{5/2} - E_{1/2}|}{\hbar} = 2\sqrt{3}\,\alpha\omega_Q \sin[\tfrac{1}{3}(\pi + \cos^{-1}\beta)]\,, \tag{2–58c}$$

with the sum rule $\omega_3 = \omega_1 + \omega_2$. Note that these frequencies are functions of α and β and therefore also functions of the asymmetry parameter η (2–56). The eigenvalues of H_{QI} and the PAC frequencies of the quadrupole interaction as a function of η for I = 5/2 are shown in Fig. 2.1.

The coefficients S_{kn} in equation (2-58) can be expressed in terms of the coefficients $S_{n\,n'}^{k\,k}$, which we defined for the general angular perturbation function (2-27):

$$S_{kn} = S_{kn}(\eta) = \sum_{m\,m'} S_{m\,m'}^{k\,k}\,. \tag{2–59}$$

The η-dependance of S_{kn} has been calculated[51] and the coefficients S_{kn} for several values of η are given in Table 2.1.

In equation (2-58) for the angular perturbation function $G_{kk}(t)$, both ω_n and S_{kn} are functions of η. So $G_{kk}(t)$ itself depends on the asymmetry parameter η of the EFG in a sample. Calculated perturbation functions $G_{22}(t)$ for different values of η are shown in Fig. 2.2.

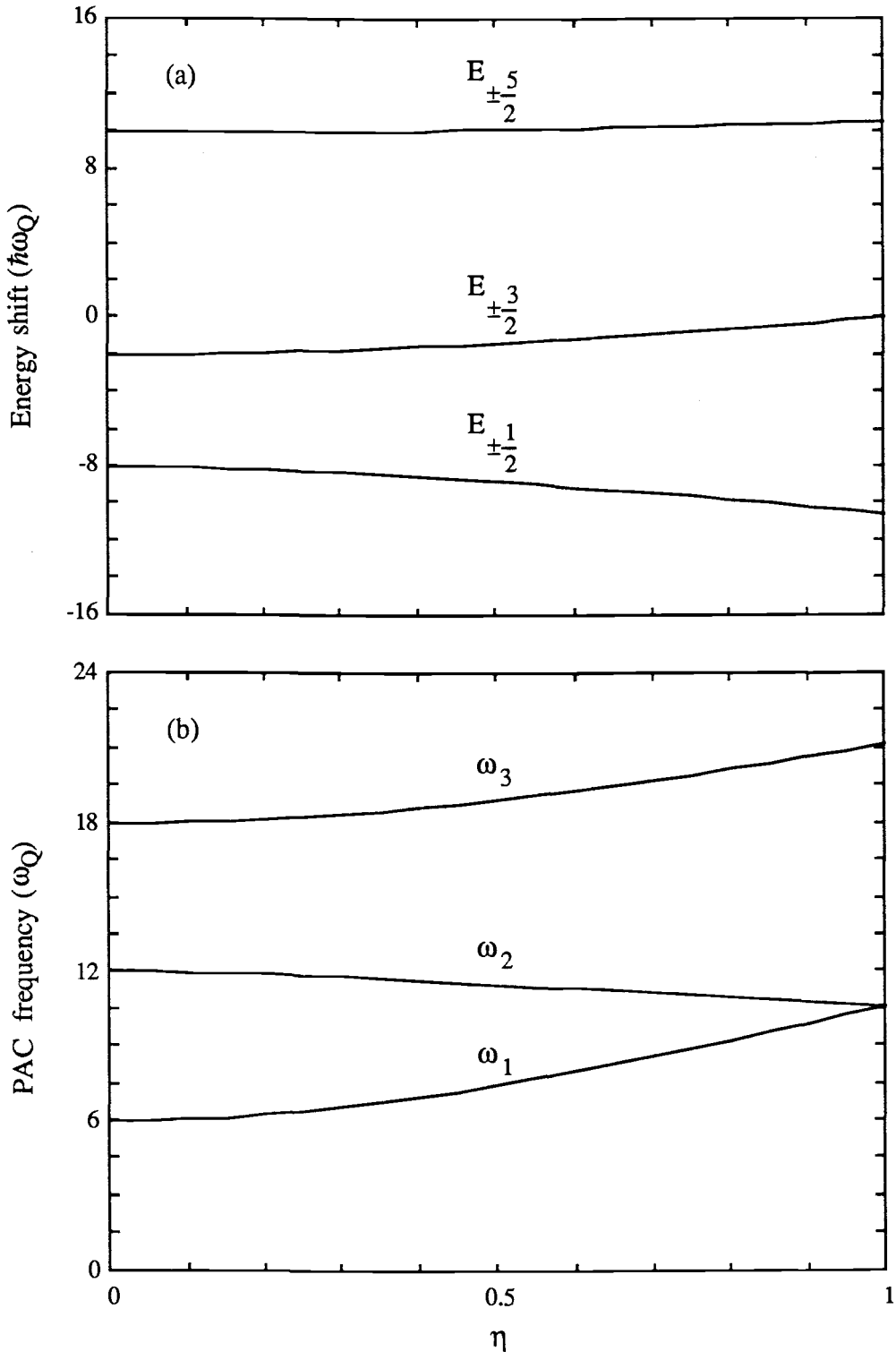

Fig. 2.1. (a) Eigenvalues and (b) PAC frequencies of the H_{QI} as functions of η for I = 5/2. The eigenstates are doubly degenerate.

Table 2.1. Coefficients S_{kn} (k = 2, 4) for a general static H_{QI} as a function of η with I = 5/2.

η	S_{20} S_{40}	S_{21} S_{41}	S_{22} S_{42}	S_{23} S_{43}
0.0	0.2000 0.1111	0.3714 0.2381	0.2857 0.2857	0.1429 0.3651
0.1	0.2024 0.1098	0.3688 0.2395	0.2855 0.2858	0.1432 0.3649
0.2	0.2090 0.1061	0.3617 0.2435	0.2850 0.2861	0.1443 0.3643
0.3	0.2181 0.1010	0.3517 0.2491	0.2844 0.2864	0.1458 0.3634
0.4	0.2280 0.0955	0.3405 0.2553	0.2840 0.2867	0.1474 0.3625
0.5	0.2373 0.0904	0.3296 0.2613	0.2841 0.2866	0.1490 0.3617
0.6	0.2451 0.0860	0.3198 0.2668	0.2847 0.2863	0.1504 0.3609
0.7	0.2511 0.0827	0.3113 0.2715	0.2861 0.2855	0.1515 0.3603
0.8	0.2552 0.0804	0.3044 0.2753	0.2882 0.2844	0.1522 0.3599
0.9	0.2576 0.0791	0.2988 0.2784	0.2910 0.2828	0.1526 0.3596
1.0	0.2583 0.0787	0.2945 0.2808	0.2945 0.2808	0.1528 0.3596

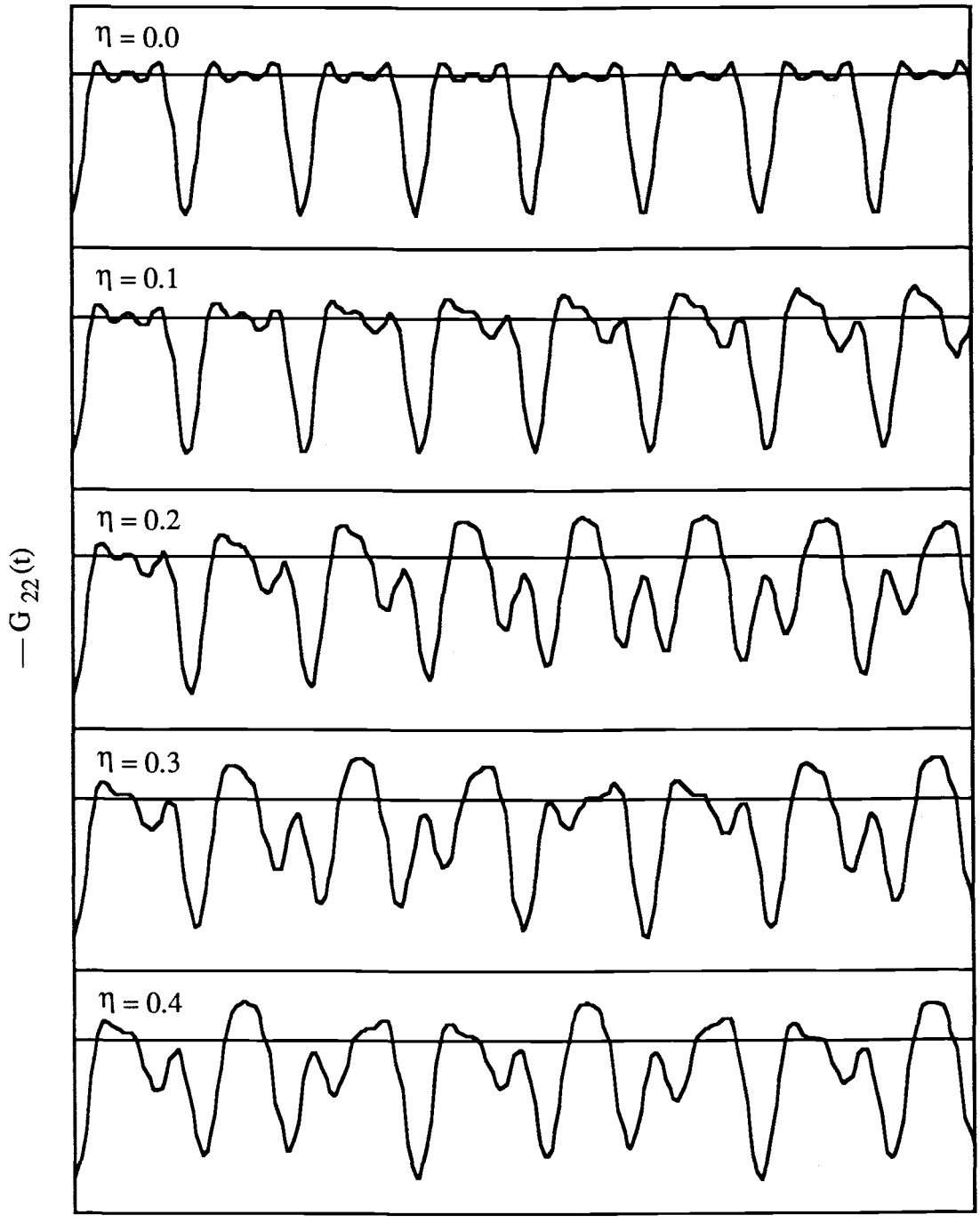

Fig. 2.2. Theoretical $G_{22}(t)$ for a static H_{QI} with I = 5/2 as a function of η.

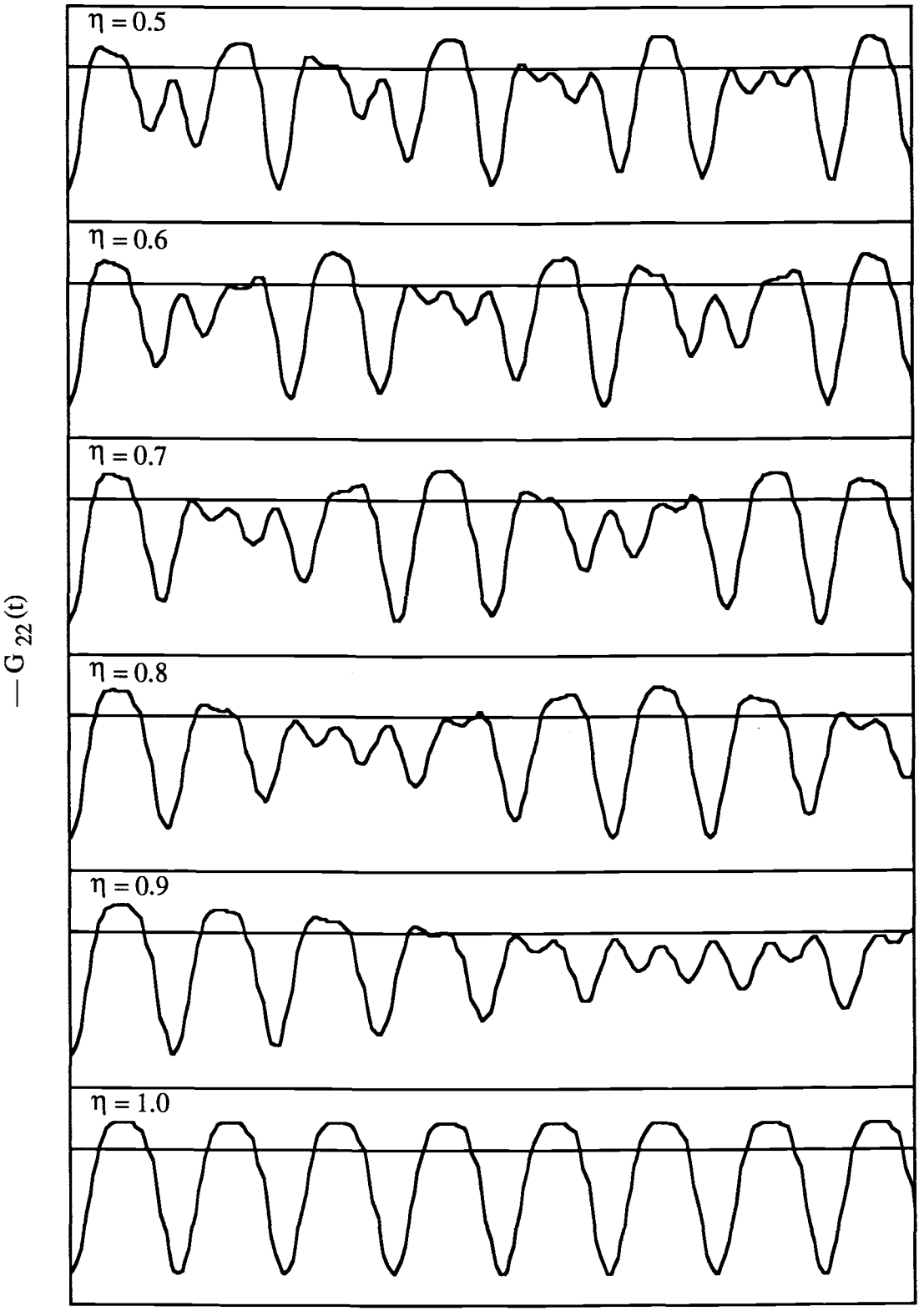

Fig. 2.2. (continued)

2.4.3. Line Broadening of EFG Distribution

So far we have assumed that all the microcrystals contained in a polycrystalline sample are perfect. But in real materials, there are always random imperfections such as impurities or lattice defects. Small variations of the electric field gradient result from these imperfections. Consequently, the Fourier transforms of the experimentally measured angular distribution functions display a distribution of frequencies, rather than an ideally sharp frequency spectrum with frequencies ω_n. To account for these random variations, several distribution models for the EFG have been proposed.[38,39,52]

In this research, a Gaussian distribution was used. Let $P(\omega - \omega_0)$ be the normalized distribution function

$$P(\omega-\omega_0)=\frac{1}{\sqrt{2\pi}\,\sigma}\exp\left\{-\left[\frac{(\omega-\omega_0)}{\sqrt{2}\,\sigma}\right]^2\right\}, \qquad (2\text{–}60)$$

where ω_0 is the peak frequency, and σ is the distribution width or standard deviation. Then the model for the measured perturbation function $G_{kk}^{measured}$ is the convolution of the theoretical perturbation function G_{kk}^{theory} (2-58) and the distribution function $P(\omega - \omega_0)$:

$$G_{kk}^{measured}(t) = \int d\omega\; G_{kk}^{theory}(t)\; P(\omega-\omega_0)\;. \qquad (2\text{–}61)$$

If we define the relative width of the frequency distribution, $\delta = \frac{\sigma}{\omega_n^0}$, where the frequencies ω_n^0 are the peak frequencies, obtained from computer fits to the experimental data (see 4.2.2.), then the solution of the integral (2-61) is

$$G_{kk}^{measured}(t) = S_{k0}(\eta) + \sum_{n=1}^{3} S_{kn}(\eta) \cos\left[\omega_n^0(\eta) t\right] \exp\left[-\frac{\left(\delta \omega_n^0 t\right)^2}{2}\right] . \qquad (2\text{–}62)$$

This model for the measured perturbation function can be regarded as the solution for the ideal perturbation function multiplied by a Gaussian damping term. Due to this damping, the higher frequency terms, ω_2 and ω_3, damp out faster than the lower frequency term ω_1.

2.5. Time-Dependent Perturbations

If the environment of the PAC probe changes during the lifetime of the intermediate state, the Hamiltonian H(t) which describes the extra-nuclear perturbations becomes time-dependent. The time-evolution operator, $\Lambda(t)$, governing the evolution of the system, obeys the equation

$$\frac{d}{dt}\Lambda(t) = -\frac{i}{\hbar} H(t)\, \Lambda(t) . \qquad (2\text{–}63)$$

To find $\Lambda(t)$ and the corresponding matrix elements in the case of time-dependent extra-nuclear fields is not as easy as it was for free nuclei (2-10) or for static perturbations

(2-14). The reason for the complications is that the Hamiltonian at time t_1 $H(t_1)$ does not in general commute with the Hamiltonian $H(t_2)$ at a different time t_2.

Nevertheless, the problem has been solved for liquids[46] and for fast fluctuating EFGs in powder sources.[47]

2.5.1. Time-Dependent Electric Quadrupole Interaction in Liquids

The time-dependent interaction due to random Brownian motion of ions in liquids is discussed here, because it reveals interesting features of the angular perturbation function for fluctuating EFGs, which will be of interest for solid materials also.

Abragam and Pound calculated the angular perturbation function $G_{kk}(t)$ for liquids[46] under the assumption that the fluctuation rate of the EFG, $1/\tau_c$, is much higher than the the transition rate, $< \omega_Q^2 >^{-1/2}$, between the sublevels of the intermediate state I. Another way to express that is to say that the observation time, meaning the lifetime of the intermediate state, $< \omega_Q^2 >^{1/2}$, is long compared to the characteristic fluctuation time of the perturbing fields, τ_c. This assumption is reasonable, because for nonviscous liquids such as water or dilute aqueous solutions, $\tau_c \approx 10^{-11}$ s, which is considerably shorter than the lifetime of the intermediate state of typical PAC probes (for ^{181}Ta $\tau_c \approx 10^{-8}$ s).

Within the lifetime of the intermediate state of the nucleus many uncorrelated fluctuations of the EFG occur. Because liquids are isotropic, the randomly fluctuating interaction establishes no preferred direction in space. This means that in equation (2-8) only spherical harmonics of the form $Y_{ki\,0}$ have to taken into account ($N_1 = N_2 = 0$).

Using the addition theorem for spherical harmonics, expressing the final result in terms of Legendre polynomials, the angular correlation function $W(\mathbf{k}_1, \mathbf{k}_2, t)$ becomes:

$$W(\theta,t) = \sum_{k_1 k_2} A_{k_1}(1) A_{k_2}(2) G^{00}_{k_1 k_2}(t) P_{k_2}(\cos\theta) \ . \qquad (2\text{–}64)$$

The selection rule for the 3j-symbols requires for $N_1 = N_2 = 0$ that $m_1 = m_1'$ and $m_2 = m_2'$ in (2–9). So the matrix elements of the time-evolution operator reduce to:

$$< m_1|\Lambda(t)|m_2 >< m_1'|\Lambda(t)|m_2' > \ = \ |< m_1|\Lambda(t)|m_2 >|^2 \ . \qquad (2\text{–}65)$$

The matrix element $|< m_1|\Lambda(t)|m_2 >|^2 \ = \ P_{m_1 m_2}$ describes the probability $P_{m_1 m_2}$ of finding the nucleus in the state $|m_2>$ at time t, if it was in state $|m_1>$ at time t=0. This transition probability $P_{m_1 m_2}$ was calculated for electric quadrupole interactions in liquids by Abragam and Pound[46]:

$$P_{m_1 m_2}(t) = \sum_r (-1)^{-2I-a-b}(2r+1)\begin{pmatrix} I & r & I \\ m_1 & 0 & -m_1 \end{pmatrix}\begin{pmatrix} I & r & I \\ m_2 & 0 & -m_2 \end{pmatrix} e^{-\lambda_r t} \ . \qquad (2\text{–}66)$$

Here λ_r, the relaxation constant, is defined as:

$$\lambda_r = \tfrac{3}{5}\tau_c < \omega_Q{}^2 > r(r+1)[4I(I+1) - r(r+1) - 1] \ . \qquad (2\text{–}67)$$

So for liquids, using (2-66) and (2-67) together with the orthogonality relation of the

3–j symbols, the general angular perturbation function (2-9) reduces to a very simple form:

$$G_{kk}(t) = e^{-\lambda_k t} \quad . \tag{2–68}$$

2.5.2. Rapidly Fluctuating Electric Quadrupole Interaction in Polycrystalline Materials

The problem of finding an analytical expression for the angular perturbation function $G_{kk}(t)$ for solids with time-dependent electric field gradients is rather complicated. Attempts[53,54] to derive analytical descriptions have achieved some success in the past, but due to the complexity of this problem, assumptions and often arbitrary simplifications were made which cast some doubt on the applicability of the results.

Recently, the stochastic theory of PAC spectra due to Blume[55] and Winkler and Gerdau[57] has been used to calculate the angular perturbation function $G_2(t)$ for spin I=5/2 nuclei in the limit of a rapidly fluctuating EFG.[46] The model assumes a static EFG which is symmetric about the z-axis and an additional axially-symmetric EFG whose symmetry axis fluctuates randomly among the x, y, and z directions. It is further assumed that the three states, describing the three directions of the EFG, are equally probable (this is the so-called XYZ+Z model):

$$P_1 = P_2 = P_3 = \frac{1}{3} \quad . \tag{2–69}$$

Then the Hamiltonian, H(t), describing the time-dependent interaction can be written in terms of the Hamiltonians of the three possible states. If K_j is the Hamiltonian of the j^{th} static-EFG state, then the total Hamiltonian is

$$H(t) = \sum_{j=1}^{3} f_j(t) K_j \ . \qquad (2\text{–}70)$$

We used the function $f_j(t)$ to account for the fact that the system is fluctuating. At each time t one of the $f_j(t)$ is one, while the other two are zero. If the probability of a transition from a state m to a state m' is independent of past transitions and only a function of the time interval between two transitions, then the time-evolution operator, $\Lambda(t)$, obeys an equation similar to equation (2-63):

$$\frac{d}{dt}\Lambda(t) = \left(-\frac{i}{\hbar} H_{st}^{x}(t) + R\right)\Lambda(t) \ . \qquad (2\text{–}71)$$

Here we used the time-independent, non-Hermitian "effective Hamiltonian", $\left(-\frac{i}{\hbar} H_{st}^{x} + R\right)$, which is also called the Blume matrix. The so-called Liouville operator H_{st}^{x} is composed of the three static interaction Hamiltonians, K_j, representing the three EFG states, and R is the Liouville relaxation operator, a matrix of transition-probabilities between the three EFG states. Note that this is a phenomenological approach justified by time-dependent perturbation theory, since the system cannot be described rigorously by a Hamiltonian, as it is evident from the fact that the Blume matrix is not hermitian. The time-evolution operator $\Lambda(t)$ then becomes:

$$\Lambda(t) = \exp\left\{\left(-\frac{i}{\hbar}H_{st}^{x}+R\right)t\right\} . \qquad (2\text{–}72)$$

With these assumptions, the matrix elements of $\Lambda(t)$ in the general equation for the angular perturbation function (2-9) have to be replaced by the sum over all the possible matrix elements weighted with the probabilities p_j. Then the angular perturbation function for a polycrystalline source is given by:

$$G_2(t) = \sum_{m_1 m_1' m_2 m_2'} (-1)^{2I+m_1+m_2} \begin{pmatrix} I & I & 2 \\ m_1' & -m1 & N \end{pmatrix}\begin{pmatrix} I & I & 2 \\ m_2' & -m_2 & N \end{pmatrix}$$

$$\times \sum_{a,b=1}^{3} P_a \langle b\, m_2\, m_2' | \exp\left\{\left(-\frac{i}{\hbar}H_{st}^{x}+R\right)t\right\} | a\, m_1\, m_1' \rangle . \qquad (2\text{–}73)$$

The eigenvalues of the Blume matrix are $(-\lambda_q + i\omega_q)$. Each of the complex eigenvalues has its own frequency ω_q and relaxation rate λ_q. The perturbation function can then be written as a sum of terms corresponding to these complex eigenvalues:

$$G_2(t) = \sum_{q} G_2(q) e^{\left(-\lambda_q+i\omega_q\right)t} . \qquad (2\text{–}74)$$

If the fluctuation rate is small, the effect of R is small, and the only frequencies which contribute to $G_2(t)$ with significant weight are the frequencies ω_q, corresponding to the static states among which the system fluctuates. In the limit for very rapid fluctuations, on the other hand, all the static contributions due to H_{st}^{x} average to zero, and $G_2(t)$ is a purely exponential decay, similar to the result for liquids (2-69).

In the rapid fluctuation regime, where the effect of the static frequencies is still noticeable, the numerical result of the angular perturbation function is described by:

$$G_2(t) = S_{20} e^{-\lambda_0 t} + S_{20}' e^{-\lambda_0' t} + \sum_{i=1}^{3} S_{2i} \cos(\omega_i t)\ e^{-\lambda_i t}\ , \qquad (2\text{–}75)$$

where $S_{20} = 0.131$, $S_{20}' = 0.069$, and the other geometrical factors S_{2i} and frequencies ω_i are the same as for the static interaction alone. There are fixed relations between the five relaxation constants, and they can be expressed as:

$$\lambda_0'/\lambda_0 = 3.525\ , \qquad (2\text{–}76a)$$

$$\lambda_1/\lambda_0 = 2.343\ , \qquad (2\text{–}76b)$$

$$\lambda_2/\lambda_0 = 3.071\ , \qquad (2\text{–}76c)$$

$$\lambda_3/\lambda_0 = 5.899\ . \qquad (2\text{–}76d)$$

The same as for static interactions (2.4.3), we have to take small variations of the EFG due to imperfections into account. After convolution with a Gaussian distribution (2-60), the measured angular distribution function for polycrystalline sources with a rapidly fluctuating EFG becomes

$$G_2^{\text{measured}}(t) = S_{20} e^{-\lambda_0 t} + S_{20}' e^{-\lambda_0' t} + \sum_{i=1}^{3} S_{2i} e^{-\lambda_i t} [\cos(\omega_i t)] \exp\left\{ -\frac{\left(\delta\omega_n^0 t\right)^2}{2} \right\}\ . \qquad (2\text{–}77)$$

It is interesting to note that the perturbation function for static interactions,

(2-29), contains a time-independent term, the so-called hard core, which does not decay with time. The perturbation of the angular correlation for static interactions is therefore never completely destroyed. Equation (2-78) shows that the time-dependent perturbation function does not contain such a hard core. This means that for a fluctuating EFG, contrary to the static case, after a time of the order of $1/\lambda_0$ there will be no more perturbation of the angular correlation between the successive gamma-rays.

3. Experimental Arrangements

3.1. PAC Spectrometer

The spectrometer used in this work is a four detector PAC spectrometer which has been developed and improved in our lab over the last three to four years.[38,39,57] Instead of the more conventional multichannel analyzer (MCA), a Tandy/Radio Shack Color Computer (CoCo) was used to control the spectrometer. Although standard features easily available in a MCA must first be programmed when using a computer, such a set up is much more flexible than a traditional MCA-based spectrometer.

The functions of a γ–γ PAC spectrometer are to detect the two correlated cascade gamma–rays emitted by a tracer nucleus and to determine the time separation between them. The functional block diagram of the spectrometer is illustrated in Fig. 3.1. The four gamma–ray detectors are placed at 90° angle intervals in a plane with the source at the center. Each detector is driven by its own high voltage power supply and provides two signals for each absorbed photon: dynode signal (used for energy information), and anode signal (used for timing information). The timing signal is correlated with the time that the gamma–ray enters the detector, and the energy signal is proportional to the energy of the absorbed photon.

3.1.1. Coincidence Electronics

The purpose of the coincidence electronics is to identify events in which a γ–ray with the energy of γ_1 enters one detector and a γ–ray with the energy of γ_2 enters another detector. Such an event is called valid, and the time interval between the

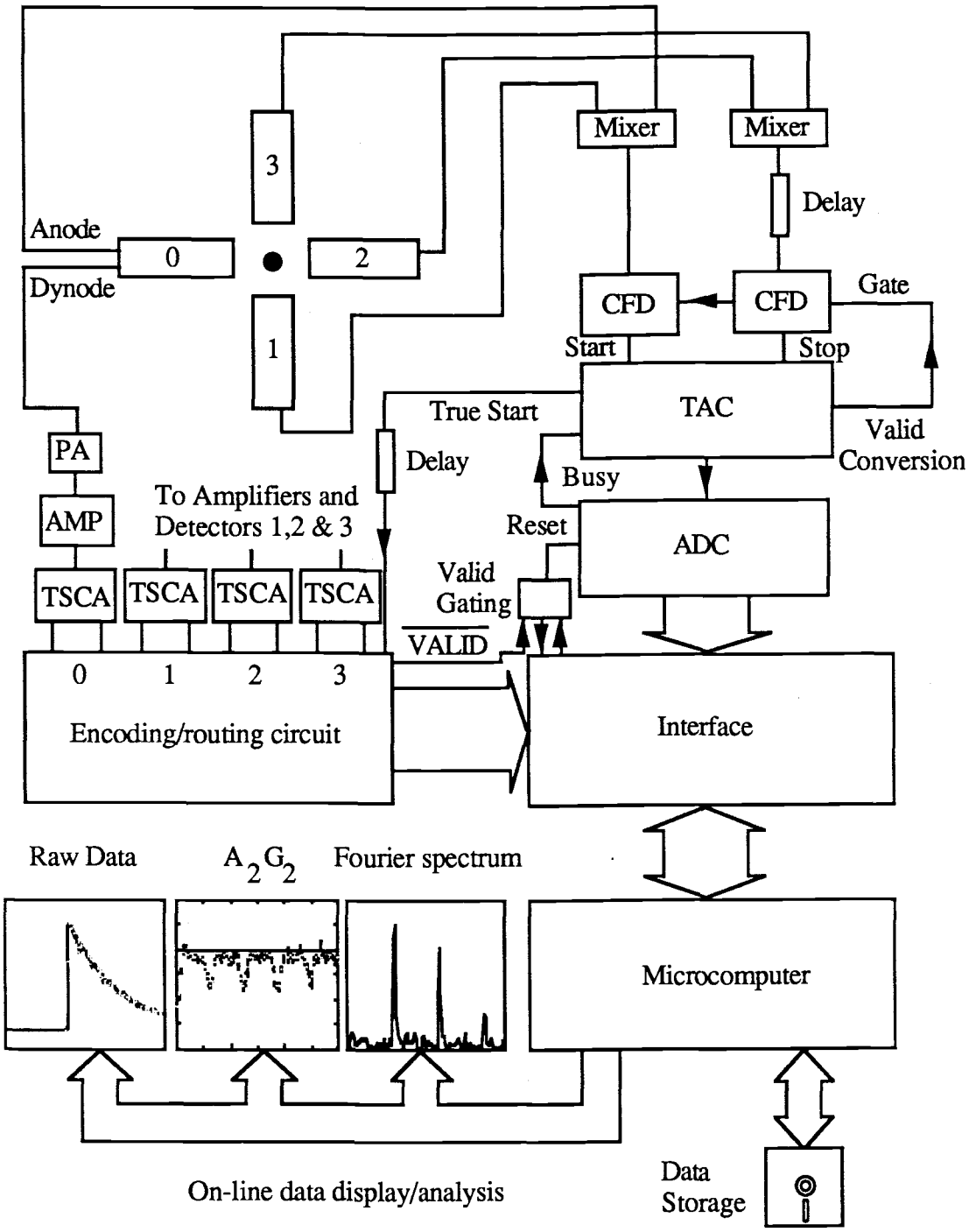

Fig. 3.1. Functional block diagram of the PAC spectrometer.

detection of the two γ–quanta is recorded.

The timing outputs of detector 0 and detector 1 are connected to a signal mixer. The signal is then shaped by a constant–fraction–discriminator (CFD) (EG&G Ortec, Oak Ridge TN, model 583). For every timing signal from the anode of the photomultiplier tube that exceeds the threshold of the CFD, a standard NIM pulse, whose timing is correlated to the time the gamma ray was absorbed in the detector, is generated and then fed into the 'Start' input of a time–to–amplitude-converter (TAC) (EG&G Ortec, model 566).

In the same way, the timing pulses of detector 2 and 3 are connected to a mixer. But before the signals of these two detectors enter the CFD, they are delayed by a delay unit (EG&G Ortec, model 416A), so that a prompt event (γ_1 and γ_2 are detected simultaneously) is recorded near midrange of the TAC. This allows one to accumulate not only a "normal" but also a "reverse" spectrum. The signal then gives the 'Stop' for the TAC.

After the TAC has received a 'Start' and a 'Stop' pulse, the CFDs are gated off until the conversion is completed to avoid interference caused by the incoming CFD signals. For each successful conversion, the TAC will generate a unipolar pulse whose pulse height is proportional to the time interval between the 'Start' and 'Stop' pulses. This pulse then is digitized by an ADC (EG&G Ortec, model 800), which is set to convert a full height linear pulse (10 V) into 1024 channels. As soon as the ADC starts the conversion, a busy signal is generated to gate off the TAC until the ADC is free for the next job. Eventually the ADC is read by the computer through the interface board.

The energy pulses from each detector are shaped and amplified by their own linear amplifiers (EG&G Ortec, model 575A , and Canberra, model 2012), then the resulting bipolar pulses are fed into a laboratory–built twin single–channel analyzer (TSCA). Each TSCA is adjusted to detect both γ_1 and γ_2. The two signals from each

TSCA are fed into a laboratory–built encoding/routing circuit to determine the sequence of the correlated events (the so-called routing information). The "encoding/routing" circuit is designed such that the simultaneous detection of more than one start and/or stop events is considered invalid.

A conversion is accepted as a valid "normal" event only if a TSCA of detector 0 or 1 indicates that a γ_1 was absorbed and a TSCA of detector 2 or 3 indicates that a γ_2 was absorbed. If a γ_2 is detected by detector 0 or 1 and γ_1 is detected by detector 2 or 3 then it is called a valid "reverse" event. In case of invalid events, a valid-gating circuit prevents the ADC-complete signal from interrupting the computer and automatically resets the system, reducing the dead-time of the spectrometer.

As soon as a valid event is flagged, the computer is interrupted and the digitized time separation of the two cascade gamma–rays and their routing information is collected by the interrupt service routine of the operating software and stored in the proper location of the computer memory. While the computer is waiting for the interrupts, it can perform some simple tasks. For example, the raw data may be displayed on an oscilloscope and on-line analyses can take place while the experiment is in progress. With this configuration, it is very easy to monitor the progress of the experiment and to detect the faults in the spectrometer or sample in the early stage and take proper measures to correct them accordingly. During an experimental run, the data are saved several times to prevent the loss of data due to power failure or computer crash.

3.1.2. Operating Software

A Tandy/Radio Shack Color Computer (CoCo) is used in this experiment to control the spectrometer and store the results on a disk. The coincidence electronics as

described above is connected to the CoCo via a bus expansion box (Basic Technology, Ortonville, MI, model BT 1000) using a peripheral interface adapter (PIA) chip (Synertek, Santa Clara, CA, type SY 6522).

Most of the spectrometer software is written in BASIC, but the time–critical parts are written in machine language. The most time–critical part is the interrupt service routine, because the time spent in reading the PIA ports largely determines the dead–time of the system. The interrupt service routine saves the processor register, status and return address on the stack. After the PIA registers are read, the ADC is reset and the next interrupts can occur while the computer is still processing the previous one. This sets an upper limit on the rate at which interrupts can be accepted. If the interrupt rate becomes too high, the stack overflows and the computer crashes. In practice, this has not been a problem because the activity of the samples was low enough not to cause too many interruptions. For additional safety, an interrupt service routine examines the VALID bit (most significant bit of the routing information) and returns immediately from interrupt if the event is invalid.

In the case of a valid interrupt, a memory location is determined by the data received from the PIA input lines. The computer's random access memory (RAM) is divided into 16 sectors corresponding to the pairs of detectors that detected γ_1 and γ_2. For example, sector 0/2 holds the spectrum of events for which γ_1 is detected in detector 0 and γ_2 in detector 2, etc. Of the possible 16 sectors, only 8 sectors are actually used. These are sectors 0/2, 0/3, 1/2, and 1/3 for the "normal" spectrum, and sectors 2/0, 2/1, 3/0, and 3/1 for the "reverse" spectrum. Each sector consists of 512 channels and each channel is represented by two bytes. The routing information identifies the memory sector, while the ADC conversion result designates the offset of a particular event in that sector. As soon as the channel which corresponds to the detected

events is identified, the count in that channel is increased by one and the routine returns from interrupt. The channel representing time–zero (of a prompt event) is located near mid–range of the TAC (channel 256), so that in addition to the "normal" spectra the "reverse" spectra can be accumulated.

For a typical run, about 5×10^4 to 6×10^4 counts per channel at the peak of the spectrum are accumulated, so a total of $\sim10^7$ counts are accumulated for each sector. A typical run takes about 24 to 48 hours to accumulate two statistically independent spectra ("normal" and "reverse"). When sufficient data have been collected, the spectra and relevant information such as sample name, date, temperature and calibration data are saved to a floppy disk for later analysis on an Apple Macintosh II computer.

3.1.3. Spectrometer Calibration

At regular intervals, the energy and time calibration of the spectrometer had to be checked and adjusted when necessary.

Performing the energy calibration means adjusting the TSCA's in such a way that they cut out the desired energies of γ_1 and γ_2 of the total spectrum of the ^{181}Ta . The energy calibration is done with the sample which is currently being investigated and a multichannel analyzer (MCA) connected to the output of the linear amplifier. Fig. 3.2. shows a typical energy spectrum accumulated in the MCA. For a zirconia sample containing ^{181}Hf/^{181}Ta tracer, four prominent peaks can be recognized. The large low energy peak is mainly due to 133 keV photons from the 1/2 -> 5/2 decay (see Fig. 1.2. and Fig. 3.2.), but note that the 136 keV peak from the 9/2 to ground state decay is not resolved from the one at 133 keV. The two smaller high energy peaks result from the 346 keV decay of the intermediate state to the 9/2 state and the 482 keV gamma from the

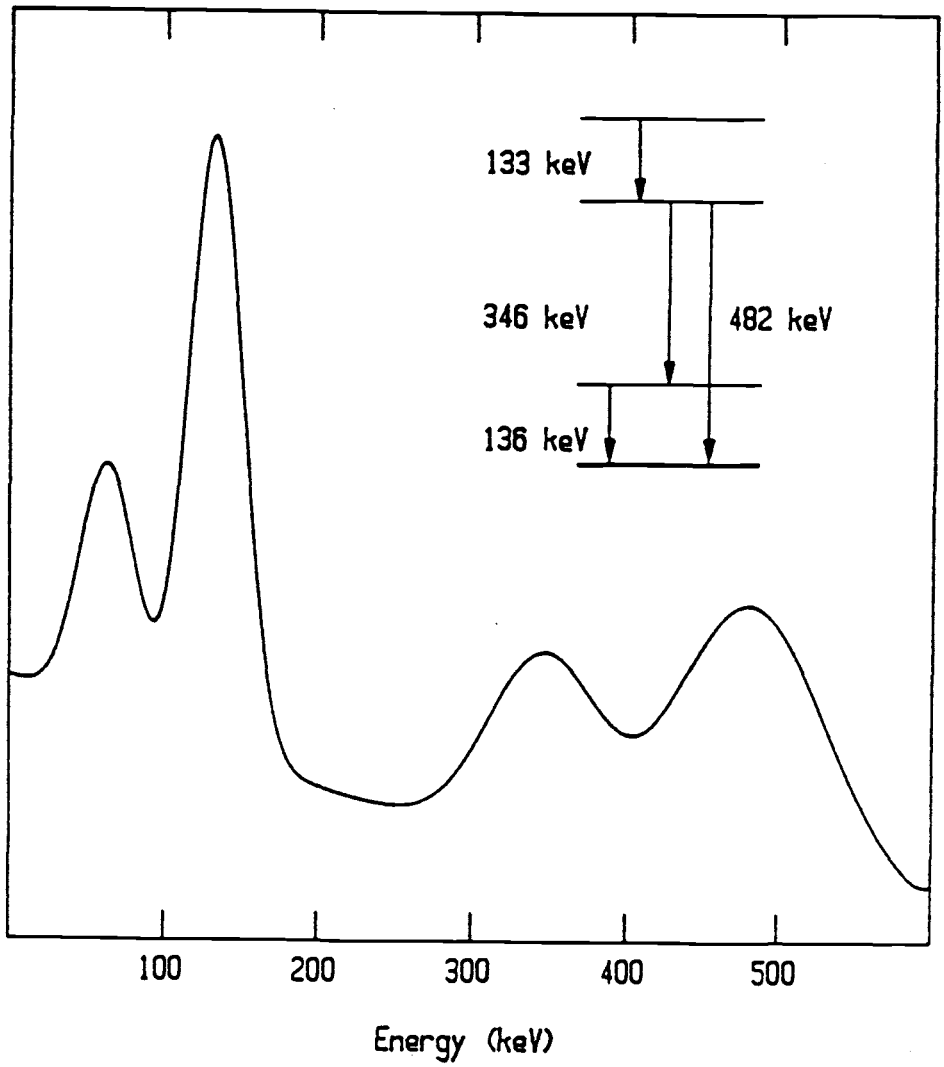

Fig. 3.2. Typical energy spectrum of ^{181}Ta recorded by a MCA unit using a BaF_2 scintillator detector. The PAC transitions γ_1 and γ_2 are the 133 keV and the 482 keV peaks, respectively.

intermediate to ground state transition, respectively. The low-energy peak near 70 keV is probably the result of K x-rays from ^{181}Ta. With the MCA gated by the output signal of the TSCA, the windows of the TSCA are set so that only the 133 keV (γ_1) or 482 keV (γ_2) peak is detected.

The energy spectrum of the zirconia-alloy samples in this experiment (Fig. 3.2.) is not only a result of the ^{181}Hf/^{181}Ta decay. In fact, the relative intensity of the peaks turned out to be dependent on the time since the irradiation with neutrons, which indicated that other isotopes with different half-lives contributed to the spectrum. The intensity of the 346 keV peak relative to the "Stop"-peak (482 keV) increased from 85% for a strong sample (immediately after irradiation) to about 100% after two to three half-lifes. In strong samples a high energy peak at about 740 keV showed an intensity relative to the "Stop"-peak of 11%, whereas this percentage rose to 34% for weak samples. These increases could be caused by ^{95}Zr decaying to ^{95}Nb with a half life of 64 days (724 keV and 756 keV) and ^{175}Hf which decays to ^{175}Lu (343 keV) with a half-life of 70 days.[43] It is not unlikely that these isotopes occur naturally in the materials used for the samples and their contribution becomes more and more important with age of the samples since their half-lives are longer than ^{181}Hf (42.4 days).

The task of time calibration consists of three parts: (i) adjusting the cable lengths in the fast branch so that the time–zero channels for all memory sectors are the same, (ii) determining the time scale of the TAC, and (iii) determining the time resolution of the spectrometer. Before the time calibration can be performed, the energy windows of the TSCA must be adjusted very carefully to respond to the appropriate energy peaks of the PAC nuclide being used in the experiment.

The time–zero channel for a prompt event in each memory is aligned using a ^{22}Na source, which decays with a half–life of 2.6 years through β^+ emission to its daughter isotope ^{22}Ne. The positron eventually annihilates with a electron in the

surrounding material. In most of the cases, two photons, each with energy of 511 keV, are created simultaneously and emitted in opposite directions. Occasionally, the photon pair will be absorbed by two detectors, and the resulting prompt spectrum accumulated in the corresponding memory sector should ideally resemble a delta–function. In reality, the prompt peaks have a Gaussian–like distribution due to the finite time resolution of the spectrometer. By adjusting variable delay lines between the mixers and CFDs, the time–zero channels of all memory sectors are aligned to within a few tenths of a channel width.

After prompt spectra for each detector pair have been accumulated for the same time interval, a program determines location and full width at half maximum (FWHM) for every prompt peak and computes the instrumental resolution function for both the normal and reverse spectrum. The instrumental resolution function, used during data analysis to account for the finite time resolution of the spectrometer, is the sum of the prompt peaks in each of the four channels before and after the time–zero channel and is normalized to 255 in the time–zero channel itself.

Special care needs to be taken to ensure that the prompt peak counts for each detector pair are as close as possible in order to get a statistically equal weighted contribution from each pair. The FWHM of the resolution function is as wide as the prompt peak belonging to the worst detector pair, assuming that the prompt peaks are lined up perfectly. The FWHM in this work is about two channels. Because the resolution is 0.4 ns/channel, the overall time resolution of the spectrometer is ~0.8 ns.

A time calibrator (EG & G Ortec model 462) is used to determine the absolute time scale of the TAC. The time calibrator generates 'Start' and 'Stop' pulses separated by integer multiples of a chosen constant period. These peaks are fed directly into the TAC inputs, and a calibration program accumulates the periodic repeating peaks and evaluates the time calibration by doing a least square fit. The time calibration gives the

absolute time scale for the TAC. For the data collected in this work the time calibration was 0.42 ns/channel with an error of less than 0.4%. Time–zero channel, instrumental time resolution function and time calibration are stored in the computer's RAM and saved with experimental spectra to a floppy disk so that this information is available when the spectra are analyzed.

3.1.4. Gamma–Ray Detectors

Each gamma–ray detector consists of a 1.5" × 1.5" cylindrical barium fluoride (BaF_2) scintillator (Harshaw/Filtrol Partnership, Solon, OH) mounted on a Hamamatsu photomultiplier (Hamamatsu, H 3177 , Japan). The base and the tube are mounted together as one unit, and the detector is already covered by the manufacturer with magnetic shielding to prevent the external magnetic field from penetrating the detector. High voltage power for each detector is provided by two power supply units (Fluke, Seattle, WA) and a laboratory-built voltage splitter, which allows individual setting of the voltages for all four detectors.

Due to the interaction of a photon entering the scintillator with the material, the energy of the γ-ray is converted to fluorescent light in the scintillator crystal. The intensity of the resulting fluorescent light is proportional to the energy the photon absorbed in the scintillator. The fluorescent light then enters the window of the photomultiplier and hits the cathode, coated with photoelectric material, and frees electrons which are then accelerated and multiplied along the dynode chain.

In using γ-γ TDPAC techniques to probe microscopic properties of condensed matter, a set of scintillators with both good energy and timing resolution is essential. NaI(Tl) scintillators used in most TDPAC experiments have a high efficiency and good

energy resolution but their time resolution (mostly in 2 to 3 ns range) is poorer than of BaF_2 crystals. Because the half-life of the intermediate state in our PAC probe nuclei is only 10.8 ns, a good time resolution of the spectrometer has to be achieved and therefore BaF_2 crystals have been used in this research. The fluorescent spectrum of BaF_2 shows a fast component in the ultra violet at 220 nm and a slow component at 310 nm. The fast component carries about 20% of the total light intensity and has a decay time of 0.8 ns. In comparison, NaI scintillators show a decay time of 230 ns at 413 nm. Some selected properties of the BaF_2 scintillator are listed in Table 3.1.

Table 3.1. Some selected data of BaF_2 scintillator.[60]

Light yield relative to NaI(Tl):		
	fast component	50%
	slow component	20%
Wavelength of maximum emission:		
	fast component	220 nm
	slow component	310 nm
Decay constant:		
	fast component	0.8 ns
	slow component	620 ns
Index of refraction at 325 nm		1.49
Thermal coefficient of linear expansion		18.4×10^{-6}/K
Density		4.88 g/cm^3
Melting Temperature		1627 K
Hygroscopic		no

Due to the memory limitations of the CoCo in use at this moment and the transit time spread in the photomultiplier tubes, we are unable to fully utilize the good timing resolution of the BaF_2 crystal. The timing resolution of the spectrometer in this work is about 0.8 ns, which is still very good. Since the fast component of the fluorescent light from the BaF_2 is in the ultraviolet region, a photomultiplier with a quartz window like the Hamamtsu H-3177 must be used.

The density of BaF_2 is 4.88 g/cm^3, compared to 3.67 g/cm^3 for NaI. This results in a higher absorption efficiency for γ–quanta in BaF_2 . The energy resolution of a detector is defined as $R = \Delta E/E$, where ΔE is the full width at half maximum and E the mean energy of the peak. While E is proportional to the number of electrons created at the cathode, ΔE is proportional to the standard deviation of the number of photoelectrons. Since NaI detectors yield about 50% more photoelectrons than BaF_2, the energy resolution for BaF_2 is about a factor of $\sqrt{2}$ worse than for NaI scintillators. An energy resolution of 15% for 511 keV gamma–rays can be achieved with our spectrometer which is comparable to the published results.[58,59] .

A detailed study of the properties and characteristics of BaF_2 scintillator has been reported in the literature[61], and the applications of the BaF_2 in the γ–γ TDPAC measurement of condensed matter have been reported by several groups.[36,58]

The face and the sides of the scintillator were covered with 3 layers of proprietary ultra–violet light reflecting Teflon tape (Harshaw/Fitrol) and a layer of aluminum foil to increase the light output. The crystal was mounted on the photomultiplier window using General Electric Viscasil 600-000 silicone fluid as optical coupling fluid, which exhibits a near unity transmissivity for light with wavelength greater than 190 nm. All four detectors are attached to aluminum frames and are free to slide along tracks at 90° angles from each other.

3.1.5. Furnace

Furnace development has been a major effort in this laboratory over the past several years.[39] Because measurements were taken in a temperature range between room temperature and 1300°C, the furnace must satisfy several conditions in order to allow proper work. Some of these conditions are: (i) the outer surfaces of the furnace must be at room temperature so that detectors work at the same temperature independent of the sample temperature, (ii) the furnace body should be thin and constructed using a material of low atomic number so as not to reduce the intensity of the gamma–rays emitted by the sample significantly, and (iii) the furnace must work reliably at 1300°C or even higher continuously over several weeks.

The furnace, which is used in this work, is built around a one-end-closed alumina furnace tube (McDanel Refractory Co, Beaver Falls, PA, type 998) with an inner diameter of 3/8" and an outside diameter of 1/2". The heating element is cut from a 5/1000" thickness graphite foil with the help of a predrawn paper pattern (Fig. 3.3(a)).

The heating element is wrapped around the furnace tube and covered with one layer of alumina thermal insulation and two layers of zirconium foil. The insulation material has been heated to about 1200 °C for 48 hours in order to burn off organic binder contained in the material. This binder would otherwise carbonize at elevated temperatures during the run of the experiment and begin conducting, ruining the effect of the heating element. The zirconium foil serves two purposes: heat shielding and oxygen "gettering" to prevent the heating element from oxidizing. Two pieces of copper foil are used as the current leads which are connected to the vacuum feed–through.

The heating unit is mounted in an aluminum housing surrounded by a water–cooled jacket (Fig. 3.3(b)). A laboratory–built AC power supply is used to power the furnace. The open end of the furnace tube is exposed to the air, and the sample and a

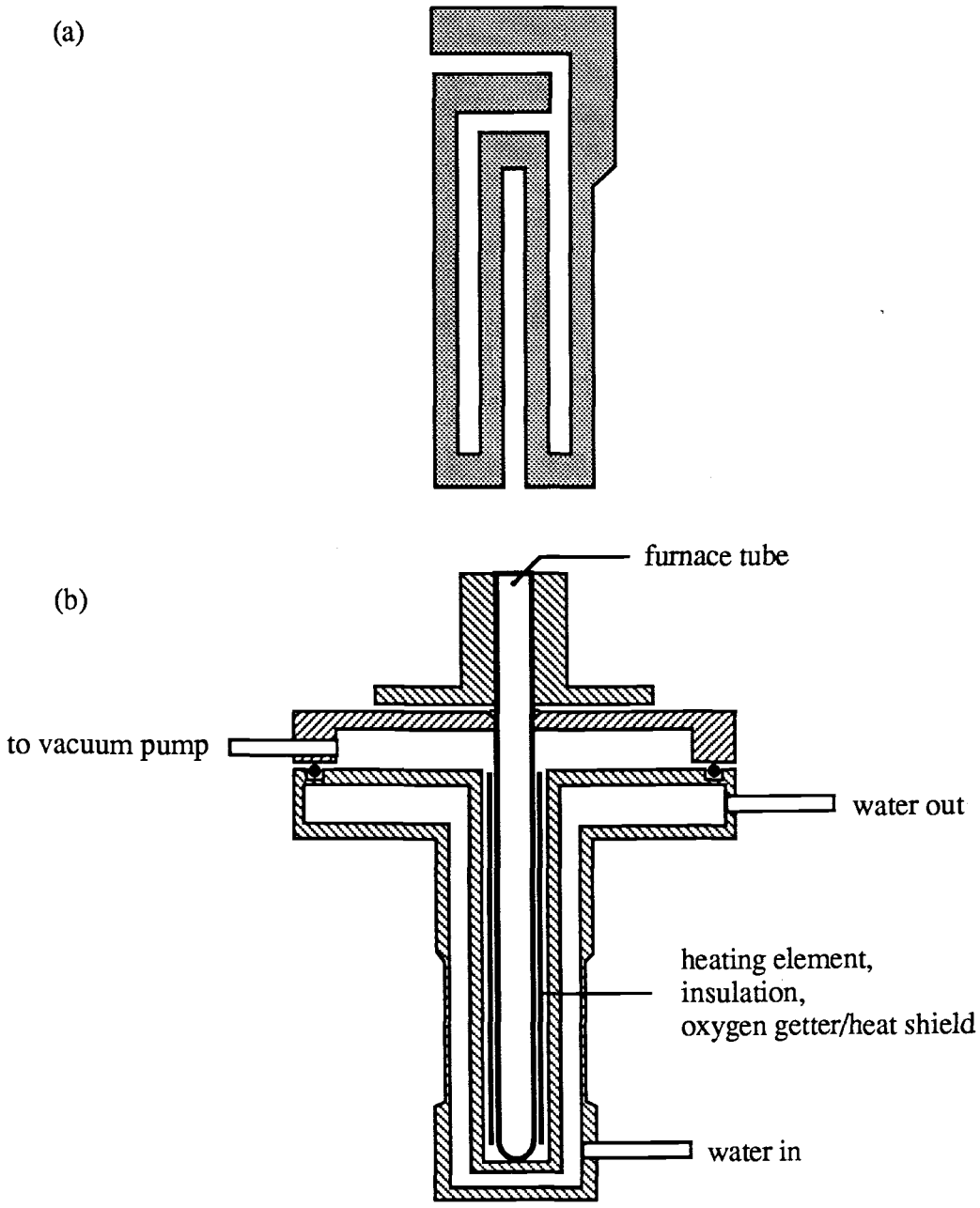

Fig. 3.3. (a) The graphite foil heating element. The resistance of the graphite heating elements is ~8Ω.
(b) Sectional view of the PAC furnace.

Pt–Pt/10%Rh thermo couple is placed in the center of the tube. The temperature is controlled by a proportional controller (Omega Engineering, Stamford CT, model 49) connected to the thermocouple. It was found that a moderate vacuum (ca. 15 mTorr) is sufficient to prevent the heating element from oxidizing. A well–constructed furnace will typically last for 3–6 months, operating at temperatures up to 1300°C.

Temperature profiles of the furnace have been measured over various temperatures up to 1400°C[38]. The temperature differences between all sides of a sample are slightly less than 10°C at 1400°C. The mentioned temperature controller has an analog temperature display to show the local temperature at the position of the sample. This display was calibrated using a Pt–Pt/10%Rh thermocouple and an accurate voltmeter. Fig. 3.4. shows a linear relationship between displayed and actual temperature, but a correction factor has to be taken into account. Even though the temperature cycle of the temperature controller is smaller than 3°C, the temperature uncertainty should be considered to be about 10°C at 1300°C.

3.2. Sample Preparation

Three different zirconia-yttria alloy samples were used in this work with Y_2O_3 contents of 35.4 wt % , 27.8 wt %, and 16.9 wt %, respectively. As mentioned in 1.1.2., the cubic phase is stabilized in alloys with an Y_2O_3 content above 16 wt %, so all samples used in this experiment are cubic, fully yttria stabilized. All sample materials were obtained from Teledyne Wah Cheng, Albany, Oregon and contained roughly 1 at % hafnium. Of each of the three materials, samples of 100 mg and 200 mg were made and placed in cylindrical alumina capsules of 4 mm inner diameter and a height of 25 mm. For use in the spectrometer, the samples had to be irradiated with thermal neutrons in

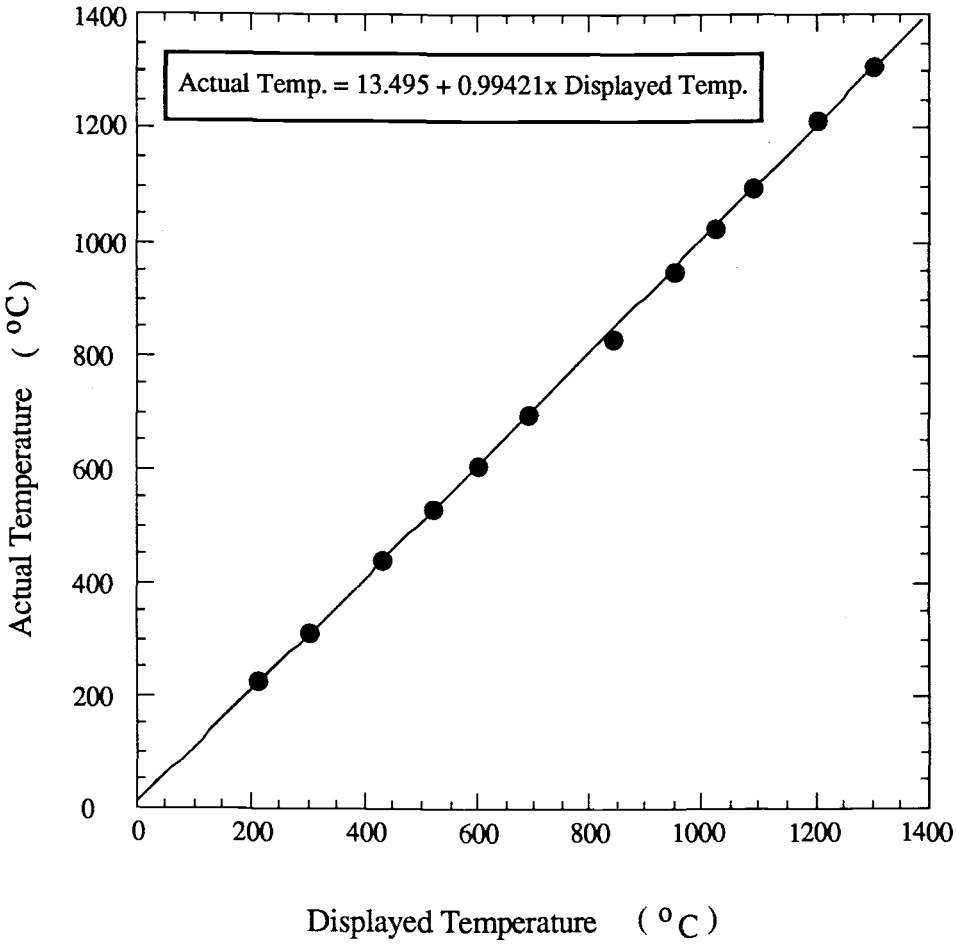

Fig. 3.4. Calibration of the display of the temperature controller. The line is a linear fit to the data.

order to create the radioactive isotope ^{181}Hf out of the natural ^{180}Hf. This was done at the Oregon State University Triga reactor, which had a thermal neutron flux of $4x10^{12}$ $n/(cm^2\ s)$ at 1 MW. For additional safety, the alumina containers were sealed in a nuclear grade polyethylene vial during irradiation.

In addition to ^{181}Hf, a number of short-lived isotopes were produced also. The samples were allowed to rest for at least three days for these isotopes to decay. The remaining ^{181}Hf activity, typically 15 to 25 μCi, was adequate to permit PAC measurements with good statistics to be taken within one to two days. Because of the long half-life of ^{181}Hf, a sample retains sufficient activity to be used for about 40 to 60 days.

4. Data Reduction and Data Analysis

After sufficient data have been collected for a spectrometer run, the coincident counts of each of the sectors for the "normal" and "reverse" spectra are saved to a floppy disk by the CoCo. Information about the calibration of the spectrometer (see 3.1.3.) is saved together with the spectra. The analysis of these raw data is basically done in two steps:

- **Calculating of $A_2G_2(t)$ (Data Reduction).** The raw data are read into an IBM XT computer where the experimental perturbation function $G_2(t)$ multiplied by the effective anisotropy A_2 is calculated using a laboratory-built program.
- **Fitting the experimental $A_2G_2(t)$ to different fitting models (Data Analysis).** The $A_2G_2(t)$, calculated from the data, is transferred to an Apple Macintosh II computer where a laboratory-built program is used to fit the results to different fitting models. The resulting fitting parameters are used for further analyses.

4.1. Data Reduction

The spectrum of each sector as it is saved on a CoCo-disk and read by the IBM XT is the number of counts per channel. Given the time calibration (in this experiment 0.4 ns/channel), this can be interpreted as a time dependent spectrum. Each sector i/j contains also a certain amount of background counts (B_{ij}) due to accidental coincidences. The background for the "normal" spectrum is found by taking the average of counts in channels corresponding to events which occurred 35 to 80 ns before time-zero. Because these channels accumulate events at negative times, they just

contain random background. For the "reverse" spectrum, the background is taken from channels corresponding to positive times.

If θ is the angular separation between the i^{th} and j^{th} detector, and e_i, e_j, the efficiencies of each detector, then the raw data contained in its corresponding memory sector i/j can be expressed as:

$$D_{ij}(\theta,t) = \frac{1}{\tau_N} e^{-\frac{t}{\tau_N}} e_i e_j N_0 W(\theta,t) + B_{ij} \ . \qquad (4\text{–}1)$$

Here N_0 is the decay rate of the parent isotope (in this experiment ^{181}Hf) and τ_N is the mean life of the intermediate state ($5/2^+$ state of the ^{181}Ta, τ_N=10.8ns). $W(\theta,t)$ is the angular correlation function which contains all the information about the interaction of the probe and the environment as it is discussed in chapter 2. For PAC experiments in polycrystalline materials using a probe with a 5/2 intermediate state and neglecting higher order terms, we derived the angular correlation function (2-70):

$$W(\theta,t) \approx 1 + A_2 G_2(t) P_2(\cos\theta) \ . \qquad (4\text{-}2)$$

The first step in the data reduction is to subtract the background counts (B_{ij}) from the data (D_{ij}) in each sector. The average background per channel is subtracted, beginning at time-zero channel until the signal-to-noise ratio becomes smaller than one. At that channel, the spectrum is cut and the succeeding channels are not considered in further analysis. The background-corrected counting rate is

$$C_{ij}(\theta,t) = D_{ij} - B_{ij} = \frac{1}{\tau_N} e^{-\frac{t}{\tau_N}} e_i e_j N_0 W(\theta,t) \ . \qquad (4\text{–}3)$$

Under the assumption that the efficiencies e_i and e_j are the same for each detector, the experimental angular perturbation function $A_2G_2(t)$ is equal to the so-called spectra-ratio, R(t), which is defined for the "normal" spectrum as[62]

$$R_n(t) = 2\frac{(C_{02}\,C_{13})^{1/2} - (C_{03}\,C_{12})^{1/2}}{(C_{02}\,C_{13})^{1/2} + 2(C_{03}\,C_{12})^{1/2}} = A_2G_2(t)_{normal} \qquad (4\text{–}4)$$

and for the "reverse" spectrum as

$$R_r(t) = 2\frac{(C_{20}\,C_{31})^{1/2} - (C_{30}\,C_{21})^{1/2}}{(C_{20}\,C_{31})^{1/2} + 2(C_{30}\,C_{21})^{1/2}} = A_2G_2(t)_{reverse}\,. \qquad (4\text{–}5)$$

So the experimental $A_2G_2(t)$ function for both the "normal" and the "reverse" spectrum was calculated and saved to their corresponding files.

4.2. Data Analysis

The experimental angular perturbation function $A_2G_2(t)$, calculated by an IBM XT computer, was transferred to an Apple Macintosh II computer. Laboratory-built programs were used to fit $A_2G_2(t)$ to different models and to take the Fourier transform of both $A_2G_2(t)$ and the fitted functions.

4.2.1. Fourier Transformation

A Fast Fourier Transformation (FFT) of the angular perturbation function $A_2G_2(t)$ was performed for some of the samples as additional information about sample quality (homogeneity) and phase transformations in the samples.

For a FFT of the $A_2G_2(t)$, the time–domain data were multiplied by a time–domain window to reduce the spurious peaks in the Fourier spectrum due to the finite extension of the data. The windowed time data were reflected to negative time to increase the data range. A cosine window was used in finding the FFT s for the $A_2G_2(t)$ functions throughout this work.

To ensure accurate fits, the FFT of the experimental $A_2G_2(t)$ and the FFT of the fitted function were compared.

4.2.2. Fitted and Derived PAC Parameters

A nonlinear least–squares fitting routine [63] based on Marquardt's algorithm was used to fit the experimental $A_2G_2(t)$ function to an appropriate theoretical expression. To account for the finite instrumental resolution of the spectrometer, the time resolution function of the system is worked into the fitting routine. The distribution of the EFG is assumed to be of Gaussian shape (see 2.4.1.). For a converging and meaningful fit, a hard copy of the fitted parameters and a plot of the fitted function was obtained.

The fitting parameters could be chosen to be either fixed to a certain value during the fit, or to be adjusted by the fitting routine. These parameters are:

- **The observed effective anisotropy** (A_2^{eff}). The true A_2 is reduced by solid angle correction factor and by other known or unknown sources and is called A_2^{eff}.

- **The relaxation constants (λ_k).** Time dependent fluctuations of the EFG give rise to terms like $e^{-\lambda_k t}$ in the perturbation function $G_2(t)$ (see 2.5.).
- **PAC frequencies (ω_1, ω_2).** The PAC frequencies depend on the quadrupole frequency ω_Q and the asymmetry η of the EFG (2-57, 2-68). The frequencies ω_1, ω_2 are therefore a measure of the interaction between the nuclear quadrupole moment of the nucleus and the EFG due to the environment.
- **The relative distribution (δ) of the EFG.** $\delta = \frac{\Delta\omega}{\omega}$ is also called the line width and is related to the distribution of cations and oxygen vacancies.

Other physical quantities can be derived from these fitting parameters. Of interest for this work is especially (i) the quadrupole frequency ω_Q, (ii) the magnitude of the electric field gradient V_{zz}, and (iii) the energy barrier for motion of defects E_a.

(i) The quadrupole frequency ω_Q can be directly obtained from the PAC frequencies ω_1 and ω_2 using equation (2-58):

$$\omega_{1,2} \;\alpha\; \omega_Q \,. \qquad (4\text{-}6)$$

(ii) V_{zz}, the magnitude of the electric field gradient, is proportional to ω_Q. We recall: $\omega_Q = \frac{e\,Q\,V_{zz}}{4I(2I-1)\hbar}$ (2–46). Since the quadrupole moment Q of the intermediate state is known to be 2.5 barn, equation (4-6) together with (2-46) show that V_{zz} is proportional to the PAC frequencies. The fitted parameters ω_1 and ω_2 are therefore a direct measure of the magnitude of the electric field gradient at a probe site.

It must be noted that the EFG, with which the quadrupole moment of the intermediate state of the PAC probe interacts, is not only due to ion cores of nearby

atoms. In general, electronic contributions arising from the influence of covalent bonds, conduction electrons, filled and unfilled electronic shells of the probe atom are also to be taken into account.[64]

In this experiment, covalent bonds are not expected to contribute considerably to the EFG. Charge density plots indicate that the oxygen charge distribution is mostly directed towards the zirconium atoms,[65] so the influence of the covalent bonds is to change the effective charge of the oxygen atoms. But these changes are not dominant.

Because ZrO_2 is an insulator, there are no contributions due to conduction electrons.

The closed electron shells of the probe atoms are usually distorted from spherical symmetry by nearby charges, causing an additional field gradient at the nucleus. This indirect contribution of the electron shells to the field gradient can be one to two orders of magnitude larger than the EFG due to the surrounding charges. To account for this additional contribution due to polarization of the core electron shells, the EFG -as it is "seen" by the PAC probe- is usually parameterized as[64]

$$V_{zz} = (1-\gamma_\infty)V_{zz}^{ion} , \qquad (4\text{–}7)$$

where γ_∞ is the Sternheimer anti-shielding factor and V_{zz}^{ion} the EFG due to neighboring ion cores. γ_∞ is negative for most ion cores. Extensive tables of anti-shielding factors for ions with closed shells, calculated using a relativistic Hartree–Fock–Slater electron theory, can be found in the literature.[66] However, γ_∞ for the Ta^{5+} ion could not be found in the literature, and so the value $\gamma_\infty = -61$ was chosen by interpolating between the numbers quoted for Hf^{4+} and W^{6+}.[66]

(iii) The energy barrier for motion of defects E_a can be derived using the temperature dependence of the relaxation constant λ. For high temperatures (above

about 850° C) the relaxation constant λ is proportional to $e^{+E_a/kT}$ (see 5.4.1.). In a plot of $\ln(\lambda)$ versus 1/T, the slope of the resulting curve is proportional to the energy barrier E_a.

5. Results of PAC Measurements

5.1. The Fitting Procedure

As described in 4.2., the experimental angular perturbation function (G_2) multiplied by the anisotropy (A_2) was obtained from the data accumulated during a run of the spectrometer. The result of $A_2G_2(t)$ was fitted to analytical expressions containing adjustable parameters.

The data for high temperatures (T > 700°C) were fitted to a dynamic quadrupole relaxation term (2-78), which was obtained by a stochastic model valid for rapidly fluctuating EFGs:

$$A_2G_2(t) = A_2\left\{S_{20}e^{-\lambda_0 t} + S_{20}'e^{-\lambda_0' t} + \sum_{i=1}^{3} S_{2i}e^{-\lambda_i t}[\cos(\omega_i t)]\exp\left[-\frac{\left(\delta\omega_n^0 t\right)^2}{2}\right]\right\}. \qquad (5\text{–}1)$$

The relaxation constants λ_i can be expressed in terms of λ_0:

$$\lambda_0' = 3.525\ \lambda_0, \qquad (5\text{–}2a)$$

$$\lambda_1 = 2.343\ \lambda_0, \qquad (5\text{–}2b)$$

$$\lambda_2 = 3.071\ \lambda_0, \qquad (5\text{–}2c)$$

$$\lambda_3 = 5.899\ \lambda_0. \qquad (5\text{–}2d)$$

A Gaussian EFG-distribution accounted for random variations of the EFG due to defects and impurities.

The low-temperature data (T < 700°C) were fitted to the expression,

$$A_2G_2(t) = A_2 e^{-\lambda t}\left\{ S_{20} + \sum_{i=1}^{3} S_{2i}[\cos(\omega_i t)]\exp\left[-\frac{\left(\delta\omega_n^0 t\right)^2}{2} \right] \right\} . \qquad (5\text{–}3)$$

This expression has been used for PAC spectra in viscous liquids due to slowly varying interactions.[67] Although this equation is not precisely applicable in cubic zirconia, it was used because there is presently no other valid analytical expression available for powder samples with slowly fluctuating EFGs. Equation (5-3) can be considered to be the perturbation function for a static interaction in a powder sample (2-63) multiplied by an exponential damping term accounting for the slow motion of oxygen vacancies. The decay-constant λ is the inverse of the fluctuating EFG correlation time.

5.2. The Effective Anisotropy, A_2^{eff}, of ^{181}Ta

The experimentally measured anisotropy A_2 of the gamma–rays cascade for the PAC probe (^{181}Ta) does not agree with the value given in literature (Table 1.1.).

Ideally, A_2 depends only on the spins of the nuclear levels and multipolarities of the radiations involved in the processes and is therefore independent of the environment of the probe atom. However, in a real experiment many sources influence A_2. Because it is impossible to account for all the factors which might result in the A_2-variation, it is more practical to determine an "effective anisotropy" for the PAC spectrometer.

The effective anisotropy, A_2^{eff}, the value of $A_2G_2(t)$ at time t = 0 because $G_2(t = 0) = 1$ (2-9), was used as one of the fitting parameters when the results of $A_2G_2(t)$ were fitted to analytical expressions (see 4.2. and 5.1).

Besides unknown factors, A_2^{eff} includes phenomena which are known to cause the anisotropy A_2 to deviate from its true value. These phenomena include:

• **Finite size of both detectors and samples.** To obtain equation (4-4, 4-5), we assumed the angles θ appearing in the Legendre-polynomials of the angular correlation function (2-31) to be exactly 90° and 180°. If the finite sizes of the sample and the detectors are taken into account, θ has to be replaced with an average of all the angles within a range of $\theta-\Delta\theta < \theta < \theta+\Delta\theta$. The spectra-ratio R(t) from equation (2-4, 5) then becomes

$$R(t) \approx A_2^{eff}\, G_2(t), \tag{5-4}$$

and in first order the effective anisotropy is given by

$$A_2^{eff} = A_2 \frac{2}{3}\left\{<\cos^2(180^o)>-<\cos^2(90^o)>\right\}. \tag{5-5}$$

An empirical formula, assuming a point sample but finite size detectors, has been proposed by Collins:[68]

$$A_2^{eff} = A_2 \left\{1-1.1\sin^2(\alpha)\right\}, \tag{5-6}$$

where $\alpha = \tan^{-1}(r/d)$ with r being the radius of the scintillator and d the sample–detector separation. The influence of the finite size of the sample and the detectors reduces A_2.

• **Compton scattering.** Gamma-rays scattered through small angles without losing significant energy can enter the detectors. Because the energy-shift is small, they still pass the windows of the TSCAs, but due to the reflection, the gamma-rays can enter the

scintillation crystal with large angles. Therefore, Compton scattering reduces A_2 in the same way that finite size attenuation does.

• **Sample self-absorption.**[69] This phenomenon occurs most often in high-Z samples. The absorption of gamma-rays depends on the distance the gamma-ray travels in the sample and results in an increase of A_2.

To obtain a result of A_2^{eff} for the ^{181}Ta probe without the influence of surrounding Y or Zr atoms, PAC spectra of a "pure" Hf wire were collected. Since it was not possible to purchase a sample with 100% Hf, a wire with 2.86 wt% Zr (Teledyne Wah Chang, Albany, Oregon) was used. The weight of the Hf-sample, 1 mg, was equal to the Hf content in the zirconia samples (typical weight: 100 mg. Hf content: about 2 wt %). The wire was irradiated with thermal neutrons to obtain the radioactive isotope ^{181}Hf in the same way as the zirconia-alloy samples. Of special interest was the question of how A_2^{eff} is influenced by the fact that the γ-rays have to penetrate the furnace. For that purpose, spectra were obtained with the wire being placed both in the furnace and outside. To investigate the effect of varying sample-detector distances, PAC spectra were collected for distances between 3.8 cm and 6.5 cm in steps of 0.5 cm. Fig. 5.1. shows a typical PAC spectrum calculated from the data in our spectrometer and Fig. 5.2. gives the results of the fitting parameter A_2^{eff}.

Two aspects of the result are rather surprising. First, the effective anisotropies, A_2^{eff}, differ considerably depending on the location of the wire: inside or outside the furnace. Second, the effective anisotropies A_2^{eff} for "normal" and "reverse" spectra are not identical. To obtain conditions comparable to the experiments on zirconia, the Hf wire was placed in an alumina capsule similar to the ones used for the zirconia samples. For the data taken outside the furnace, this capsule was placed in an alumina tube, as used in the furnace. Unexpectedly, the elements of the furnace (graphite foil, thermal insulation, zirconium foil, water and the alumina container) reduced A_2 dramatically. A

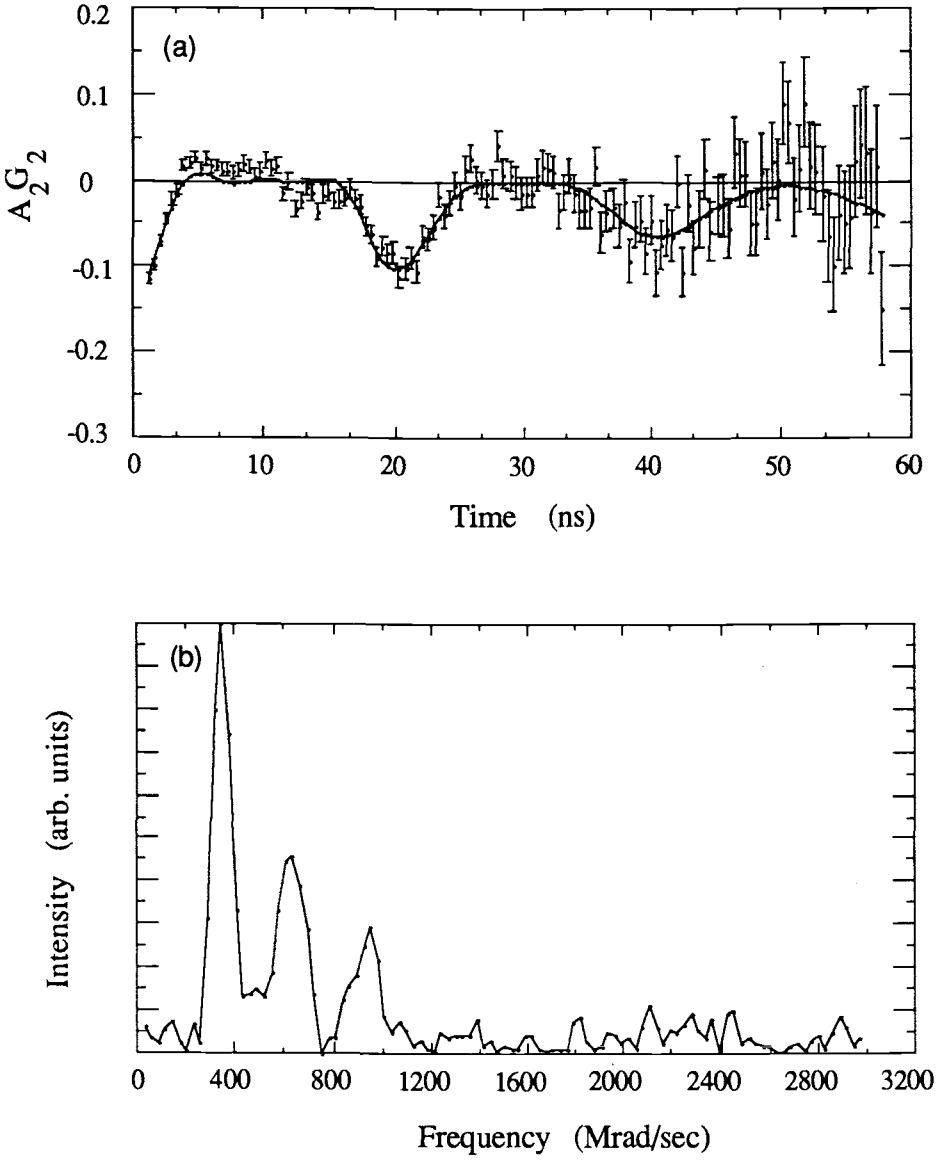

Fig. 5.1 (a) The time-domain spectrum with computer fit, and
(b) the Fourier spectrum for ^{181}Hf/Ta PAC of a Hf wire with 2.68 wt% Zr. The data were collected at a detector-sample distance of 3.8 cm.

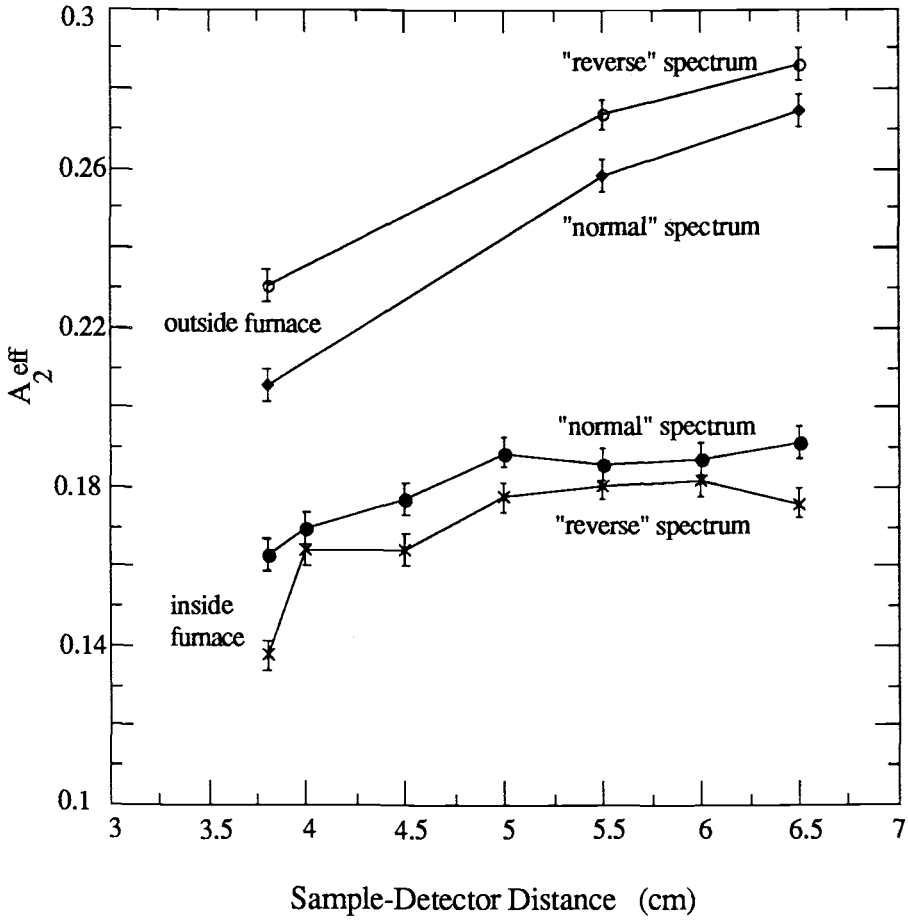

Fig. 5.2. The effective anisotropy, A_2^{eff}, obtained from computer fits to experimental data, as a function of the sample-detector distance.

possible explanation for this behavior is Compton scattering of γ-rays (see Compton scattering). Some parts of the furnace were only 7 mm apart from the detectors. So γ-rays scattered with small angles, which would have otherwise not been detected, entered the detector with larger angles than unscattered rays. Since their energy had not shifted significantly, they pass the TSCA windows. Similar to the discussion of finite detector and sample size, the Compton-scattered gamma-rays result in an average of angles in the spectra-ratio R(t), reducing A_2^{eff}.

Compton scattering is also a possible source for the difference of the effective anisotropies, A_2^{eff}, for "normal" and "reverse" spectra. If γ-rays are not equally scattered in all directions and the setting of the TSCA windows is not identical, then differences in A_2^{eff} are likely to occur. This behavior could also be caused by the electronics of the spectrometer, but unfortunately all efforts to detect any errors have failed. Therefore, in the analyses of the zirconia samples, an average of the values obtained for "normal" and "reverse" spectra was used to reduce possible systematic errors.

5.3. Results of Measurements on Cubic Zirconia

Zirconia samples with Y_2O_3 concentrations of 35.4 wt %, 27.8 wt %, and 16.9 wt % were used in this experiment. As mentioned in 1.1.2., the cubic phase is stabilized in alloys with an Y_2O_3 content above 16 wt %, so all samples used in this experiment were cubic, fully yttria stabilized. Of each of the three materials, 100 mg and 200 mg samples were made and placed in cylindrical alumina capsules. After irradiation with thermal neutrons to obtain the radioactive isotope ^{181}Hf, the samples were put in the PAC furnace and PAC spectra accumulated for about 24 to 48 hours. A

heating element in the furnace, connected to a temperature-controller, allowed regulation of the temperature of the sample. PAC spectra were collected in a temperature range from room temperature up to 1300°C. The experimental function $A_2G_2(t)$ was calculated from these data (4.2.) and fitted as described in 5.1.

The spectrometer geometry was not changed for the different temperature runs of one sample. Therefore, the effective anisotropy, A_2^{eff}, is the same for all temperatures. To find the appropriate value of A_2^{eff} for each sample, the anisotropy was first kept variable in the fits in addition to the relaxation constant λ, the PAC-frequency, ω_1, and the linewidth, δ. In Fig. 5.3. the temperature-dependence of the fitting parameter A_2^{eff}, as it was found for all samples, is shown. Since there is no physical explanation for the minimum of A_2^{eff} at about 600°C, the v-shape of the curve must be caused by the fitting routine itself. It can also be seen, as mentioned in 5.2., that A_2^{eff} is not identical for the "normal" and "reverse" spectrum. For further analyses, A_2^{eff} was therefore fixed to the average value for high temperatures (the horizontal line in Fig. 5.3.). The high-temperature average of A_2^{eff} for all three samples was consistent with the value obtained for the Hf wire at a sample-detector distance of 3.8 cm, the distance used for all zirconia samples.

After finding the parameter A_2^{eff}, $A_2G_2(t)$ was fitted again, now with fixed anisotropy, A_2^{eff}. The ratio $\omega_1:\omega_2:\omega_3$ was set to be 1:2:3, corresponding to axial symmetry. The reason for choosing this ratio, even though the sites have actually random symmetry, is because an arbitrary but fixed value is more consistent for fitting other parameters and it did not influence the fits considerably. So the variables, adjusted by the fitting routine were (i) the relaxation constant, λ, (ii) the PAC frequency, ω_1, and (iii) the linewidth of the EFG distribution, δ, accounting for imperfections in the crystal.

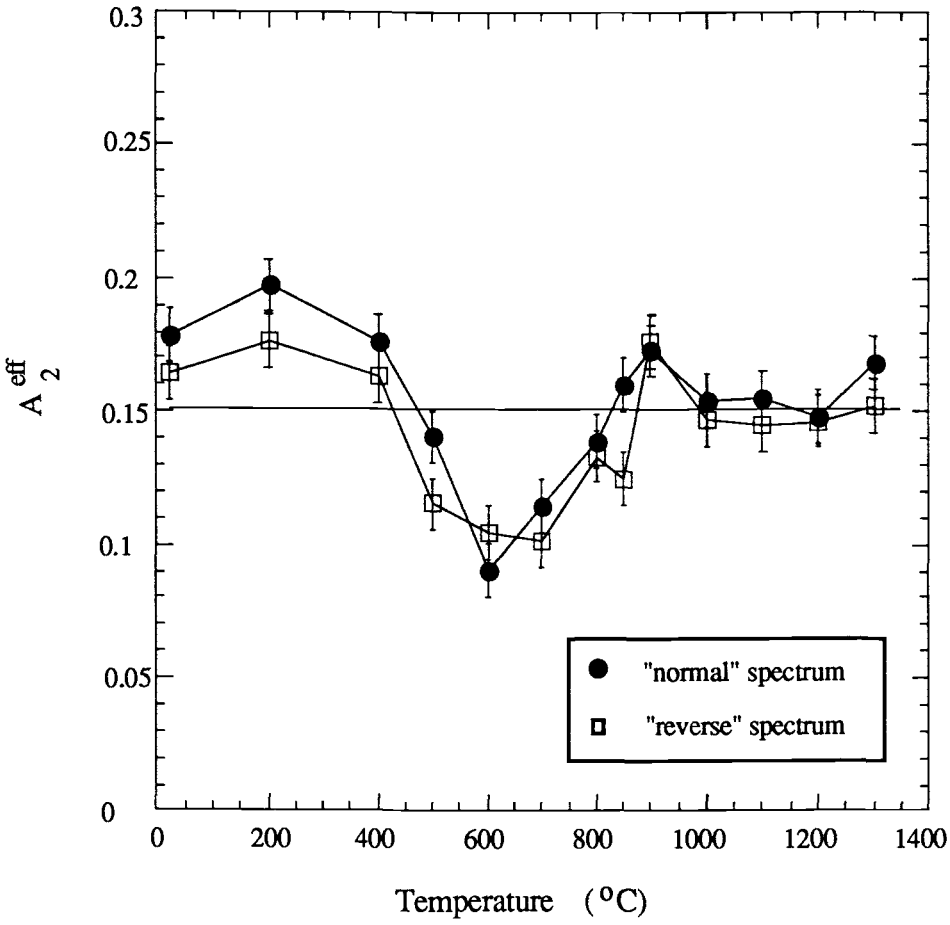

Fig. 5.3. The fitting parameter A_2^{eff} as a function of temperature.
The data were obtained from the zirconia sample with 16.9 wt % Y_2O_3.

In Fig. 5.4.and 5.5. typical PAC spectra (with computer fits) and Fourier transforms for lowest (24°C) and highest temperatures (1300°C) are shown. The Fourier spectra show a wide continuum of frequencies, which is shifted towards lower frequencies for the high-temperature runs. The function $A_2G_2(t)$ in these spectra does not decay to zero but approaches a constant value (hard core), which indicates a static interaction (2-29).

Spectra of intermediate temperatures (Fig. 5.6) show a decaying angular correlation, typical for time dependent interactions (2-77). The relaxation constant, λ, increases from room temperature up to a maximum at about 800°C and decreases for higher temperatures. In Fig. 5.7., where λ is plotted as a function of the inverse temperature, the two temperature regions can be clearly seen. The slopes of the curves are similar for all samples, but note that it is considerably smaller for the low-temperature data than for high temperatures. The maximum of λ is shifted towards lower temperatures for higher Y_2O_3-concentrations.

The results for $A_2G_2(t)$ in Fig. 5.5. and 5.6. indicate a temperature dependence of the frequencies in the angular perturbation function. The PAC frequency, ω_1, (Fig. 5.8.) is largest for lowest temperatures and almost constant up to about 400°C. For higher temperatures ω_1 decreases, but the curve flattens again above about 1200°C. Since ω_1 is directly proportional to the strength of the EFG interacting with the PAC probes, Fig. 5.8. also reveals the temperature dependence of the electric field gradient, EFG.

Fig. 5.9. shows the temperature dependence of the relative EFG distribution (or linewidth of the EFG distribution), δ. Even though the data fluctuate considerably, the tendency of δ to increase for higher temperatures is obvious. The average relative linewidth at 1300°C is about twice as big as at room temperature.

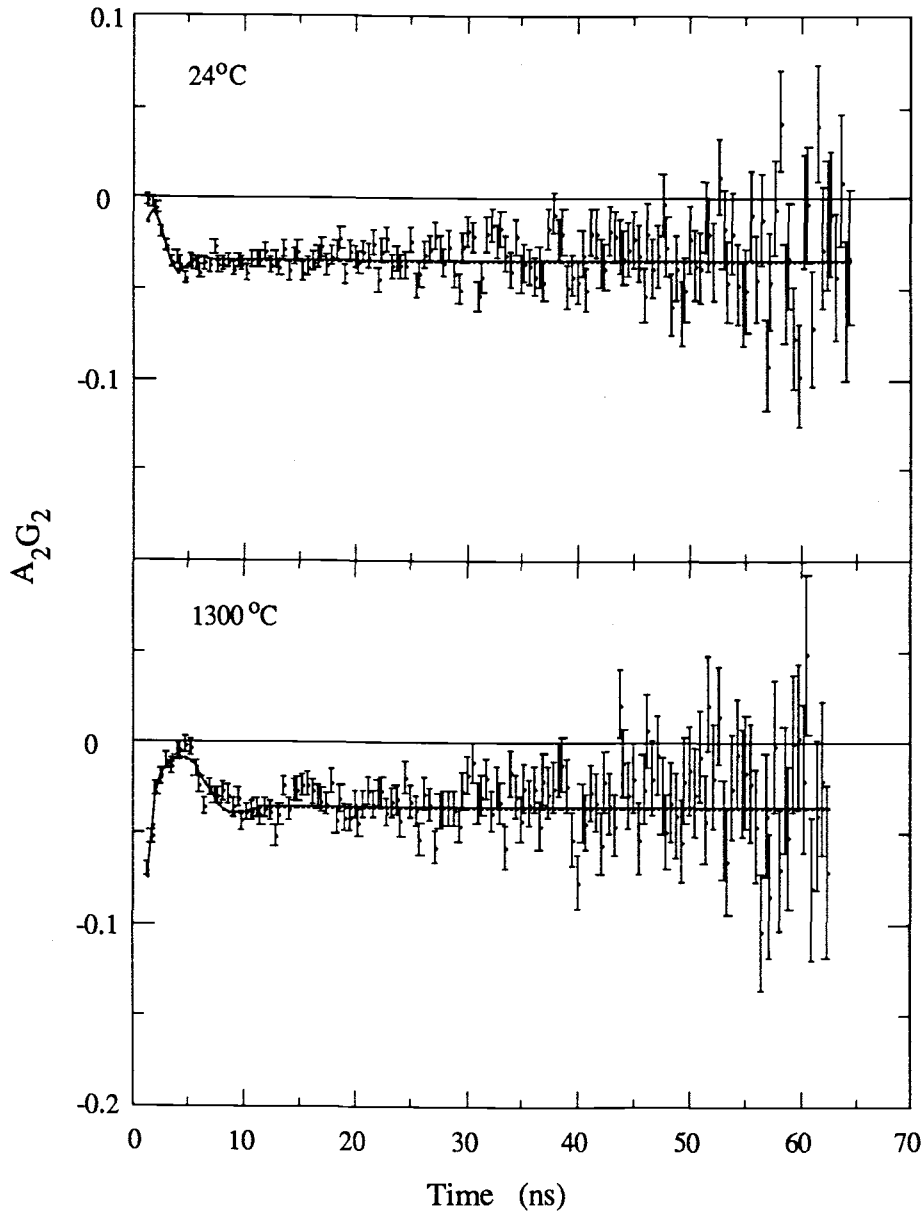

Fig. 5.4. PAC time spectra for ^{181}Hf/Ta PAC of cubic zirconia (16.9 wt % Y_2O_3) at lowest (24°C) and highest(1300°C) temperatures. The lines are fits discussed in the text. $A_2G_2(t)$ approaches a constant value (the hard core), indicating a static interaction.

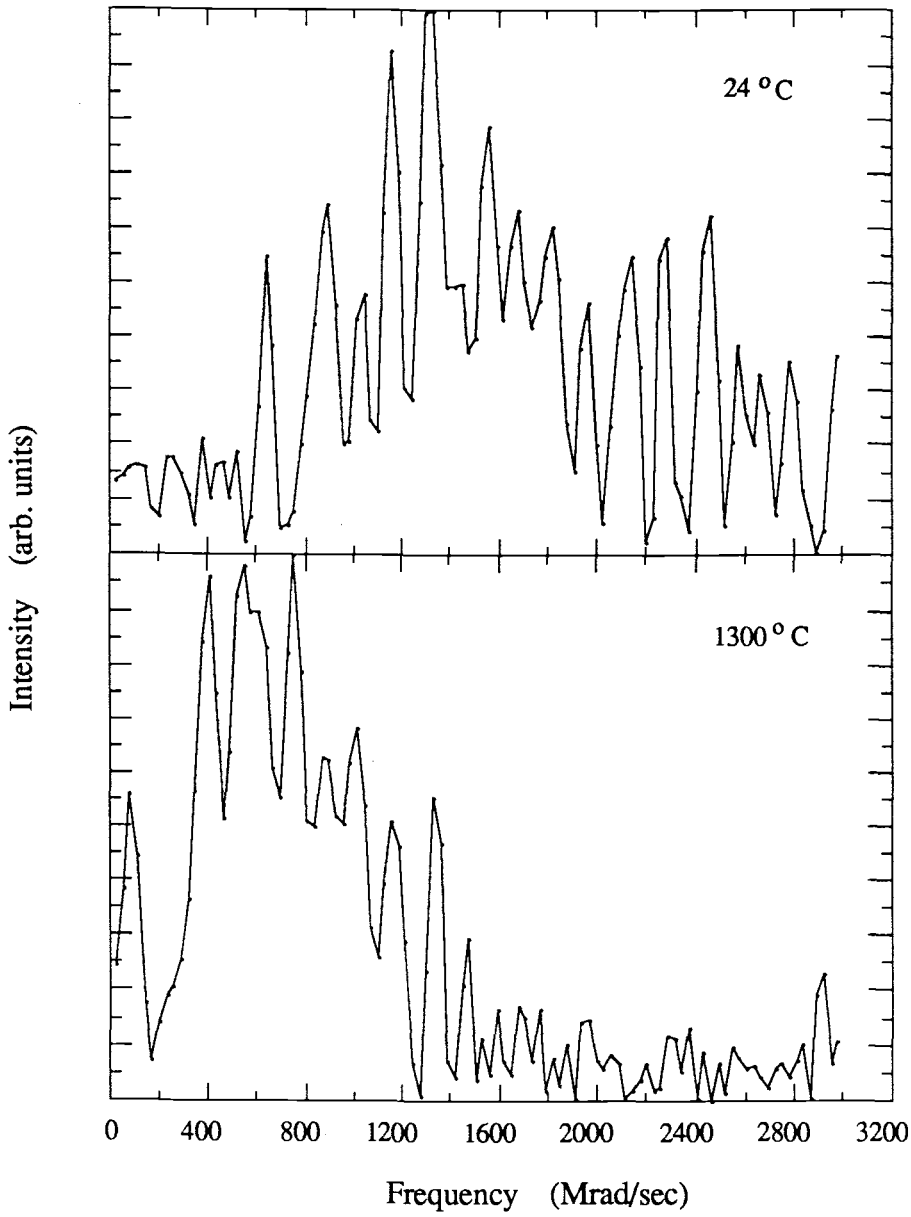

Fig. 5.5. Fourier spectra for ^{181}Hf/Ta PAC of cubic zirconia (16.9 wt % Y_2O_3) at lowest (24°C) and highest (1300°C) temperatures.

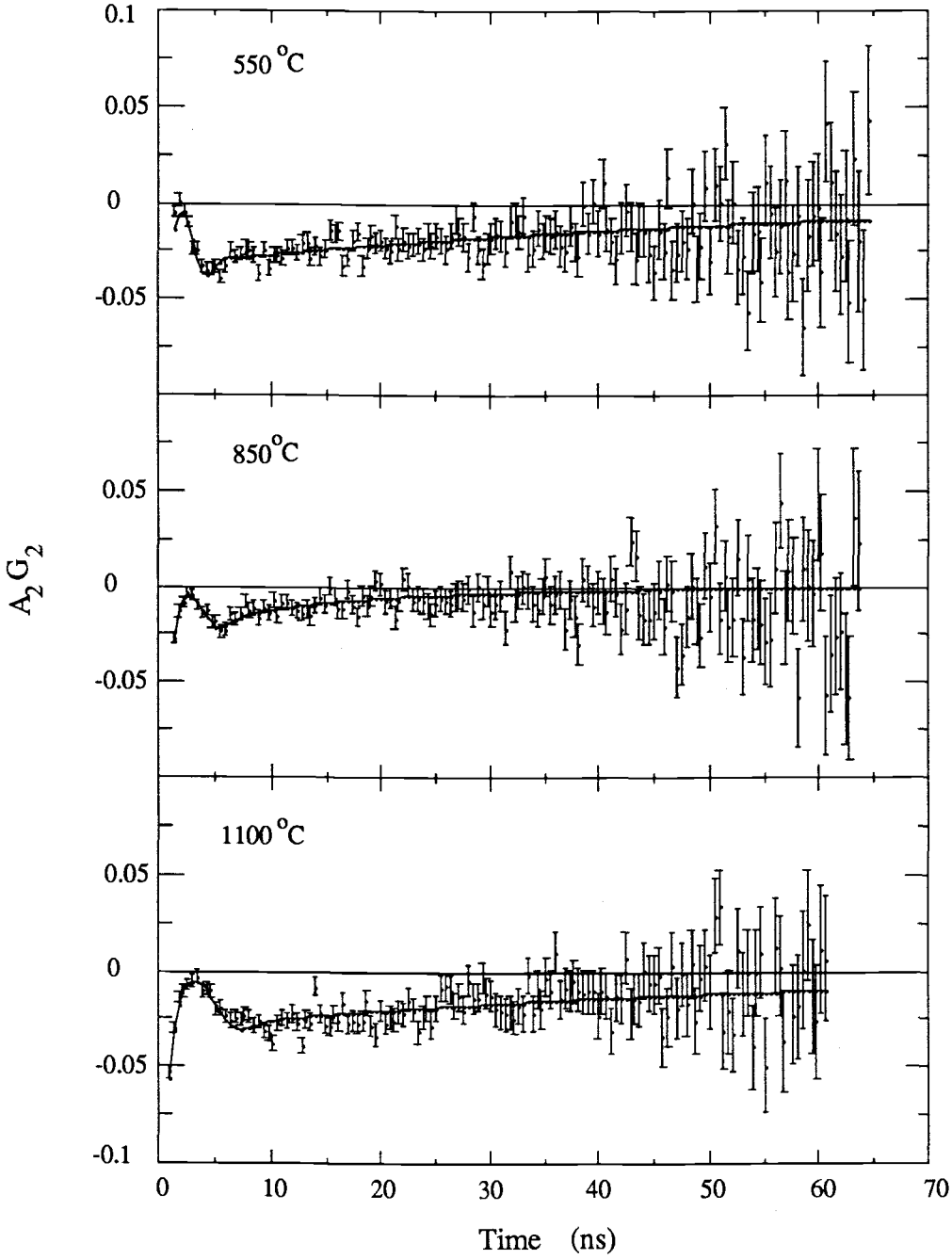

Fig. 5.6. PAC time spectrum for ^{181}Hf/Ta PAC of cubic zirconia (27.8 wt % Y_2O_3) at intermediate temperatures (550°C, 850°C, 1100°C). $A_2G_2(t)$ decays to zero, indicating a time-dependent interaction.

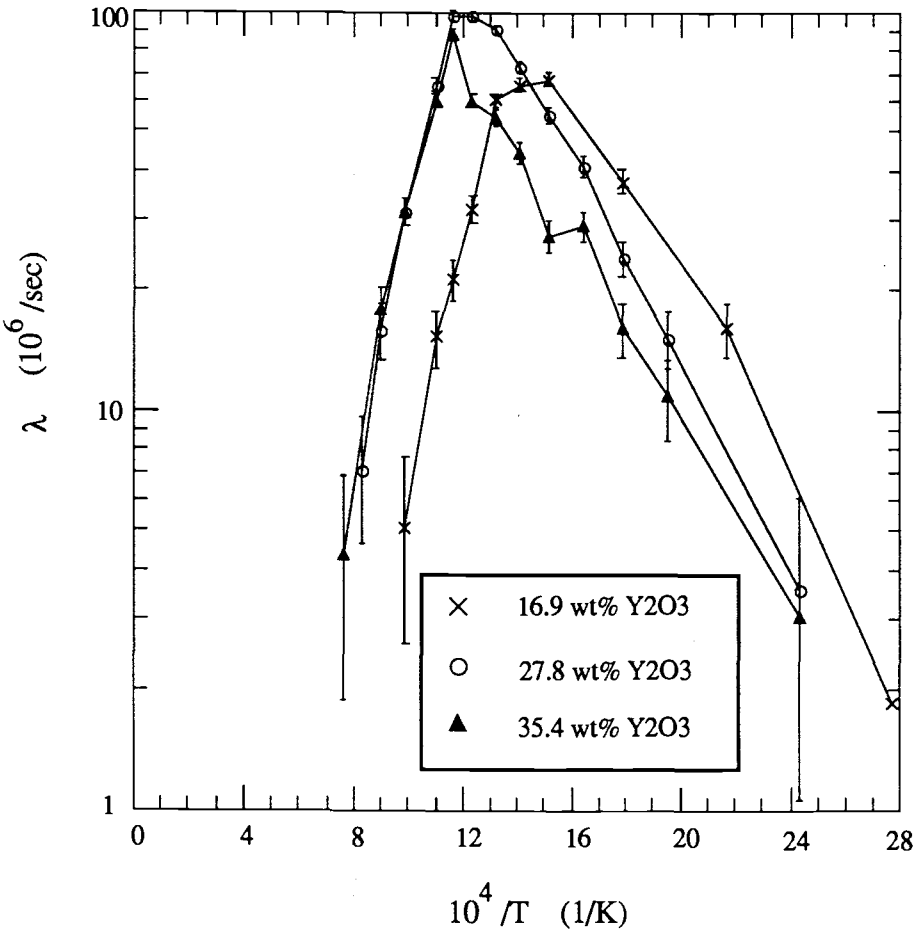

Fig. 5.7. Relaxation parameter, λ, as a function of the inverse temperature for ^{181}Hf/Ta PAC of cubic zirconia.

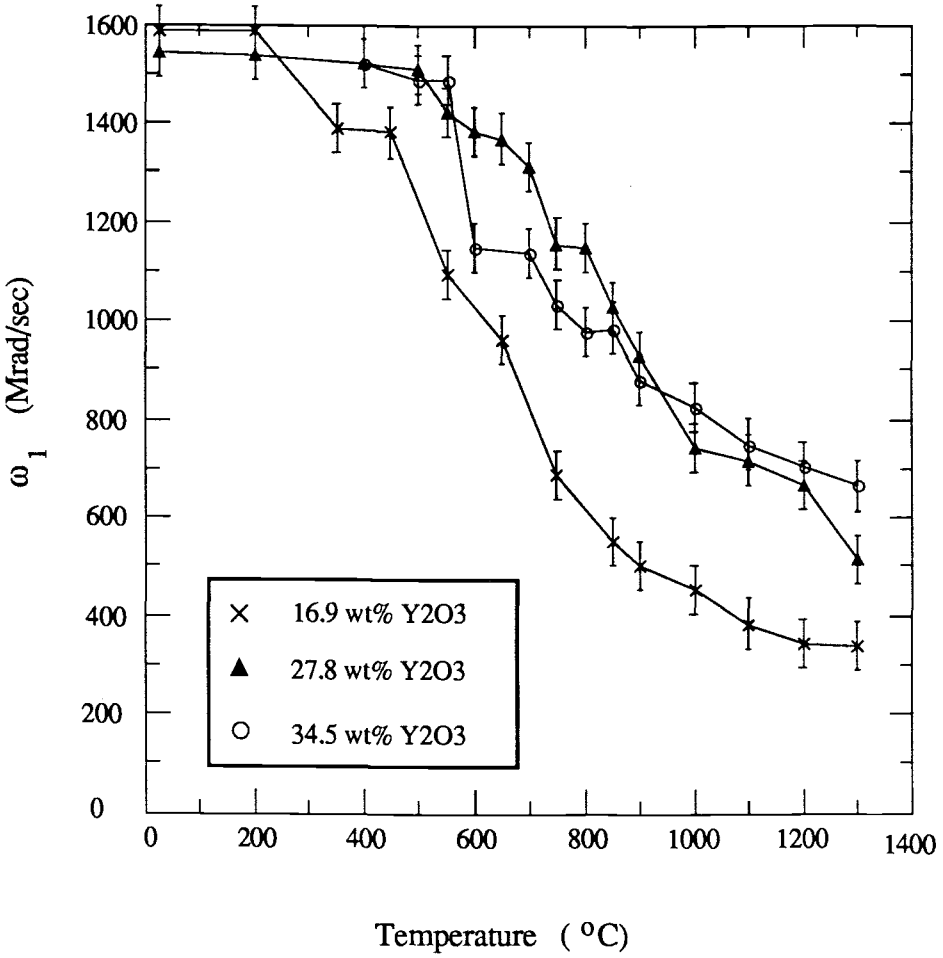

Fig. 5.8. PAC frequency, ω_1, as a function of temperature for ^{181}Hf/Ta PAC of cubic zirconia. Note that ω_1 is proportional to V_{zz}.

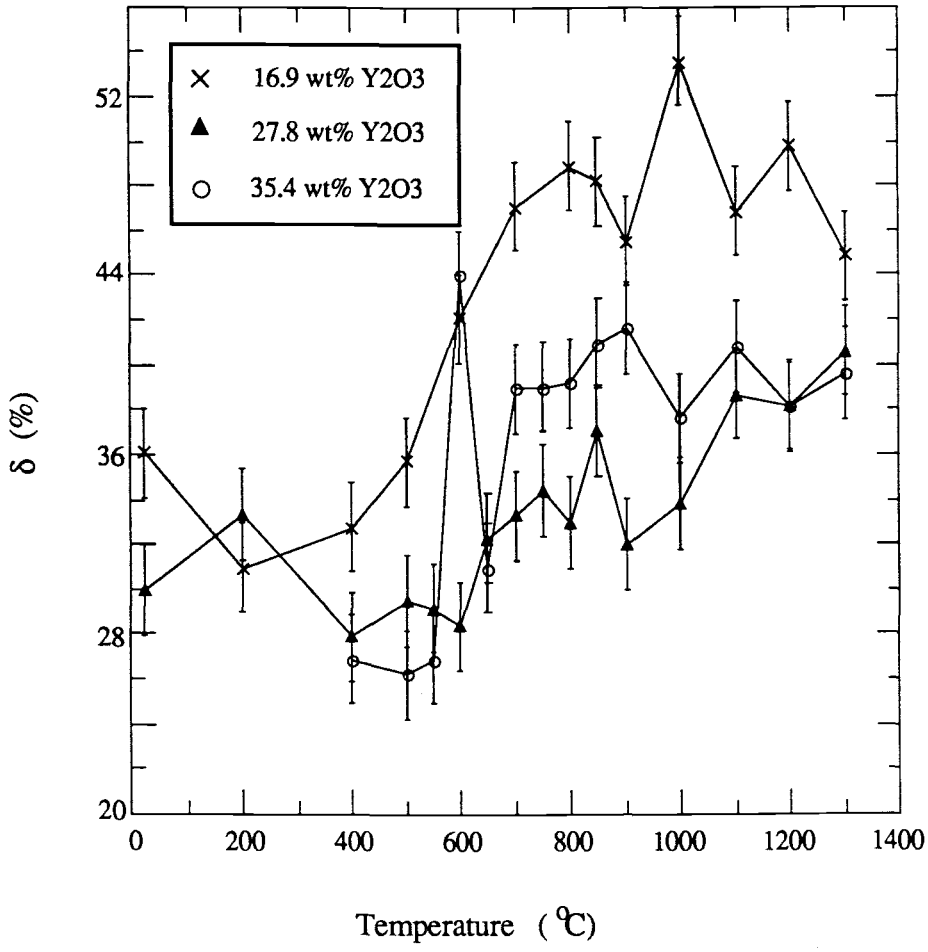

Fig. 5.9. Relative EFG distribution, δ, as a function of temperature for ^{181}Hf/Ta PAC of cubic zirconia.

5.4. Discussion of Results of PAC Measurements on Cubic Zirconia

The three different zirconia samples in this experiment were doped with 35.4 wt%, 27.8 wt%, and 16.9 wt% Y_2O_3. For dopant cations with a lower valence than four, the valence of Zr, oxygen vacancies are formed as charge compensating defects. Because Y is three-valent, one oxygen vacancy is created for every two Y atoms added. Therefore, the EFG at a cation site in fully stabilized (cubic) zirconia consists of two parts. The contributions are due to (i) the surrounding dopant cations with a negative effective charge, and (ii) the oxygen vacancies with a relative charge of +2.

In cubic zirconia the jump rate for oxygen vacancies is several orders of magnitude higher than for the cations. In fact, compared to the characteristic interaction time of the PAC probe with the EFG, $<\omega^2_Q>^{-1/2}$ (for ^{181}Ta about 15 ns), the cations can be considered static in the entire temperature range (24°C to 1300°C). The lattice part of the EFG experienced by the PAC probe is therefore static and temperature-independent.

The mobility of the oxygen vacancies on the other hand depends strongly on the temperature. For temperatures above 1200°C, the vacancy jump-rate is much higher than $<\omega^2_Q>^{-1/2}$, so that the occupation of all the anion sites around the probe are equally probable. Due to the cubic symmetry, the contributions of the vacancies average to zero, leaving only the static, temperature independent interaction due to the cations. This behavior can be seen especially for the sample with 16.9 wt% Y_2O_3 in Fig. 5.8., where ω_1 does not continue to decrease for temperatures above 1200°C.

As the temperature is lowered, the jump-rate of the vacancies decreases and the vacancy EFG does not average to zero. The time-dependent vacancy contribution to the EFG increases with decreasing temperature (see 5.4.2.) until the time between two successive vacancy jumps becomes greater than the lifetime of the ^{181}Ta intermediate

state. Further decrease in temperature below about 500°C leaves the EFG unchanged, and the interaction between PAC probe and EFG is static.

Equations (2-29) and (2-77) describe the interesting feature in which $A_2G_2(t)$ decays to zero for time-dependent interactions, whereas it approaches a constant value (hard core) for static EFGs. Fig. 5.4 and 5.6. show the hard core for lowest (24°C) and highest (1300°C) temperatures (static EFG) as well as the decay of $A_2G_2(t)$ for intermediate temperatures (fluctuating EFG due to vacancy jumps).

In stabilized cubic zirconia each individual PAC probe nucleus experiences a different EFG resulting from the particular dopant and vacancy distribution in the neighborhood of the probe site. The PAC spectra therefore consist of a wide frequency distribution (Fig.5.5.) resulting in a nonoscillatory behavior of the angular perturbation function $G_2(t)$ (Fig. 5.4. and 5.6.).

5.4.1. The Activation Energy, E_a, for the Oxygen Vacancy Motion

Electrical transport in cubic zirconia occurs by thermally activated hopping of oxygen ions via empty anion sites. The motion of oxygen ions can be described in terms of the motion of vacant anion sites, oxygen vacancies. It is equivalent to consider either an oxygen ion moving to a neighboring empty site, or the vacancy jumping to the site previously occupied by the ion. Due to the mobility of oxygen vacancies in cubic zirconia, it shows, like other fluorite structured oxides, a high ionic conductivity.

The frequency of the thermally activated vacancy hopping can be empirically described by

$$\nu = \nu_0 \exp\left\{-\frac{E_a}{kT}\right\} , \qquad (5\text{–}7)$$

where ν_0 is the attempt frequency, E_a is the activation energy, T is the temperature and k the Boltzmann constant. The characteristic fluctuation time of the perturbing field, τ_c, is then

$$\tau_c = \frac{1}{\nu} = \tau_0 \exp\left\{\frac{E_a}{kT}\right\} , \qquad (5\text{–}8)$$

with $\tau_0 = 1/\nu_0$. For high temperatures, meaning fast jumping vacancies and therefore rapidly fluctuating EFGs, the PAC relaxation constant, λ, is proportional to τ_c in the Abragam-Pound limit (2-67). So λ expressed in terms of the activation energy, E_a, is

$$\lambda \propto \tau_0 \exp\left\{\frac{E_a}{kT}\right\} . \qquad (5\text{–}9)$$

Experimental results of the PAC relaxation constant, λ, as a function of temperature are shown as a logarithmic plot in Fig. 5.10. According to equation (5-9), the slope of the curve is proportional to E_a. The lines are exponential fits to the data. Results of these E_a measurements are listed in Table 5.1.

The most important feature is that E_a does not depend on the concentration of doped Y_2O_3 (Fig. 5.11). This is in clear contradiction to all bulk ionic conductivity measurements. Even though there is a considerable scatter of the data from different authors,[70-81] they all agree in the fact that the activation energy, E_a, increases with the Y_2O_3 concentration in cubic zirconia samples.[82] In Fig. 5.11. the result of Ikeda et al[70, 82] is shown as a representative result for bulk ionic conductivity measurements. It

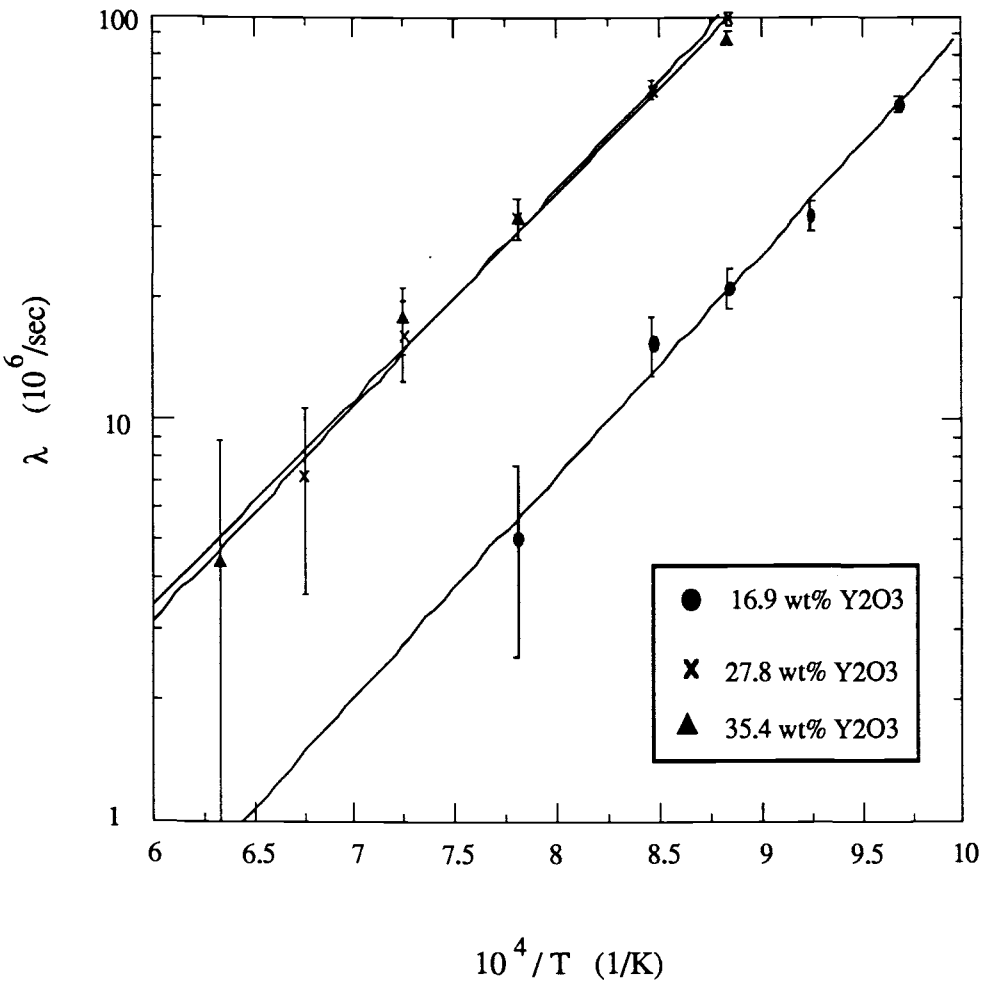

Fig. 5.10. Relaxation parameter, λ, as a function of the inverse temperature for ^{181}Hf/Ta PAC of cubic zirconia. The lines are exponential fits to the data. The activation energy, E_a, is proportional to the slope of the lines.

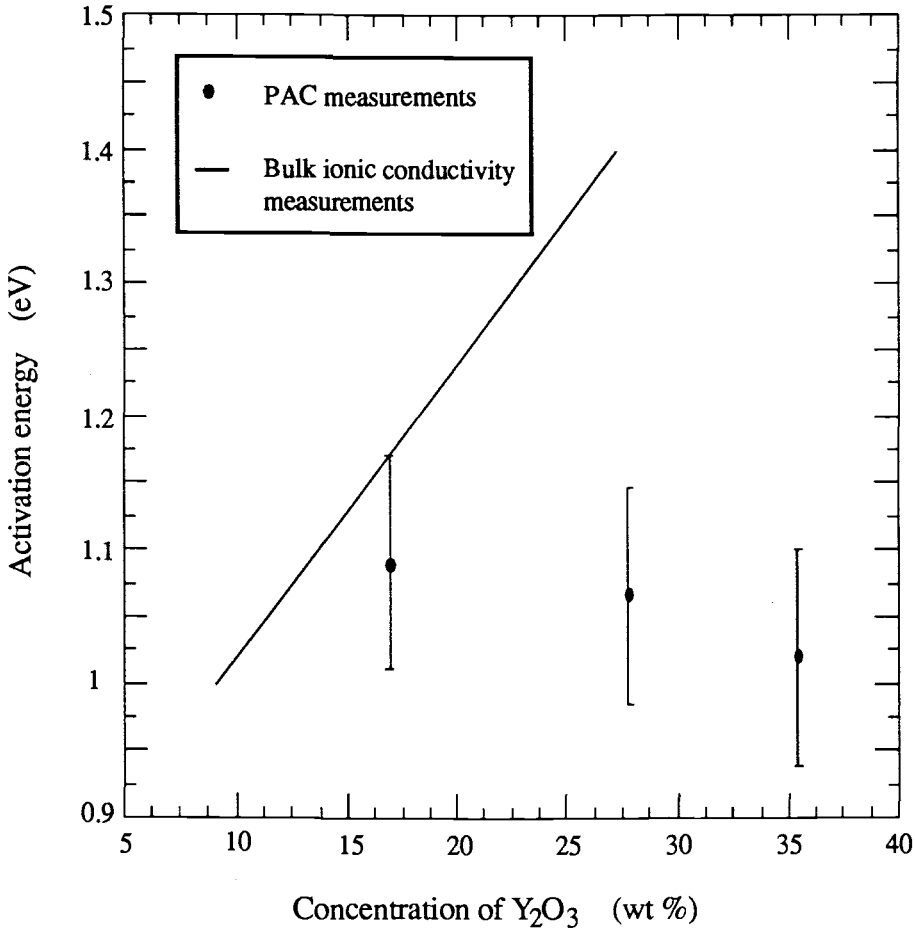

Fig. 5.11. Activation energy for oxygen vacancy hopping in cubic zirconia, E_a, as a function of Y_2O_3 concentration. The straight line for the bulk ionic conductivity measurements is a fit to data as reported by S. Ikeda et al.[70]

Table 5.1. Activation energy, E_a, for oxygen vacancy hopping in cubic zirconia. The PAC results were obtained from computer fits to the 181Ta PAC relaxation constant, λ. The conductivity results were taken from bulk ionic conductivity measurements as reported by S. Ikeda et al.[70]

wt % Y_2O_3	vacancy concentration (%)	E_a (PAC) (eV)	E_a (conductivity) (eV)
16.9	4.54	1.09	1.17
27.8	7.47	1.06	1.41
35.4	9.51	1.02	1.58

has been reported that E_a goes through a minimum at about 9 wt% Y_2O_3 (partially stabilized zirconia), but this is presently still a matter of controversy.

Starting with the simplifying assumption of a random distribution of dopant yttrium ions within the cation sublattice, the incorporation equation reads:

$$Y_2O_3 \rightarrow 2Y'_{Zr} + 3O_O^x + V_O^{\bullet\bullet} \quad . \tag{5–10}$$

From an electrostatic consideration, the mobile carriers, the oxygen vacancies, experience two kinds of interactions at large defect concentrations: either attractive with respect to aliovalent dopant cations, or repulsive with respect to other positively charged carriers. In the simplest approach, attractive interactions between vacancies and yttrium ions can be described in the Kröger-Vink notation as:

$$Y'_{Zr} + V_O^{\bullet\bullet} \rightarrow (Y_{Zr}, V_O)^{\bullet} \quad . \tag{5–11}$$

In this case, the defect structure consists of simple $(Y_{Zr}, V_O)^{\bullet}$ clusters or complexes and Y'_{Zr} ions distributed statistically. For higher dopant concentrations it is not meaningful to consider only simple complexes such as $(Y_{Zr}, V_O)^{\bullet}$ since, even with a random distribution of dopant ions, the probability that a vacancy has more than one Y ion in its immediate vicinity, as a nearest or next-nearest neighbor, becomes quite significant.[83,84] The sites with two or more Y ions as nearest neighbors are expected to act as deeper traps for oxygen vacancies, at least from a simple Coulombic consideration. The formation of a complex with two dopant ions can be written as:

$$2Y'_{Zr} + V_O^{\bullet\bullet} \rightarrow (2Y_{Zr}, V_O)^{\bullet} . \qquad (5\text{–}12)$$

Atomistic calculations performed by Butler et al.[85] yield a maximum binding energy for complexes with two Y ions. According to their calculations, the complex $(Y_{Zr}, V_O)^{\bullet}$ has a binding energy of 0.28 eV compared to 0.63 eV for $(2Y_{Zr}, V_O)'$ with respect to the total energy of the isolated defects.

It must be noted that in all of these considerations a random distribution of dopant ions is assumed, which has been questioned by many investigators[86] and has not been solved satisfactorily at the present time. In fact, Auger electron spectroscopy was used to determine the composition near grain boundaries, and an enrichment with Y was observed with respect to the bulk with an enrichment factor of 1.5.[87]

All these arguments do not explain an increase of the conductivity with the dopant concentration in cubic zirconia, obtained by bulk ionic conductivity measurements. Even if the mobility of vacancies trapped into associates is strongly diminished compared to a free vacancy, the formation of complexes decreases only the relative and not the absolute number of free defects. Many different models have been developed to explain the conductivity variation. The basic concept of these models is (i)

to attribute a larger binding energy to a complex formed by a vacancy and several dopant ions and (ii) to generate a distribution of binding energies according to the respective positions of the vacancy and dopants lying in its neighborhood.[84] Some models predict at least qualitatively the experimental results for the conductivity, but it seems as if the conclusion which is drawn from these considerations, namely an increase of the activation energy with increasing dopant concentrations, is rather vague.

As opposed to conductivity measurements, PAC spectroscopy does not average over macroscopic regions. So all bulk- and surface-effects, which could vary with the Y concentration and change the results for the conductivity, have no influence on our results. We therefore propose that the activation energy is independent of the dopant concentration, and that explanations for the behavior of the ionic conductivity, other than a concentration-dependence of E_a, have to be found.

5.4.2. The Temperature Dependent EFG

In Fig. 5.8. the PAC frequency ω_1 is shown as a function of temperature. For cubic zirconia where the asymmetry parameter η is equal to zero, ω_1 is according to (2-46, 2-58):

$$\omega_1 = 6\omega_Q = 6\frac{eQ}{4I(2I-1)\hbar}V_{zz} . \qquad (5\text{–}13)$$

As discussed above, for temperatures above 1200°C and below about 500°C the EFG is time independent and does not vary considerably with temperature. For intermediate temperatures the motion of oxygen vacancies cause the EFG to fluctuate and the PAC

probe experiences a time-dependent interaction. In this temperature region, the EFG is not only time-dependent but also varying with temperature. The PAC spectra of all Y_2O_3 concentrations investigated in this work show a decreasing V_{zz} for increasing temperatures (example for 16.9 wt % in Fig. 5.12.).

A possible explanation for this behavior is EFG shielding due to occupation of higher energetic vacancy sites near the Ta PAC probe. Since both the ^{181}Ta ions and the oxygen vacancies have positive effective charges, they repel each other and the energy of a ^{181}Ta first neighbor oxygen site is higher than the energy of an oxygen site next to a Zr ion by an amount of ΔE. The measured EFGs are too small to admit the possibility of first neighbor oxygen vacancies, even at room temperature. If the vacancies were distributed randomly before the ß-decay of ^{181}Hf to ^{181}Ta, they must have therefore been forced out of their next-neighbor positions during the ß-decay. So immediately after the decay, vacancies do not occupy sites next to the PAC probe.

At temperatures below 500°C where the jump time of the oxygen vacancies is larger than the characteristic interaction time of the PAC probe with the EFG, $<\omega^2_Q>^{-1/2}$ (for ^{181}Ta about 15 ns), the vacancy configuration appears to be static, meaning the vacancies have no time to jump back into next neighbor sites during the lifetime of the intermediate state. The EFG in this temperature region is therefore primarily due to Y ions.

As the temperature rises and the jump time becomes comparable to $<\omega^2_Q>^{-1/2}$, the interaction time is long enough for vacancies to jump back to next neighbor positions of the PAC probe. The probability of occupying these sites is proportional to $\exp\{-\Delta E/kT\}$ and increases with temperature. Due to electrostatic attraction, sites with one or more Y neighbors will be occupied first. The vacancy contribution to the EFG at the probe site reduces the EFG due to the Y ions since they have opposite effective charges. At higher temperatures more and more of these next neighbor sites are

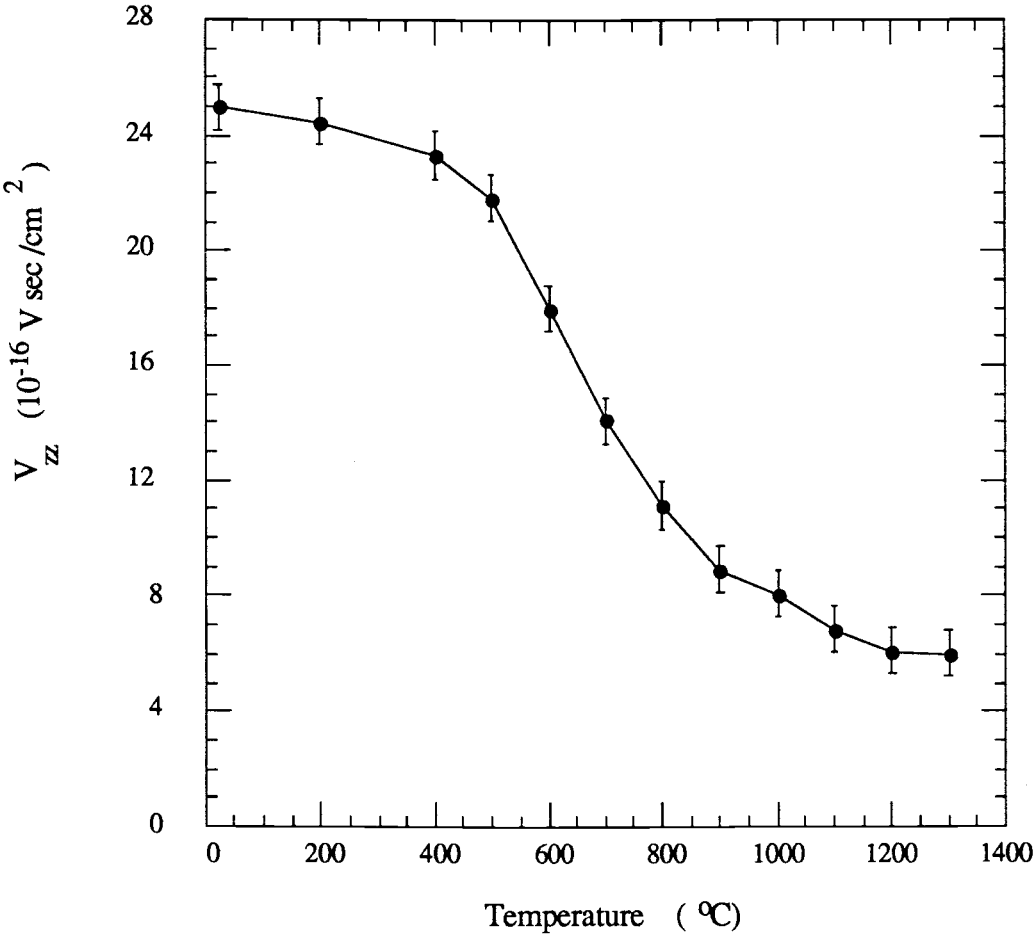

Fig. 5.12. Typical magnitude of the EFG component V_{zz} of cubic zirconia (data for sample with 16.9 wt % Y_2O_3). The line is a guide to the eye.

occupied by vacancies, gradually reducing the EFG (Fig. 5.12.).

In Fig. 5.13. and 5.14. the logarithm of V_{zz} is plotted versus the inverse temperature, and it can be seen that the data for temperatures above 600°C can be fitted to an exponential (note that occupation probability of next neighbor sites is proportional to $\exp\{-\Delta E/kT\}$). Fits to expressions of the form $V'_{zz} + V^0_{zz}*\exp\{\Delta E/kT\}$ yield an asymptotic value of $V'_{zz} = 0.39*10^{17}$ V/cm^2, and a energy difference ΔE of about 0.2 eV.

To estimate the screening, the contributions to the EFG due to a single Y and and the surrounding vacancies is considered. If the Ta ion is at the origin, then oxygen sites neighboring both the Ta and the Y ion are at $(\pm 1, \pm 1, 1)$ and the Y at (0, 0, 2). The contribution to the EFG due to the Y ion with the effective charge -1 is 0.0078 e, whereas vacancies (charge +2) on the four oxygen sites contribute - 1.3 e. Let p be the occupation probability, which is very small since even for 1300°C $\exp\{-\Delta E/kT\}$ is only 0.16. The reducing EFG due to oxygen vacancies is therefore about 166p times the EFG due to the Y.

At low temperatures p is zero, and the EFG at the probe site is primarily due to the Y ions. As the temperature and therefore p rises, the EFG is reduced by the negative vacancy contribution, which could even become larger than the Y contribution.

Fig. 5.15. shows V_{zz} as a function of the Y_2O_3 concentration for five different temperatures between 24°C and 1300°C. For higher dopant concentrations, meaning also vacancy concentrations, the EFG has the tendency to increase.

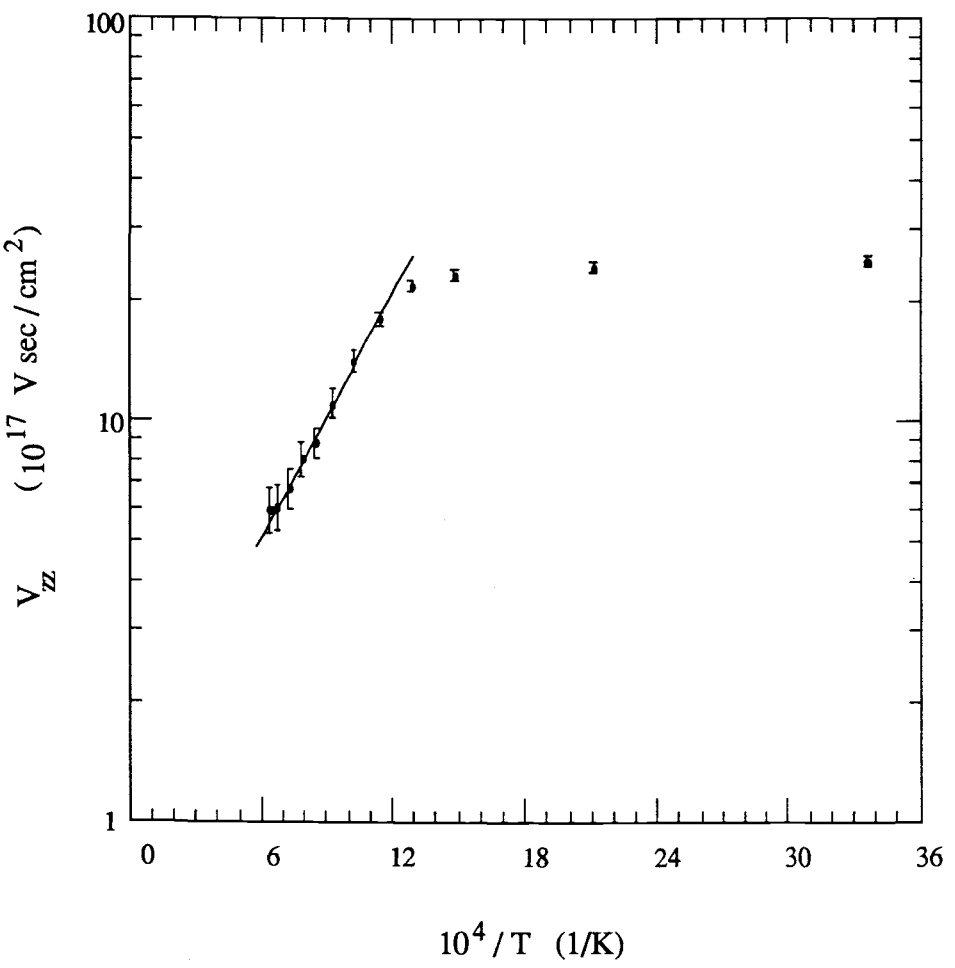

Fig. 5.13. Typical magnitude of the EFG component V_{zz} of cubic zirconia (sample with 16.9 wt % Y_2O_3) as a function of the inverse temperature. The line is an exponential fit to the high temperature data (T>600°C).

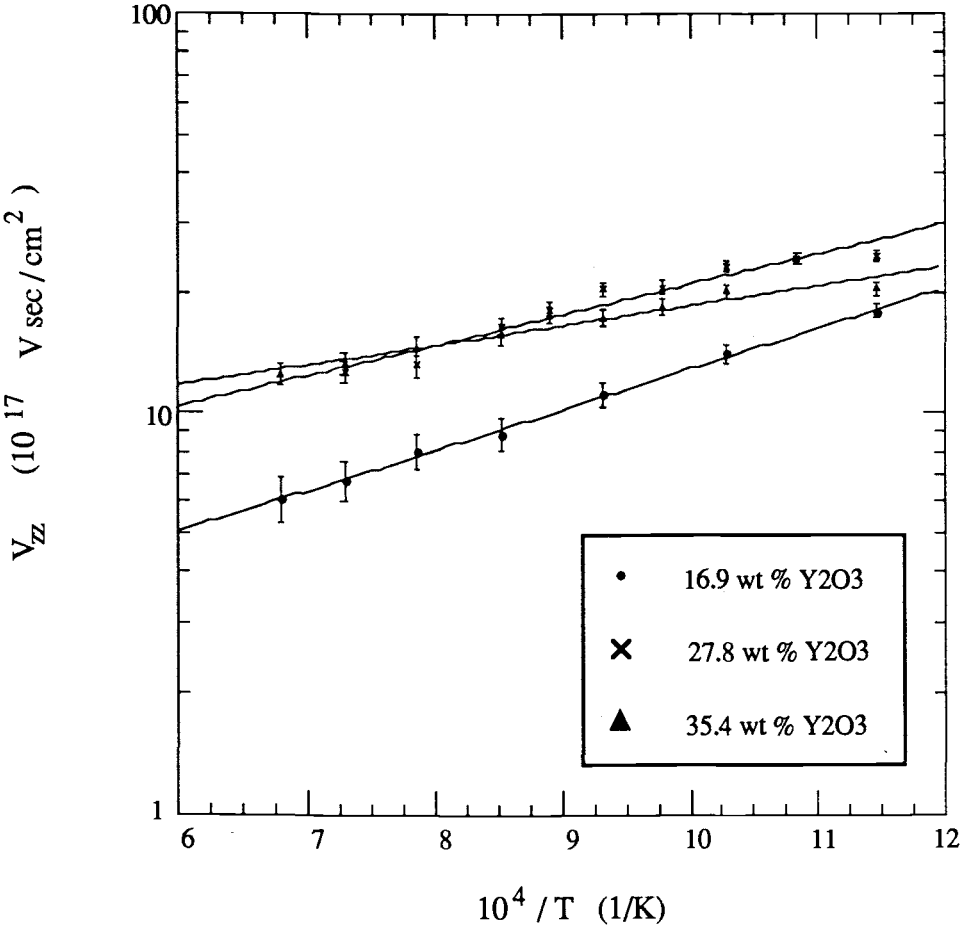

Fig. 5.14. Magnitude of the EFG component V_{zz} of cubic zirconia as a function of the inverse temperature. Data for temperatures T>600°C. The lines are exponential fits to the data.

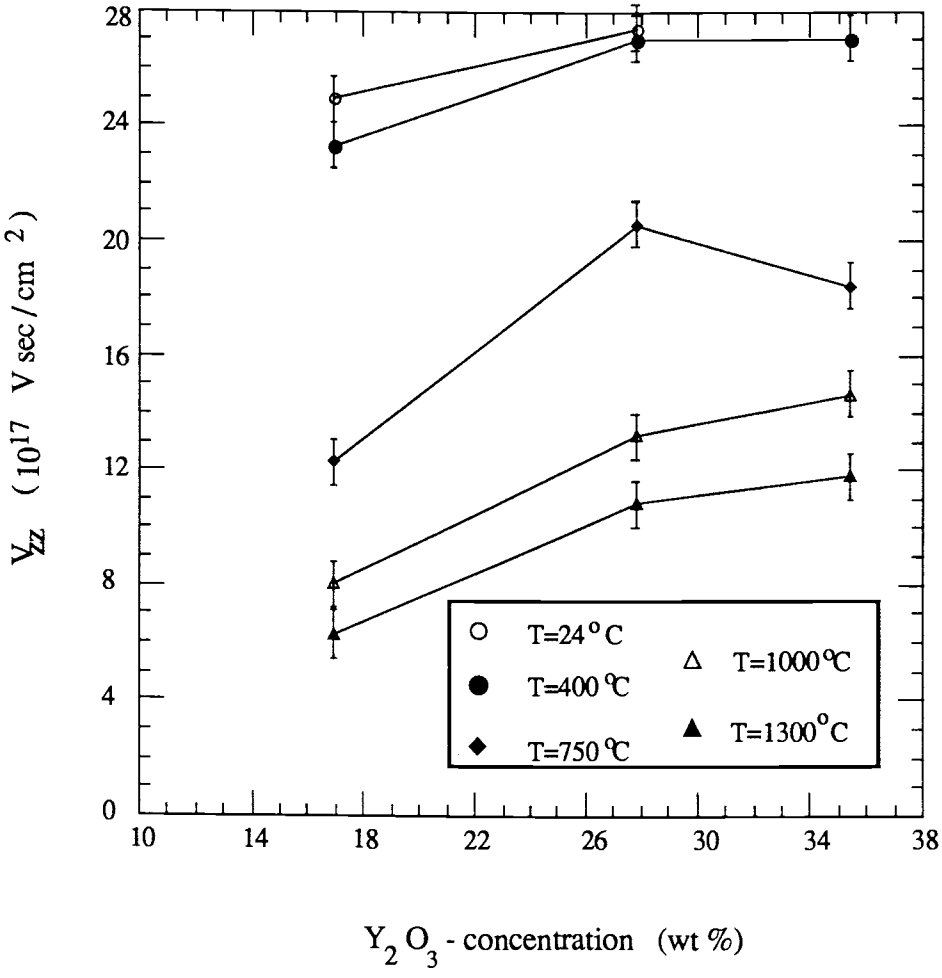

Fig. 5.15. Magnitude of the EFG component V_{zz} of cubic zirconia as a function of the Y_2O_3 concentration. The lines are guides to the eye.

5.4.3. Annealing of Samples

A comparison of PAC results, using the same sample but with a different "history", reveals an important fact: the samples were not homogeneous unless they were heated up to at least 1300°C for several hours.

Since the Y_2O_3 content was 16.9 wt % and more, one would have expected to obtain fully stabilized (cubic) zirconia. But PAC Fourier spectra of samples which were not annealed (Fig.5.16.) showed an additional site with discrete frequencies besides the typical result for cubic symmetry (wide frequency distribution). This site resulted in a noticeable oscillation of the angular perturbation function $G_2(t)$.

The frequencies of the additional site in Fig. 5.16. (ω_1 is about 700 Mrad/sec at room temperature) could be caused by a fraction of monoclinic zirconia in the material. The monoclinic phase is not stable at higher temperatures (see Fig. 1.2.), which would explain the annealing of the samples. There are many other possible sources for the differences in the PAC spectra. It is not unlikely, for example, that high temperatures enlarge the grains in the material. The Y content near grain boundaries is higher than in the bulk,[87] resulting in an inhomogeneous Y distribution which is temperature-dependent.

Also the PAC frequency ω_1 of the cubic site is influenced by the annealing process. Fig. 5.17. shows ω_1, corresponding to the Fourrier spectra in Fig. 5.16. After a spectrum was taken at room temperature (spectrum a), the temperature of the material was gradually raised to 1300°C and then kept at 1600°C for 24 hours and quenched to room temperature within 5 min (spectrum c). The sample was then heated to 1300°C again and very slowly (3 weeks) cooled down to 24°C (spectrum b). PAC spectra were accumulated for various temperatures during these cycles and Fig. 5.17. gives the resulting values for ω_1. It is striking that ω_1 shows the behavior of a

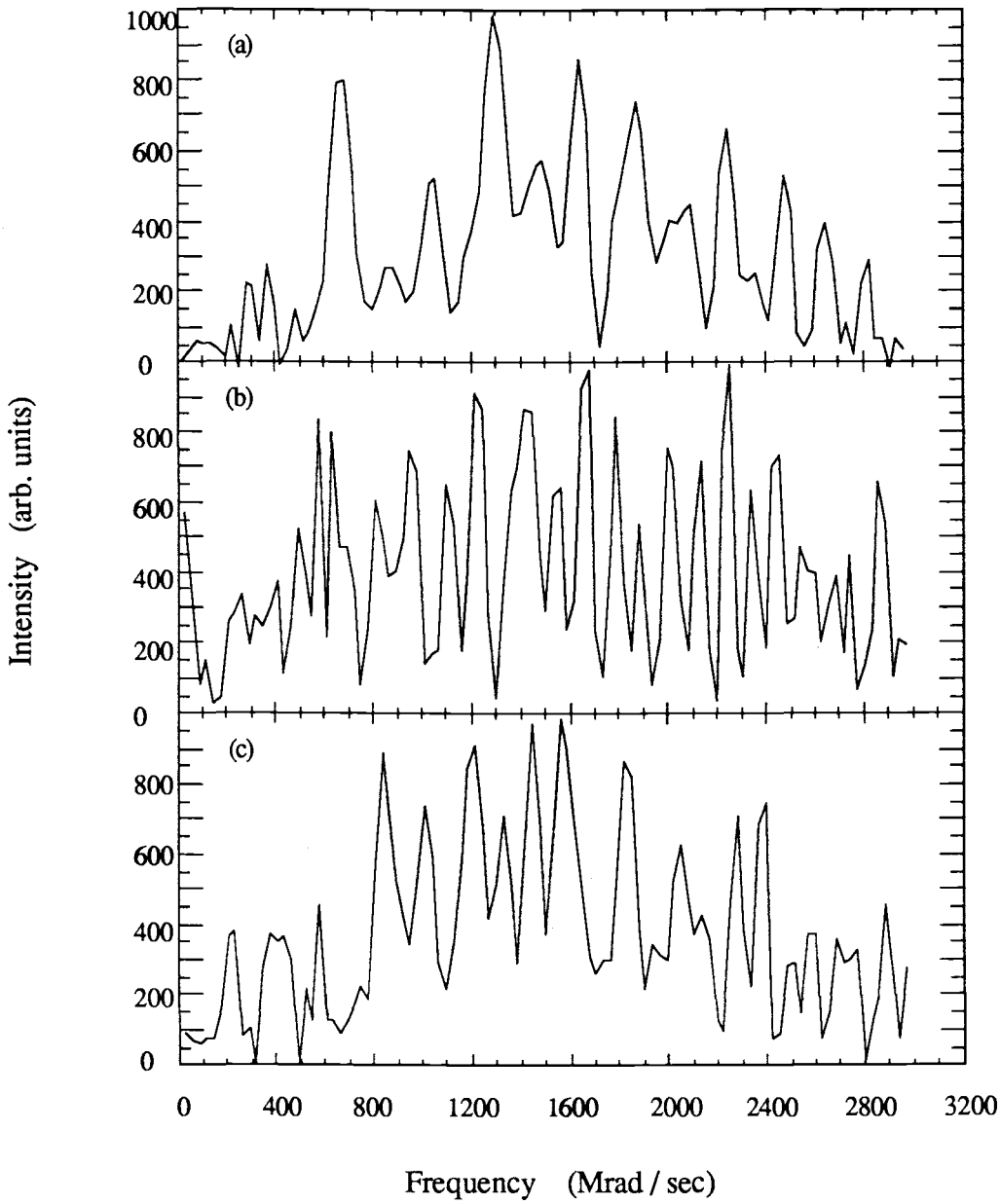

Fig. 5.16. Fourier spectra for ^{181}Hf/Ta PAC of cubic zirconia (16.9 wt % Y_2O_3) at 24°C:
(a) without preheating
(b) 3 weeks after heating up to 1300°C for 24 hours (slowly cooling)
(c) immediately after heating up to 1600°C for 24 hours.

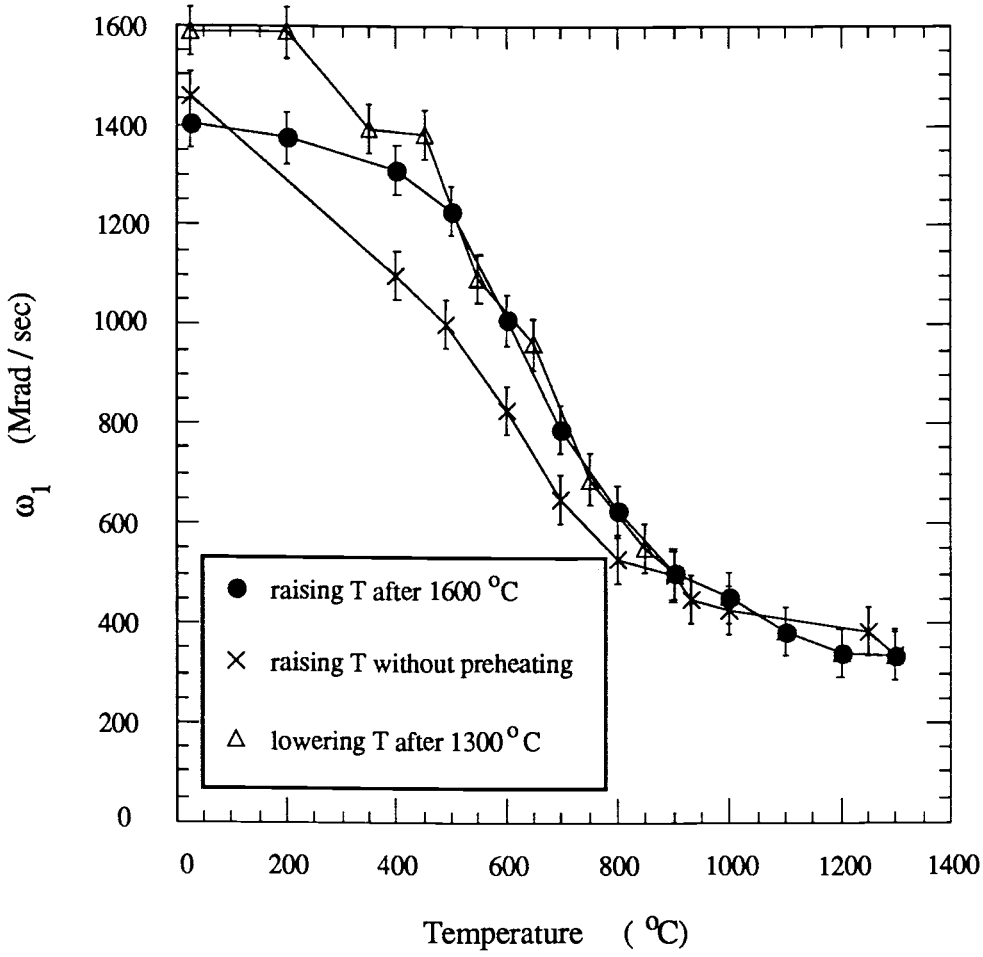

Fig. 5.17. PAC frequency, ω_1, as a function of temperature for ^{181}Hf/Ta PAC of cubic zirconia.

hysteresis.

To find a way of sufficiently annealing the materials, a sample was heated up to 1300°C and PAC spectra taken for three days. The spectra as well as the Fourier spectra of the second day did not differ from the ones taken on the first or third day and no second site could be detected. We therefore concluded that the material is annealed after about 24 hours at 1300°C and all the data presented in this work were taken from samples which have been annealed for at least one day at 1300°C.

6. Computer Simulation of PAC Spectra

Complementary to experimental measurements of PAC spectra, a program was developed to obtain computer-simulated results for the angular perturbation function, $G_2(t)$, of zirconia. By simply adjusting the appropriate parameters, this method allows investigation of how different conditions in the simulated "sample" effect the function $G_2(t)$. Computer simulations provide a useful tool in the attempt to answer questions which can presently not be solved by fitting experimental data to theoretically calculated models. As mentioned in 2.5., there are even cases for which no satisfactory analytical fitting function exist. An example of such an unsolved question is the time-dependent angular perturbation function in the low-temperature region in powder samples.

The simulated angular perturbation function was obtained in two steps:

- Simulating a fluctuating EFG.
- Calculating the angular perturbation function $G_2(t)$.

6.1. Simulation of a Fluctuating EFG

On an Apple Macintosh II computer, a crystalline lattice was set up with the PAC probe located at the center of the crystal. Vacancies were randomly distributed in the lattice and were then allowed to jump to neighboring sites. After each jump, the five components of the EFG (meaning: V_{xx}, V_{yy}, V_{xy}, V_{xz}, and V_{yz}) were calculated and saved to a disk together with the corresponding time-variable.

The time-dependent EFGs were simulated under some simplifying assumptions. The assumptions, compared to the situation in a real lattice are listed in Table 6.1.

Table 6.1. Assumptions in the simulation, compared to the situation in a real lattice.

Assumptions in the simulation	Situation in a real lattice
• The cationic sublattice of the oxygen atoms is cubic.	• In cubic zirconia, the oxygen-lattice is actually a fluorite structure.
• The atoms of Zr and Y are randomly distributed. As a result of this, all the contributions to the EFG due to Zr and Y average out to zero. Thus for the calculation of the EFG, only oxygen vacancies with an effective charge of +2 have to be taken into account.	• Replacing a Zr^{4+} with a Y^{3+} results in an EFG different from zero because the cubic symmetry is broken. Because the jump-rate of Y^{3+} is several orders of magnitudes smaller than of the vacancies, the EFG due to Y^{3+} can be considered to be static.
• The oxygen vacancies can be described as point-ions.	• Exact electronic structures and charge-distributions have to be considered in a realistic calculation.
• There are no interactions between the oxygen vacancies and no interactions between vacancies and Zr or Y. As a result, the distribution and motion of the vacancies is totally random.	• For very low doping concentrations the interactions might be negligible, but there is clear experimental evidence for different interactions between Y ions and oxygen vacancies.[82, 84, 85, 86]
• The vacancies can only hop to next-nearest-neighbor sites.	• 'Diagonal' jumps might happen in a real lattice, but they are not expected to change the fluctuating EFG qualitatively.

Table 6.1. continued

• The PAC probe repels oxygen vacancies so that they never occupy nearest neighbor sites to the probe.	• Experimental results of PAC spectra using a ^{181}Ta probe seem to support this assumption.

In a later stage of this work, more realistic conditions could replace some of these assumptions.

The program to simulate the fluctuating EFG was written in PASCAL (Light-speed-Pascal), which is a clearly structured language and was divided into several subroutines, called procedures. This allowed easy access to parameters, which could be adjusted for the different conditions under which the EFGs were desired to be simulated. These parameters included the size of the crystal, the crystallographic configuration (cubic, FCC, BCC, etc.), the concentration of vacancies in the crystal, the number of vacancy-jumps, and the seed for the random-number generator (RNG).

In early stages of this work, a random number generator following Knuth's algorithm[88] was used, but this turned out to be much slower than using the Macintosh built-in RNG. Results, obtained by the different RNGs, do not vary substantially,[89] and so for all simulations presented in this work, the built-in RNG was used. The first seed for the RNG was chosen by the user at the beginning of the program and all the other seeds, necessary for random-numbers for the random doping with vacancies and the random jumps, were derived from the start-seed.

A flow-chart of the program is given in Fig. 6.1. The first step in the program was to establish a crystal lattice with randomly doped vacancies. For this purpose, the user was asked to input the size of the crystal, the vacancy concentration m, and the first

seed for the RNG. According to the chosen concentration, a random-number decided at every possible site in the crystal, if a vacancy was positioned at this particular site. If a site was decided to be doped with a vacancy, its coordinates were stored in an array as integer multiples of the lattice parameter a, and its contributions to the components of the EFG were calculated. The contributions of all the vacancies were added up to yield the total EFG-components at time t=0, meaning before the vacancies start to jump.

The program then informed the user about the number of vacancies in the crystal and asked for input of the number of jumps desired for a simulation.

An abstract time variable which continuously added a '1' to its value was used to record the time. Later in the process, when the angular perturbation function $G_2(t)$ was calculated from the time-dependent components of the EFG, the user could choose to assign any "real" meaning to this variable. During every time-step there was a chance of 20% for any vacancy in the crystal to jump.

Once the random-number decided whether a vacancy jumped, another random-number determined which of the vacancies was hopping. The RNG was again used to decide in which direction the vacancy was moving. Before the contributions to the EFG-components due to the old position were deleted and the ones due to the new location added, a subroutine checked if the vacancy had jumped out of the chosen size of the crystal, or if it had jumped on a site that was already occupied by a vacancy. In the case of a jump on an already doped site, the vacancy simply hopped back to the old position. The case of jumping out of the crystal was a bit more complicated and two different boundary conditions have been used.

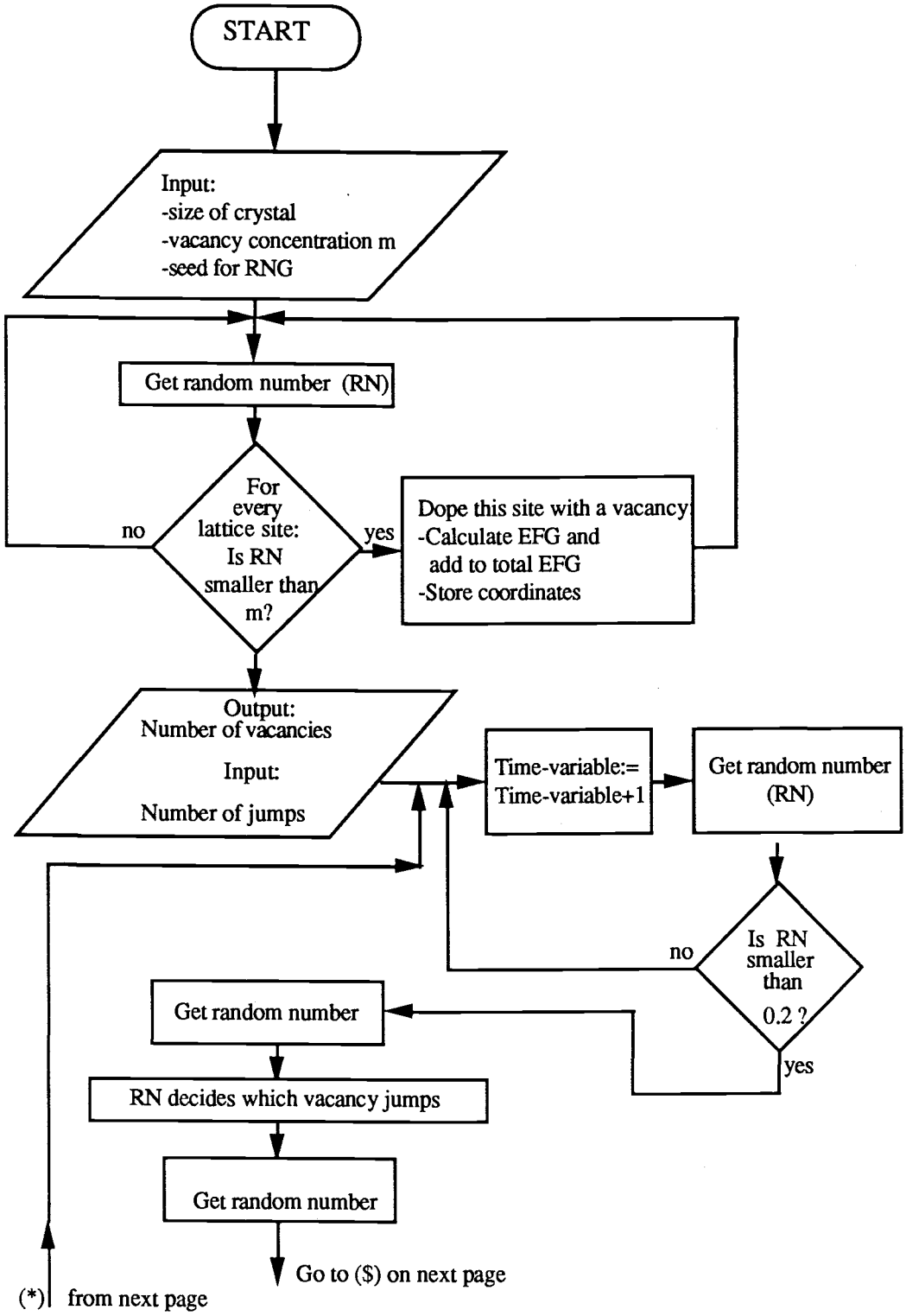

Fig. 6.1. Flow-chart of the simulation-program.

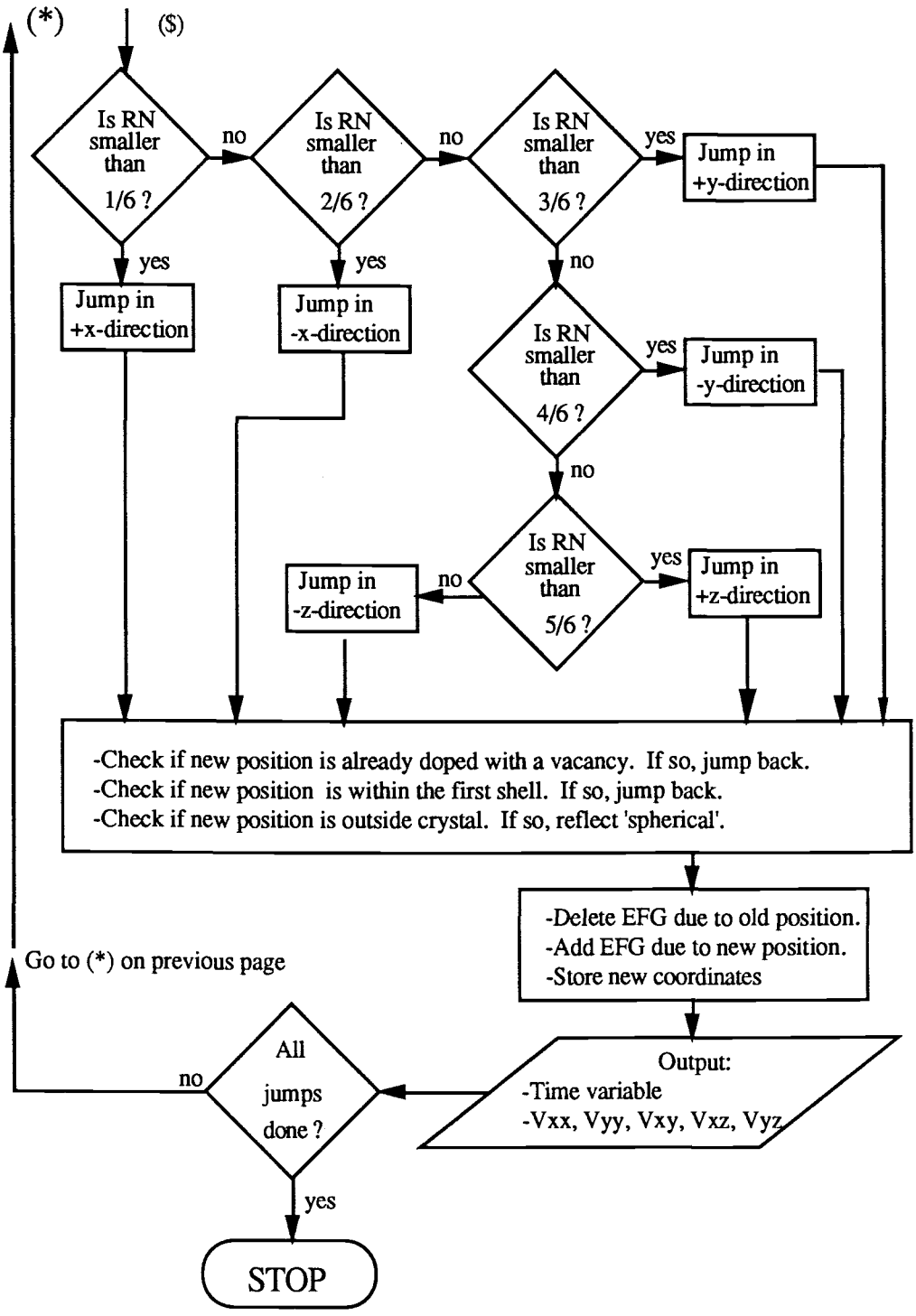

Fig. 6.1. (continued)

(i) An "elastic" boundary. This means that the vacancy, instead of hopping outside, bounced off the edge and moved towards the center of the crystal. (ii) A "periodic" boundary. This condition made use of the fact that the contributions to the EFG of a vacancy at position (x, y, z) is the same as a vacancy at position (-x, -y,- z). So, if a vacancy reached the edge of the crystal, instead of jumping outside (eg.: x', y', z'+1), it was reflected to the spherical-diagonal position (eg.: -x', -y',- z'+1).

After each jump, the new coordinates of the vacancy were stored and the time-variable together with the five components of the EFG (meaning: V_{xx}, V_{yy}, V_{xy}, V_{xz}, and V_{yz}) were saved to a disk:

$$V_{x_i,x_j} = \frac{3\,x_i\,x_j - r^2\delta_{ij}}{r^5}\,, \tag{6–1}$$

with

$$r^2 = x^2+y^2+z^2\,. \tag{6–2}$$

In Fig. 6.2 an example is given of the x-y-coordinates of all the vacancies immediately after doping the lattice as well as after 5500 jumps in a cube with 9x9x9 sites. Fig. 6.3. plots the x-coordinate of a vacancy during the simulation for both the elastic and the periodic boundary in a simulation with 5500 jumps (27500 time steps). To get a visual impression of the "randomness" of the RNG, Fig.6.4. shows which vacancy was hopping at each jump.

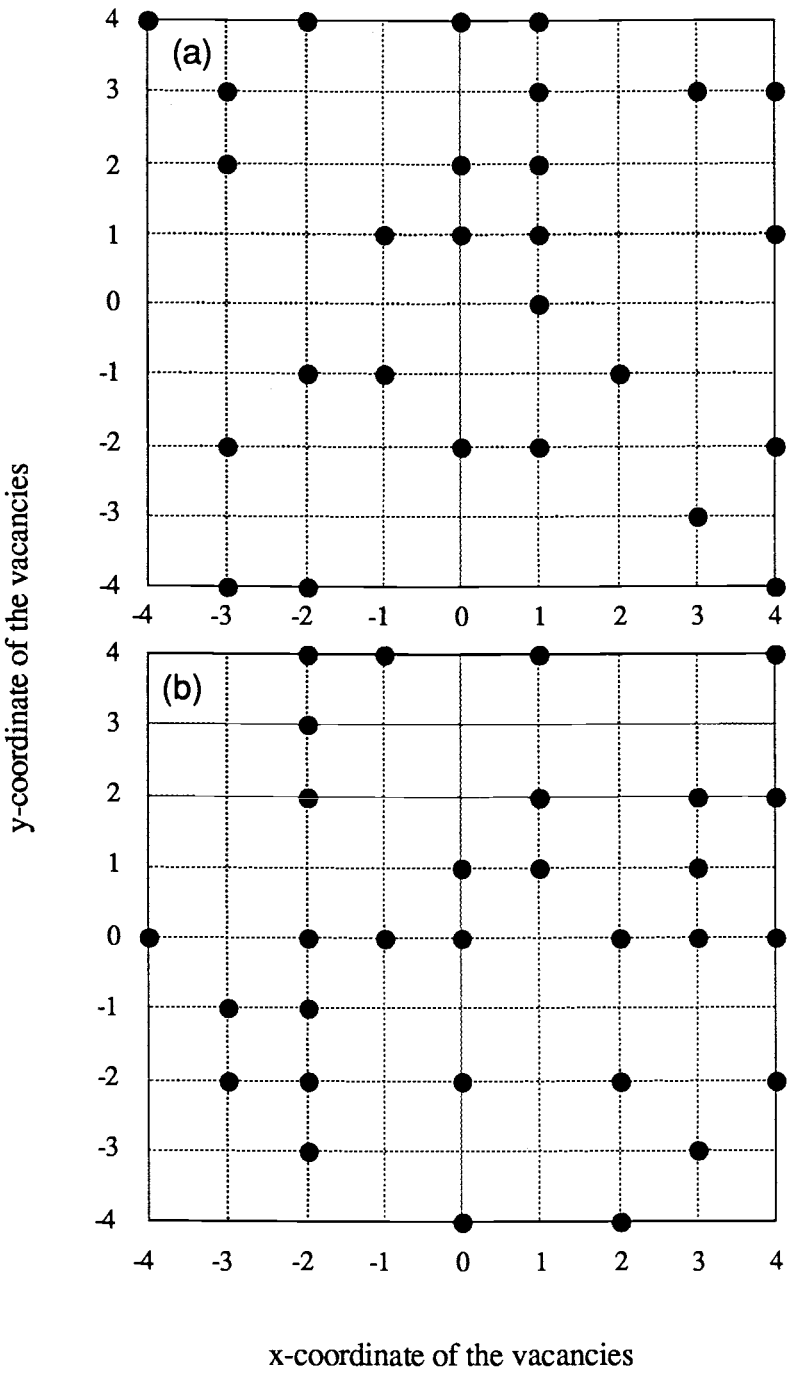

Fig. 6.2. Projection of the position of all vacancies in a 9x9x9 lattice on the x-y-plane:
(a) immediately after doping the lattice.
(b) after 5500 jumps.

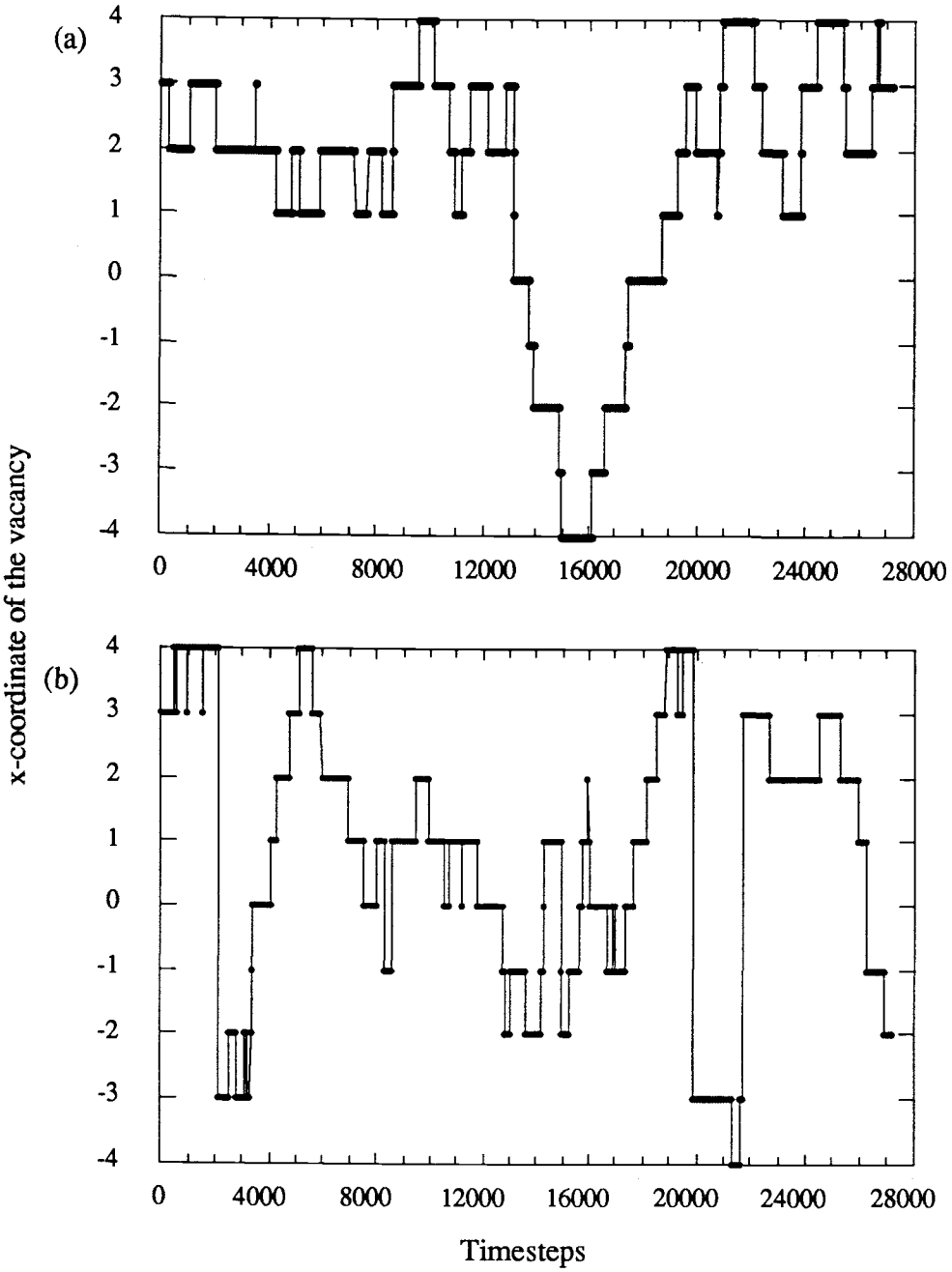

Fig. 6.3. Path of a vacancy during the simulation:
(a) bouncing boundary condition.
(b) periodic boundary condition.

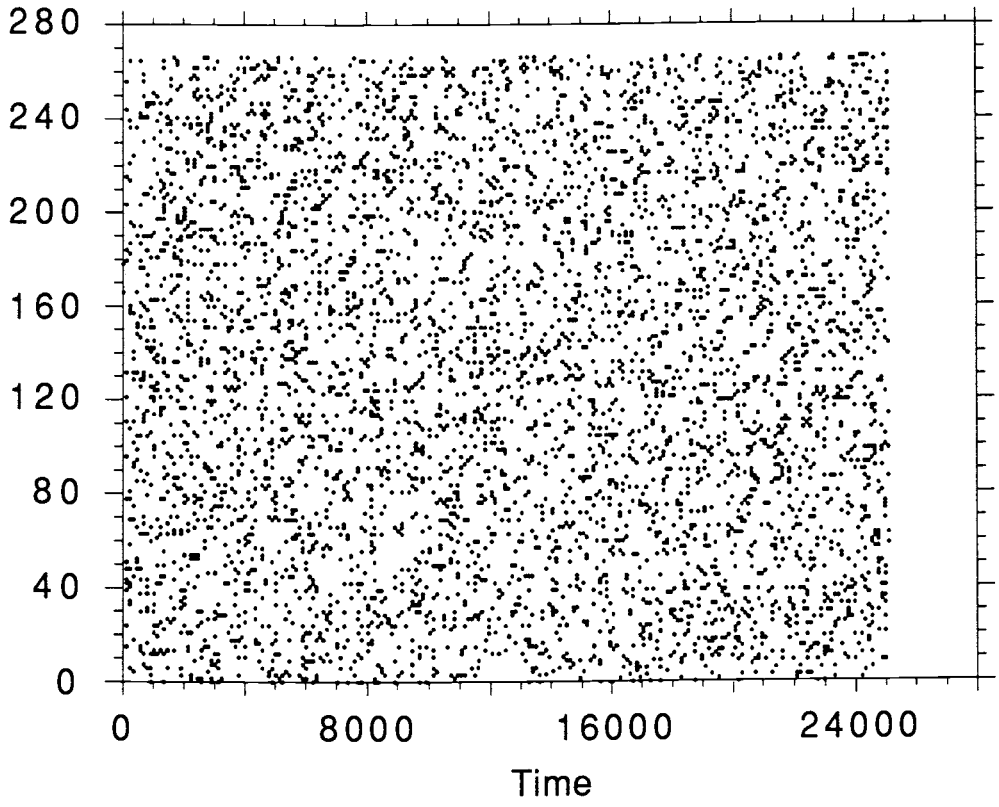

Fig. 6.4. Number of vacancy which was hopping at each jump.

6.2. Calculation of the Angular Perturbation Function, $G_2(t)$

The simulated data (6.1.), the components of the electric field gradient as a function of time, were transferred to a Ridge 32/130 computer. A laboratory-built program,[90] written in FORTRAN, calculated the angular perturbation function $G_2(t)$, which then could be compared with experimental results. The algorithm for the calculation followed very closely the description in chapter 2. With the matrix elements of the time-evolution operator

$$<m_1|\Lambda(t)|m_2>=\sum_{m_1'm_2'n}<n|m_1'>^*<n|m_2'>\exp(-\tfrac{1}{\hbar}E_n t)D^I_{m_1'm_1}{}^*(\Omega)D^I_{m_2'm_2}(\Omega)\ , \quad (2\text{–}22)$$

we obtained the angular perturbation function for polycrystalline samples:

$$G_{k\,k}(t)=\sum_{\substack{m_1m_2\\m_1'm_2'}}\sum_{n\,n'}(-1)^{2I+m_1+m_2}\begin{pmatrix}I & I & k\\ m_1' & -m_1 & N\end{pmatrix}\begin{pmatrix}I & I & k\\ m_2' & -m_2 & N\end{pmatrix}$$

$$\times\exp[-\tfrac{i}{\hbar}(E_n-E_{n'})t]<n|m_1>^*<n'|m_1'><n|m_2><n'|m_2'>^* . \quad (2\text{–}28)$$

Before the program started to actually calculate $G_2(t)$, the user had to specify the abstract time-variable of the simulation in units of $1/\omega_Q$ (see 6.3.).

The next step in the program was to calculate the Clebsch-Gordan coefficients, which are expressed as 3j-symbols in equation (2-28). The Clebsch-Gordan coefficients were time-independent, so they could be evaluated at the beginning of the program and be used throughout the whole process.

For each time-step, the EFG-components and the time-variable were read into the program. Then the Hamiltonian corresponding to these values of the EFG was diagonalized to find E_n and $E_{n'}$, and the scalar products of the form $\langle n|m_i\rangle$ were calculated. This means, physically, that the matrix elements of the density matrix were obtained for every instant at which the EFG was changing.

The total time for the simulation was divided into 512 time-intervals. So even though the matrix elements of the density matrix were calculated for every time-step in the simulation, the resulting G_2 was only obtained for 512 equidistant times. All the constants in the program were chosen in such a way that the output-time was given in units of $1/\omega_Q$.

The result of these calculations, the angular perturbation function, $G_2(t)$, caused by a simulated fluctuating electric field gradient, was saved to a disk for further analyses.

6.3. Results of Computer Simulation

As described in 6.1. and 6.2., the angular perturbation function, $G_2(t)$, was obtained by first simulating the five components of the EFG (meaning: V_{xx}, V_{yy}, V_{xy}, V_{xz}, and V_{yz}) for both static and dynamic systems and then calculating $G_2(t)$. The resulting $G_2(t)$ was compared with theoretical analytical calculations.

The constants in the calculations were chosen in such a way that the resulting time scale is given in terms of $1/\omega_Q$, if the abstract time variable was also specified in units of $1/\omega_Q$. Here ω_Q is the quadrupole frequency (2-46) corresponding to a nearest-neighbor vacancy, meaning $V_{zz} = 2$ (eqn 6-1).

6.3.1. Static EFG

The angular perturbation function, $G_2(t)$, for a static EFG is well known (see 2.4.). Comparing the results from our calculations with the expected values was a good check of the program calculating $G_2(t)$ (6.2.), and was helpful to determine the necessary constants in the program.

The five EFG components due to a vacancy at an arbitrary position in the lattice were calculated and a "static EFG" created by simply copying the same EFG components for different time-steps. This was then read into the program on the Ridge computer to calculate $G_2(t)$. As expected, the results depend only on the magnitude and not on the direction of the EFG.

An example for a vacancy located at the lattice position (0, 0, 1) can be seen in Fig. 6.5. Since the EFG due to one vacancy is axially symmetric, the results agree with the predicted angular perturbation function, $G_2(t)$, for $\eta = 0$ (see Fig. 2.2.). The EFG component V_{zz} for a vacancy at (0, 0, 1) is 2 in our units (6-1). Since the time variable is given in units of $1/\omega_Q$, the period T of $G_2(t)$ is

$$T = \frac{2\pi}{\omega_1} = \frac{2\pi}{6\omega_Q} = \frac{\pi}{3}\left(\frac{1}{\omega_Q}\right), \qquad (6\text{–}3)$$

which agrees with the result in Fig. 6.5.

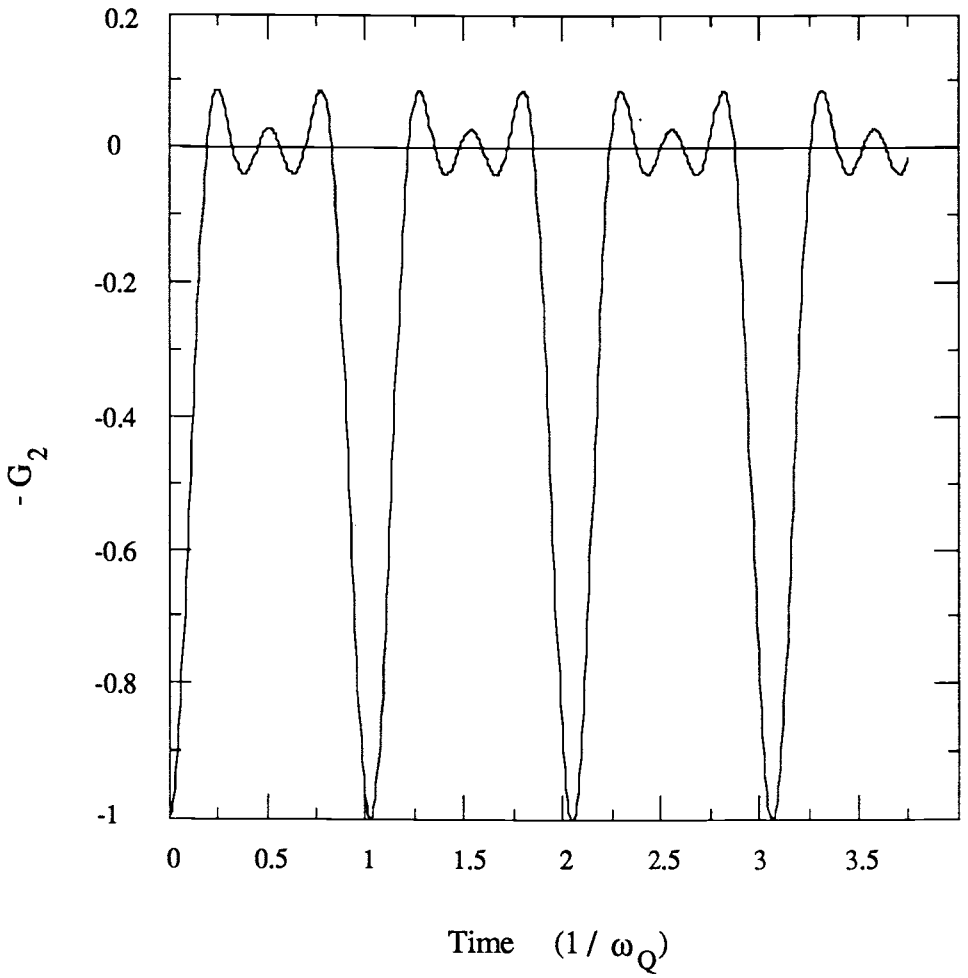

Fig. 6.5. Simulated angular perturbation function, $G_2(t)$, for a static EFG as a function of time.

6.3.2. XYZ Model

The XYZ model is a special case of the XYZ+Z model (see 2.5.2.) in which the static EFG is zero. The EFG components are therefore due to a vacancy jumping randomly between the positions $(\pm 1,0,0)$, $(0,\pm 1,0)$, and $(0,0,\pm 1)$, and the symmetry axis of the EFG fluctuates among the x, y, and z directions.

Such a system was simulated, and the resulting perturbation functions, $G_2(t)$, are shown in Fig. 6.6, 6.7, and 6.8. The time variable of the simulated EFG was an abstract integer number with time steps $\Delta t=1$ (see 6.1.). In order to compare $G_2(t)$ with theoretical calculations, this variable had to be given a physical meaning. As an average, after every five time-steps the simulated EFG was changing (meaning: a vacancy was jumping). The average correlation time, τ_c, of the system is therefore

$$\tau_c \approx 5\Delta t \ . \qquad (6\text{–}4)$$

If W is defined as the transition probability between two particular EFG states per unit time, then W can be written in terms of τ_c :[91]

$$W = \frac{1}{N\tau_c} \approx \frac{1}{N5\Delta t} \ , \qquad (6\text{–}5)$$

where N is the number of possible states of the EFG. Since for the calculation of $G_2(t)$ only the magnitude and not the direction of the EFG is relevant, there are three possible states (N = 3) for the XYZ model.

The timestep Δt was a variable to be specified in the program and Fig. 6.6 and 6.7. show the results for $\Delta t = 0.01$ (W = 6.67), whereas Fig. 6.8 is the result of

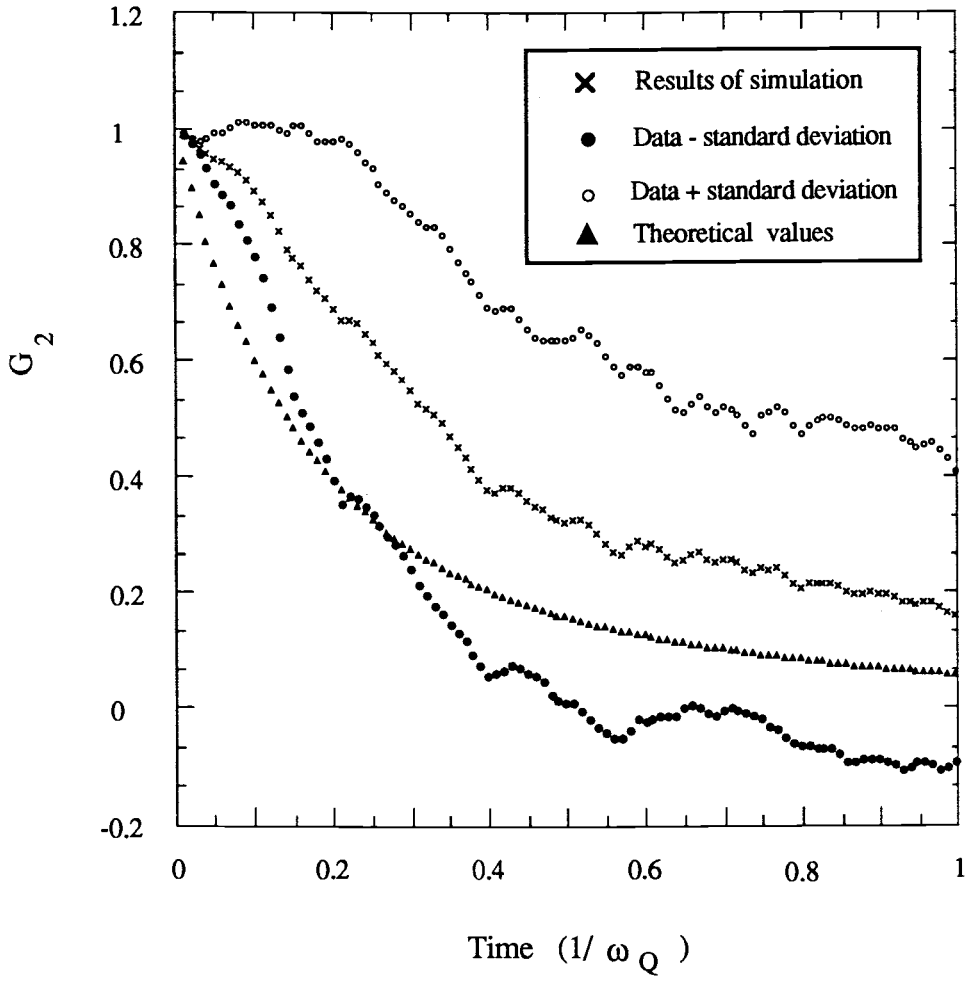

Fig. 6.6. Simulated angular perturbation function, $G_2(t)$, for the XYZ model (correlation time $\tau_c = 0.05/\omega_Q$). Data shown are the average of 10 simulations for times smaller than $1/\omega_Q$ (20 jumps). The standard deviation and the theoretical expression are discussed in the text.

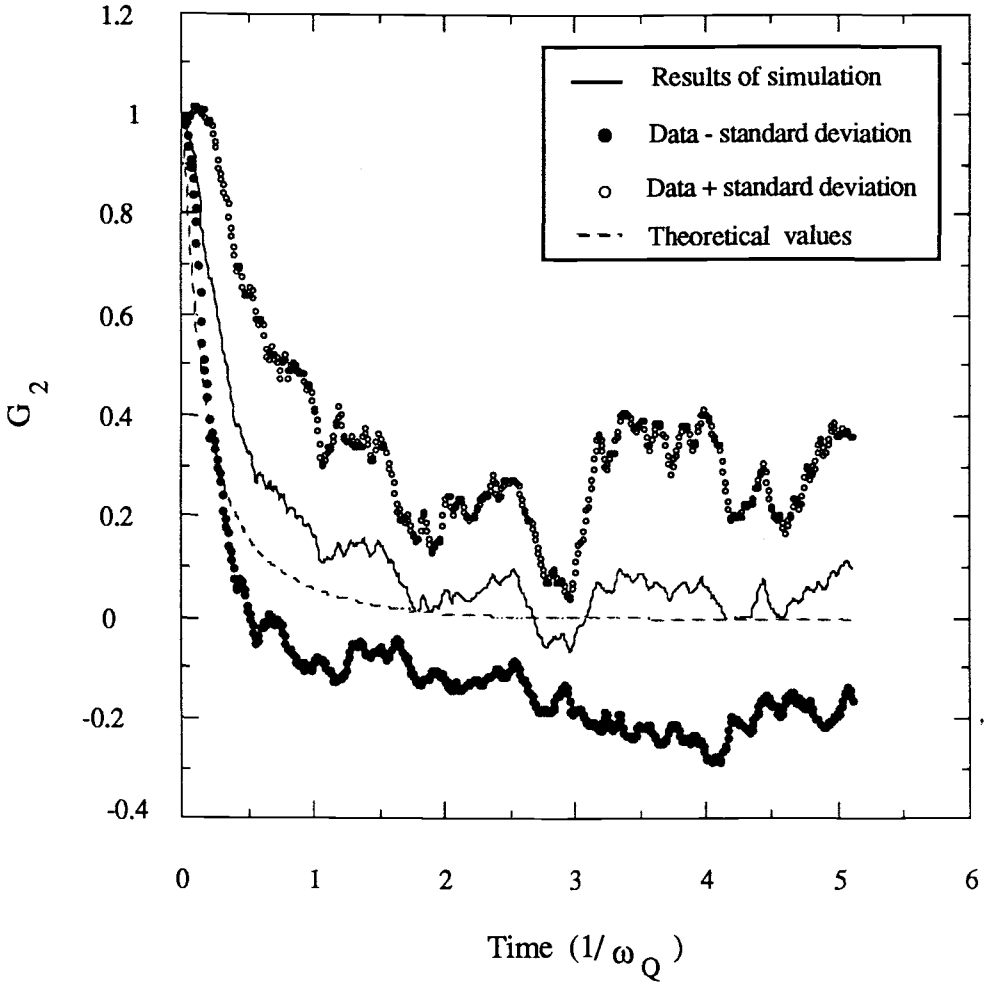

Fig. 6.7. Simulated angular perturbation function, $G_2(t)$, for the XYZ model (correlation time $\tau_c = 0.05/\omega_Q$). Data shown are the average of 10 simulations for times smaller than $5/\omega_Q$ (100 jumps). The standard deviation and the theoretical expression are discussed in the text.

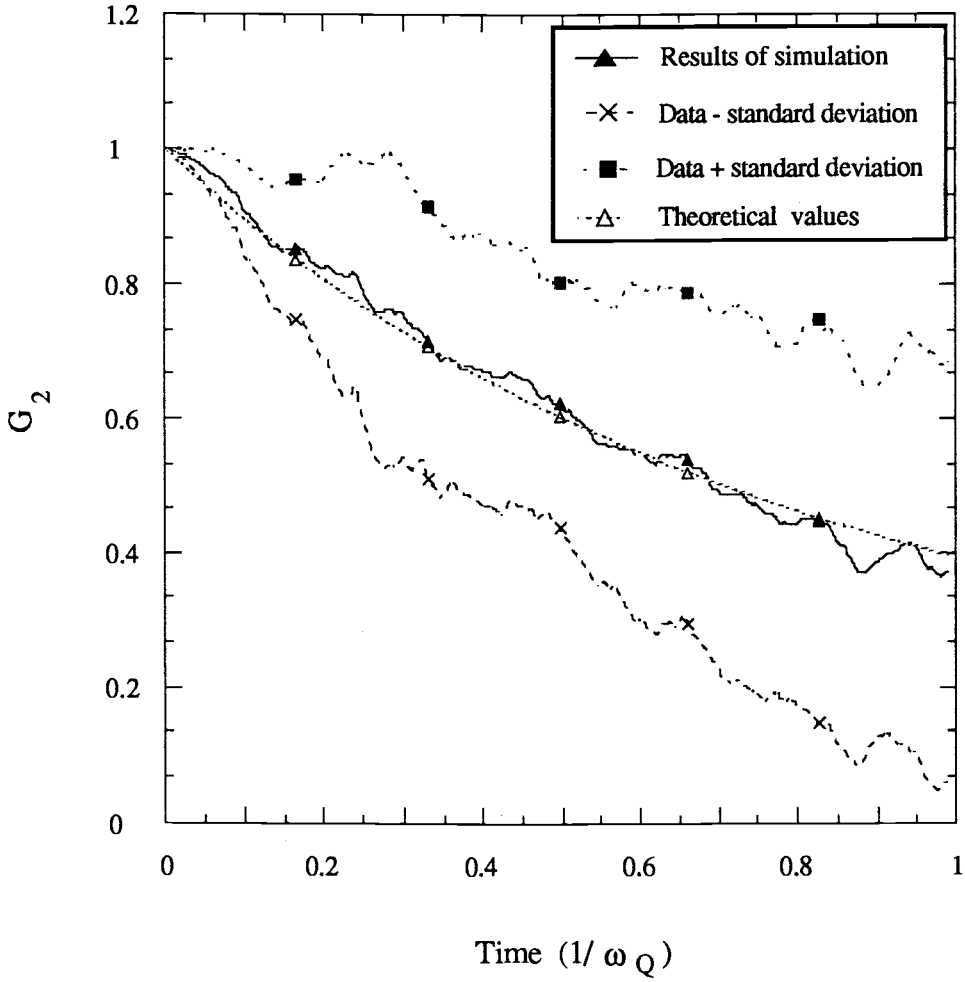

Fig. 6.8. Simulated angular perturbation function, $G_2(t)$, for the XYZ model (correlation time $\tau_c = 0.01/\omega_Q$). Data shown are the average of 10 simulations (100 jumps each). The standard deviation and the theoretical expression are discussed in the text.

choosing Δt to be 0.002 (W = 33.3).

For both values of W, $G_2(t)$ was calculated from ten statistically independent "simulation samples". Besides the average of $G_2(t)$, the standard deviation, σ, was calculated for each data point to obtain information about the statistics of the results:

$$\sigma = \sqrt{\frac{1}{n}\sum_{i=1}^{n}\left(x_i^{(k)} - \overline{x_i}\right)^2} \quad . \tag{6-6}$$

As "error bars" in Fig. 6.6., 6.7., and 6.8., the values for the average $G_2(t)$ plus and minus σ are plotted.

As discussed in chapter 2.5., there is presently no general analytical expression available for $G_2(t)$ due to time dependent EFGs in polycrystalline material. But recently, $G_2(t)$ has been described for rapidly fluctuating EFGs (W>20) as[91]

$$G_2(t) = 0.5714\exp\left\{\frac{-41.7}{W}t\right\} + 0.3032\exp\left\{\frac{-11.1}{W}t\right\} +$$

$$+ 0.0968\exp\left\{\frac{-70.1}{W}t\right\} + 0.0286\exp\left\{\frac{101}{W}t\right\} \quad . \tag{6-7}$$

This function has been calculated for the appropriate values of W and is plotted in Fig. 6.6., 6.7., and 6.8. For W = 6.67, the results of (6-7) lies within the uncertainty, except for very small times ($T<0.2/\omega_Q$) where the simulated data are larger than the calculated values. It is not surprising that (6-7) does not fully describe the data since it is actually only valid for more rapidly fluctuating EFGs (W>20).

In the case of W = 33.3, where expression (6-7) is really applicable, the data are excellently described by the theoretical values. In fact, when W is kept variable in a

least squares fit of eqn (6-7) to the data, W turns out to be 33.15.

The obtained data show that for rapidly fluctuating EFGs already a small number of simulations is sufficient for a qualitative analysis. Nevertheless, further research has to be done to achieve better statistics and a bigger variety of correlation times, τ_c.

So far, our results obtained from simulated EFG fluctuations support the theory that the perturbation function, $G_2(t)$, caused by fast fluctuating EFGs can be described by (6-7).

6.3.3. General Time-Dependent EFG

To simulate a system which is closer to "real life" than the XYZ model, a simple cubic crystalline lattice of 9x9x9 sites was set up and doped with vacancies (concentration of vacancies was chosen to be 5%). These vacancies then were allowed to move, creating a fluctuating EFG (see 6.1.). The angular perturbation function, $G_2(t)$, calculated from these data for correlation times,τ_c, of $0.1/\omega_Q$ and $0.001/\omega_Q$ are given in Fig. 6.9. and 6.10., respectively.

Oxygen vacancies were not allowed to occupy next neighbor positions since PAC measurements indicated that during the lifetime of the intermediate state no vacancies would be found on nearest neighbor positions.

As already mentioned, there is presently no theory available which these data could be compared with. Nevertheless, some features of the results may be noted.

More than for the XYZ model, a non-exponential hyperbolic term in $G_2(t)$ is visible for small times. Even in the case of $\tau_c = 0.001/\omega_Q$, meaning the lifetime of the intermediate state of the PAC probe is considerably longer than a single jump time of a vacancy, the hyperbolic part is dominant up to $0.25/\omega_Q$, where $G_2(t)$ has a value of 0.7.

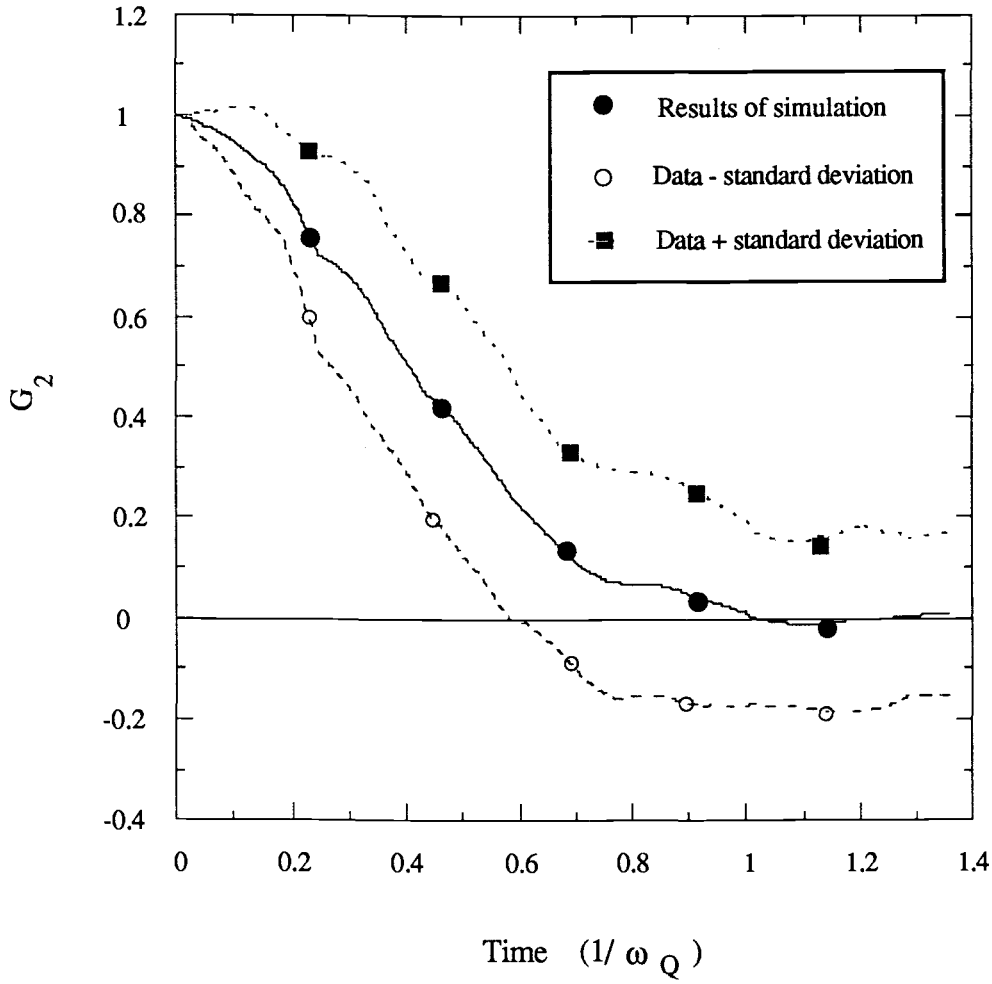

Fig. 6.9. Simulated angular perturbation function, $G_2(t)$, for a simple cubic crystal (9x9x9 sites). The correlation time, τ_c, is $\tau_c = 0.001/\omega_Q$. Data shown are the average of 9 simulations (1375 jumps each). The standard deviation is discussed in the text.

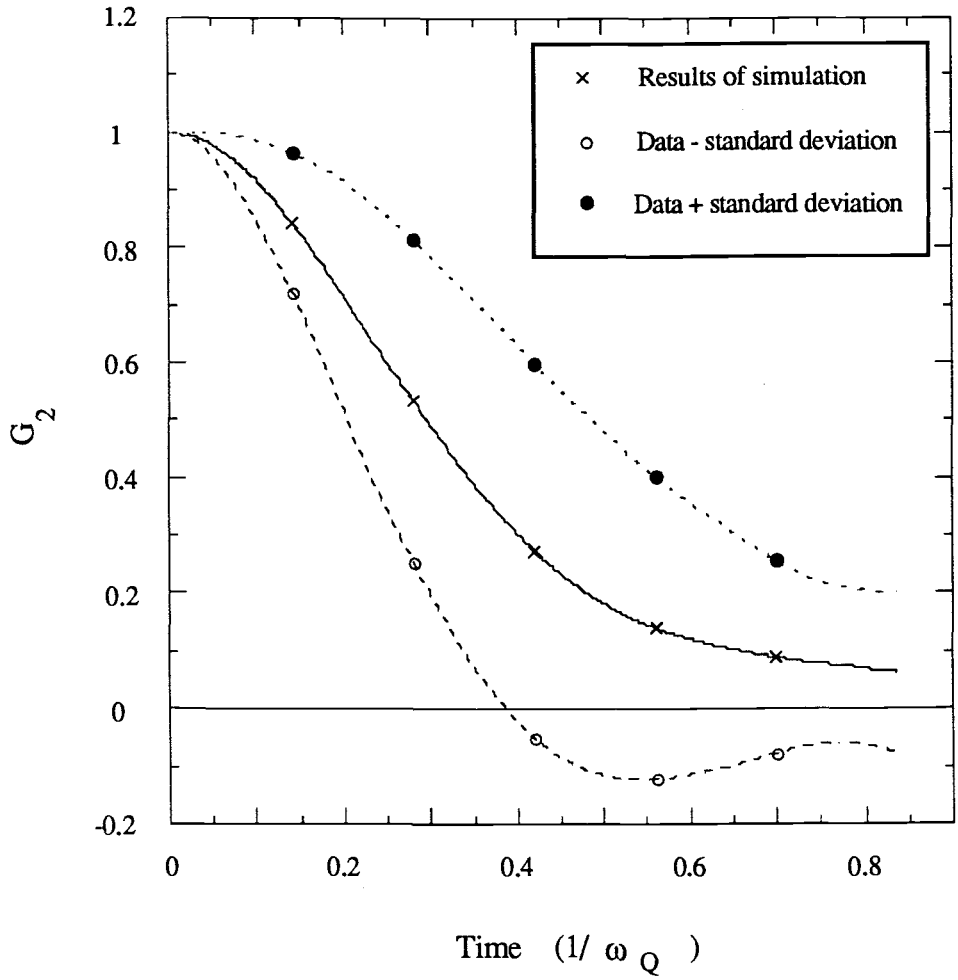

Fig. 6.10. Simulated angular perturbation function, $G_2(t)$, for a simple cubic crystal (9x9x9 sites). The correlation time, τ_c, is $\tau_c = 0.1/\omega_Q$. Data shown are the average of 10 simulations (8 jumps each). The standard deviation is discussed in the text.

A possible explanation is small values of W due to many possible directions, meaning N is considerably larger than for the XYZ model. This is especially reasonable because the first shell was excluded for vacancy positions. The second shell already has 12 positions, and the contributions due to vacancies in the third shell (which has even more positions) are not negligible. Future simulations using different lattice structures may yield useful information to solve this problem.

Even though pure exponential fits are not very meaningful (because of the shape of the curves discussed above), it is clear that the decay rate increases with increasing τ_c. This is qualitatively the same behavior which was observed for the XYZ model.

The purpose of presenting the data for the general time dependent EFG (6.3.3.) is not to give a full analysis, but rather to give a flavor for how the developed simulation method can be used for future research. It provides a powerful tool which complements laboratory experiments.

References

1. J. G. Bednorz and K. A. Müller, Z. Phys. B **64**, 189 (1986).

2. *Science and Technology of Zirconia*, Advances in Ceramics, Vol. 3, edited by A. H. Heuer and L. W. Hobbs, The American Ceramic Society, Columbus, OH (1981).

3. *Science and Technology of Zirconia II*, Advances in Ceramics, Vol. 12, edited by N. Claussen, M. Rühle, and A. H. Heuer, The American Ceramic Society, Columbus, OH (1984).

4. *Science and Technology of Zirconia III*, Advances in Ceramics, Vol. 24 A&B, edited by S. Somiya, N. Yamamoto, and H. Hanagida, The American Ceramic Society, Westerville, OH (1988).

5. R. Stevens, *An Introduction to Zirconia*, 2/e, Magnesium Elektron Ltd., Flemington, NJ (1986).

6. A. H. Heuer and L. K. Lenz, J. Am. Ceram. Soc. **69**, 325 (1982).

7. *International Table for Crystallography*, Vol. A, edited by T. Hahn, D. Reidel Publishing Co., Dordrecht (1987).

8. R. W. G. Wyckoff, *Crystal Structures*, Vol. 2, John Wiley & Sons, New York (1960)

9. D. K. Smith and H. W. Newkirk, Acta Cryst. **18**, 983 (1965).

10. R. N. Patil and E. C. Subbarao, J. Appl. Cryst. **2**, 281 (1969).

11. G. Teufer, Acta Cryst. **15**, 1187 (1962).

12. P. Aldebert and J.–P. Traverse, J. Am. Ceram. Soc. **68**, 34 (1985).

13. R. C. Garvie, R. H. Hannink, and R. T. Pascoe, Nature **258**, 703 (1975).

14. G. M. Wolten, J. Am. Ceram. Soc. **60**, 543 (1962).

15. E. C. Subbarao, in ref. 1, p. 1.

16. J. Faber, Jr, M. H Mueller, and B. R. Cooper, Phys. Rev. B **17**, 4884 (1978).

17. T. S. Sheu, J. Xu, and T. Y. Tien, "The systems ZrO_2–Sc_2O_3 and ZrO_2–In_2O_3", presented at the 90th Annual Meeting of The American Ceramic Society, Cincinnati, OH, May 1–5, 1988.

18. H.T. Su, Ph. D. Thesis, Oregon State University (1989), unpublished, p. 6.

19. V. S. Stubican, in ref. 3, p. 71.

20. H. G. Scott, J. Mater. Sci. **10**, 1527 (1975).

21. V. I. Alexandrov, V. V. Osiko, A.M.Prokhorov, and V. M. Tatarintsev, in *Current Topics in Materials science, Vol. 1*, edited by E. Kaldis, North Holland Publishing Co., Amsterdam (1978), pp 497 - 517.

22. J. D. Jackson, *Classical Electrodynamics*, 2/e, John Wiley & Sons, New York (1975) Chap. 16.

23. *Perturbed Angular Correlations*, edited by E. Karlsson, E. Matthias, and K. Siegbahn, North–Holland, Amsterdam (1964).

24. E. Recknagel, G. Schatz, and Th. Wichert, in *Hyperfine Interactions of Radioactive Nuclei*, edited by J. Christiansen, Springer–Verlag, Berlin (1983), pp. 133–204.

25. G. S. Collins and R. B. Schuhmann, Phys. Rev. B **34**, 502 (1986).

26. H. Metzner, R. Sielemann, S. Klaumünzer, and E. Hunger, Phys. Rev. B **36**, 9535 (1987).

27. F. Raether, D. Wiarda, K. P. Lieb, J. Chevallier, and G. Weyer, Z. Phys. B **73**, 467 (1989).

28. W. Bolse, M. Uhrmacher, and K. P. Lieb, Phys. Rev. B **36**, 1818 (1987).

29. W. Segeth, D. O. Boerma, L. Niesen, and P. J. M. Smulders, Phys. Rev. B **39**, 10725, (1989).

30. A. F. Pasquevich and R. Vianden, Phys. Rev. B **35**, 1560 (1987).

31. A. F. Pasquevich and R. Vianden, Phys. Rev. B **37**, 10858 (1988).

32. K. Krusch and J. A. Gardner, Phys. Rev. B **24**, 4587 (1981).

33. M. Brüssler, H. Metzner, K.–D. Husemann, and H. J. Lewerenz, Phys. Rev. B **38**, 9268 (1988).

34. A. Lerf and T. Butz, Hyperfine Interactions **36**, 275 (1987).

35. R. Vianden, Hyperfine Interactions **15/16**, 1081 (1983).

36. H. Jaeger, J. A. Gardner, J. C. Haygarth, and R. L. Resera, J. Am. Ceram. Soc. **69**, 458 (1986).

37. A. Baudry, P. Boyer, and A. L. de Oliveira, J. Phys. Chem. Solids **43**, 871 (1982).

38. H. T. Su, Ph. D. Thesis, Oregon State University (1989), unpublished.

39. H. Jaeger, Ph. D. Thesis, Oregon State University (1987), unpublished.

40. J. A. Gardner, H. Jaeger, H. T. Su, W. H. Warnes, and J. C. Haygarth, Physica B **150**, 223 (1988).

41. H. Haas and D. A. Shirly, J. Chem. Phys. **58**, 3339 (1973).

42. Y. A. Ellis, Nucl. Data Sheets **9**, 319 (1972).

43. *Table of Isotopes*, 7/e, edited by C. M. Lederer and V. S. Shirley, Wiley–Interscience, New York (1978), p. 521.

44. H. Frauenfelder and R. M. Steffen, in *Alpha– Beta– and Gamma–Ray Spectroscopy*, Vol. 2, edited by K. Siegbahn, North–Holland, Amsterdam (1965), Chap. XIXA, pp997–1198.

45. R. M. Steffen and K. Adler, in *The Electromagnetic Interaction in Nuclear Spectroscopy*, edited by W. D. Hamilton, North–Holland, Amsterdam (1975), Chap. 13, pp 583–643.

46. A. Abragam and R. V. Pound, Phys. Rev. **92**, 943 (1953).

47. W. E. Evenson, A. G. McKale, H. T. Su, and J. A. Gardner, Hyperfine Interactions, to be published.

48. A. Messiah, *Quantum Mechanics*, Vol. II, John Wiley & Sons, New York (1968).

49. E. Matthias, W. Schneider, and R. M. Steffen, Phys. Rev. **125**, 261 (1962).

51. L. A. Mendoza–Zélis, A. G. Bibiloni, M. C. Caracoche, A. R. López–García, J. M. Martínez, R. C. Mercader and A. F. Pasquevich, Hyperfine Interactions **3**, 315 (1977).

52. W. H. Warnes and J. A. Gardner, Phys. Rev. B **40**, 4276 (1989).

53. P. da R. Andrade and J. D. Rogers, Phys. Rev. B **3**, 1052 (1971).

54. A. Baudry and P. Boyer, Hyperfine Interactions **35**, 803 (1987).

56. H. Winkler and E. Gerdau, Z. Physik **262**, 363 (1973).

57. H. Jaeger, J. A. Gardner, H. T. Su and R. L. Rasera, Rev. Sci. Instrum. **58**, 1694 (1987).

58. A. Baudry, P. Boyer, and P. Vulliet, Hyperfine Interactions **13**, 263 (1983).

59. C. Hohennemser and R. B. Schuhmann, Hyperfine Interactions **30**, 109 (1986).

60. *Harshaw radiation detectors*, Harshaw/Filtrol Partnership, Solon (1984).

61. M. Laval, M. Moszynski, R. Allenand, E. Cormoreche, P. Guinet, R. Odru and J. Vacher, Nucl. Instr. Meth. **206**, 169 (1983).

62. A. R. Arends, C. Hohennemser, F. Pleiter, H. De Waard, L. Chow, and R. M. Sutter, Hyperfine Interactions **8**, 191 (1980).

63. P. R. Bevington, *Data Reduction and Error Analysis for the Physical Sciences*, McGraw–Hill, New York, (1969).

64. E. N. Kaufman and R. J. Vianden, Rev. Mod. Phys. **51**, 161 (1979).

65. H. Jaeger, Ph. D. Thesis, Oregon State University (1987), unpublished, p. 100.

66. F. D. Feiock and W. R. Johnson, Phys. Rev. **187**, 39 (1969).

67. A. G. Marshall and C. F. Meares, J. Chem.Phys. **56**, 1229 (1972).

68. G. S. Collins (1981), unpublished.

69. P. C. Lopiparo and R. L. Rasera, in *Angular Correlations in Nuclear Disintegration*, edited by H. V. Krugten and B. Van Nooijen, Rotterdam University Press, Rotterdam (1971).

70. S. Ikeda, O. Sakurai, K. Uematsu, N. Mizutani, and M. Kato, J. Mater. Sci. **20**, 4593 (1985).

71. M. Kuwabara, T. Murakami, M. Ashizu, Y. Kubota, and T.Tsukidate, J. Mater. Sci. Lett. **4**, 467 (1985).

72. M. Weller, H. Schubert, J. Am. Ceram. Soc. **69**, 573 (1986).

73. P. Papet, P. Abélard, and J. F. Baumard, in ref.4, p.p. 781.

74. N. Bonanos, R. K. Slotwinski, B. C. H. Steele, and E. P. Butler, J. Mater. Sci. Lett. **3**, 245 (1984).

75. K. Keizer, M. Van Hemert, M. A. C. G. Van de Graaf, Solid State Ionics **16**, 67 (1985).

76. M. J. Vervek, B. J. Middlehuis, and A. J. Burggraaf, Solid State Ionics, **6**, 159 (1982).

77. M. J. Vervek, A. J. A. Winnubst, and A. J. Burggraaf, J. Mater. Sci. **17**, 3113 (1982).

78. S. P. S. Badwal, J. Mater. Sci. **19**, 1767 (1984).

79. S. P. S. Badwal and M. V. Swain, J. Mater. Sci. Lett. **4**, 487 (1985).

80. E. Schouler, M. Kleitz, and C. Desportes, J. Chim. Phys. (Paris), **70**, 923, (1973).

81. P. Abélard and J. F. Baumard, Phys. Rev.B. **187**, 1005 (1982).

82. J. F. Baumard P. Papet, and P. Abélard, in ref.4, p. 779.

83. A.S. Nowick, in *Diffusion in Crystalline Solids*, edited by G. E. Murch and A.S. Nowick, Academic Press, New York (1984), pp 143-188.

84. J. F. Baumard,and P. Abélard, in ref.3, p.555.

85. V. Butler, C. R. A. Catlow, and B. E. F. Fender, Solid State Ionics **5**, 539 (1981).

86. H. J. Rossell, in ref. 2, p. 47-63.

87. A. J. A. Winnubst, P. J. M. Kroot, and A. J. Burggraaf, J. Phys. Chem. Solids **44**, 955 (1983).

88. D. Knuth, in *Numerical Recipes,* edited by W. H. Press, B. P. Flannery, S. A. Teukolsky, and W. T. Vetterling, Cambridge University Press, New York (1986), pp 198-199.

89. J. Roberts, private comunication.

90. H. J. F. Jansen, unpublished.

91. W. E. Evenson, to be published.